



HAL
open science

Thermal boundary layer modelling for heat flux prediction of bubbles at saturation: A priori analysis based on fully-resolved simulations

Mathis Grosso, Guillaume Bois, Adrien Toutant

► To cite this version:

Mathis Grosso, Guillaume Bois, Adrien Toutant. Thermal boundary layer modelling for heat flux prediction of bubbles at saturation: A priori analysis based on fully-resolved simulations. *International Journal of Heat and Mass Transfer*, 2024, 222, pp.124980. 10.1016/j.ijheatmasstransfer.2023.124980 . cea-04419812

HAL Id: cea-04419812

<https://cea.hal.science/cea-04419812>




Submitted on 26 Jan 2024

HAL is a multi-disciplinary open access archive for the deposit and dissemination of scientific research documents, whether they are published or not. The documents may come from teaching and research institutions in France or abroad, or from public or private research centers.

L'archive ouverte pluridisciplinaire **HAL**, est destinée au dépôt et à la diffusion de documents scientifiques de niveau recherche, publiés ou non, émanant des établissements d'enseignement et de recherche français ou étrangers, des laboratoires publics ou privés.




Highlights

Thermal boundary layer modelling for heat flux prediction of bubbles at saturation: *a priori* analysis based on fully-resolved simulations

Mathis Grosso , Guillaume Bois , Adrien Toutant 

- The numerical method of `TrioCFD`, a Front-Tracking code developed at CEA, is exposed for direct resolution of heat transfer problems in bubbly flows at saturation.
- The gradient correction approaches, developed for chemical species transport phenomena, are re-employed and investigated for temperature gradient correction in the bubbles' interface vicinity.
- *A priori* assessment of a radial sub-resolution method on steady-state fully resolved simulations results produced promising results at moderate Reynolds and Prandtl numbers.
- A local post-processing shows that the tangential convective term contribution is significant and could be modelled to further enhance the local sub-layer temperature prediction.

Thermal boundary layer modelling for heat flux prediction of bubbles at saturation: a *priori* analysis based on fully-resolved simulations

Mathis Grosso ^a, Guillaume Bois ^a, Adrien Toutant ^b

^aUniversité Paris-Saclay, CEA, Service de Thermo-hydraulique et de Mécanique des Fluides, Gif-sur-Yvette, 91191, France

^bPROMES - CNRS (UPR 8521), Université de Perpignan Via Domitia, Perpignan, 66100, France

Abstract

This study presents and investigates uni-directional thermal sub-layer enhancement techniques within the context of an interface tracking method for simulating bubbly flows at saturation. Current discretisation methods on structured and fixed Cartesian grids tend to spread the bubbles' interface region, creating a trade-off between the freely moving nature of the bubble to the detriment of accurately capturing the discontinuous aspect of the interface and variations of properties and fluxes crossing it. Although robust techniques have been described in the literature to ensure energy conservation, less research has been undertaken to develop a methodology to retrieve the non-linear behaviour of quantities in the interface vicinity at a reasonable computational cost. In this study, the discretised bubble surface is used as a basis for addressing several quasi-static radial sub-problems that are bounded by an interfacial constant saturation temperature and a CFD temperature field value. A first approach, based on an analytical solution fitted at each time step using underlying Eulerian field values, has been developed to incorporate near-interface physics. This includes the tangential effect, incoming fluid velocity, and local mean curvature (first order surface approximation). A semi-analytical approach needs to meet certain assumptions to be valid. This is due to its derivation from a simplified plane boundary-layer development or from a spherical diffusion problem which limits its applicability range. Therefore, a second approach based on a uni-directional sub-resolution fed carefully by interpolated velocity and tangential source terms demonstrates promising results as it aligns with the principal variations of the solution. Both methodologies have been applied onto DNS data of a steady rising bubble configuration at low and moderate Reynolds {3.6; 62.5} and Prandtl {1; 2.5; 5} numbers with a constant interfacial temperature after an extensive analysis of the advection-diffusion terms hierarchy. The key aspects to maximise the effectiveness of the sub-resolution method have been clearly identified and discussed. The Sub-resolution shows better applicability to our case study on moderately large thermal layers. The newly predicted interfacial temperature gradient and temperature profile could be re-employed for Eulerian fluxes correction.

Keywords: Two-phase flows, Heat transfer, Front-Tracking, Ghost Fluid Method, Boundary-Layer modelling, Sub-grid modelling

Nomenclature

a_Γ	Interfacial area	$\cdot^{(c)}$	Continuous variable
Ar	Archimedes number	$\cdot^{(d)}$	Discretised variable
CFL	Courant number $U\Delta t\Delta x$	\cdot_k	Parameter related to phase k
Fo	Fourier number $\alpha\Delta t/\Delta x^2$	\mathbf{e}^i	Dual basis vector
Ja	Jakob number	\mathbf{e}_i	Natural basis vector
Mo	Morton number	$\tilde{\mathbf{e}}_i$	Normalised basis vector
Nu	Nusselt number	$\cdot _l$	Variable \cdot evaluated at location l
Oh	Ohnesorge number	$\llbracket \cdot \rrbracket$	Jump of property
Pe	Peclet number	$\langle \cdot \rangle$	Average value
Pr	Prandtl number	D_b	Bubble diameter
Re	Reynolds number	R_b	Bubble radius
We	Weber number	g	Gravity norm
α	Thermal diffusivity	I_k	Discrete indicator function: phase k
χ_k	Phase indicator function: phase k	\mathcal{L}^{vap}	Latent heat of vaporisation
Δt	Time step	\dot{m}	Mass flow rate per unit area
δ_Γ	Dirac function at the bubble interface	\mathbf{n}_k	Normal unit vector pointing outward phase k
Δ_d	Length of a cell's diagonal	p	Pressure
Δ_{d^*}	One length and a half of a cell's diagonal	T_δ^θ	Probe's tip temperature for non-dimensionalisation
$\Delta_{x,y,z}$	Spatial resolutions	T_∞^θ	Local temperature for non-dimensionalisation
$\Gamma, \cdot^\Gamma, \cdot_\Gamma$	Interface related parameter	T_∞	Global temperature for non-dimensionalisation
κ	Mean curvature	T	Temperature
λ	Thermal conductivity	t	Time
μ	Dynamic viscosity	\mathbf{u}	Velocity vector field
ν	Kinematic viscosity	u	Velocity component in the x-direction
ϕ	Azimuthal coordinates: $\phi \in [0, 360]^\circ$	v	Velocity component in the y-direction
ρ	Density	w	Velocity component in the z-direction
σ	Surface tension	u_r	Velocity component in the radial direction
Θ	Dimensionless temperature	u_θ	Velocity component in the tangential direction
θ	Elevation coordinates: $\theta \in [0, 180]^\circ$	u_ϕ	Velocity component in the azimuthal direction

1 Introduction

Direct Numerical Simulations (DNS) of two-phase flows have been widely developed and enhanced since the last decade to simulate growing complexity problems. It starts from boiling [1, 2], evaporation of droplets [3–6], free surface flow [7] to simulations involving species reactions [8].

One of the key issues when simulating two-phase flows with sharp interfaces is to capture properly the discontinuity of properties (density and viscosity jumps $[\![\rho]\!]_{\Gamma}$ and $[\![\mu]\!]_{\Gamma}$). Capturing these strong interfacial property variations is partially related to momentum and energy conservation but it also determines how accurately the strong variations of physical quantities like temperature will be captured near the interface.

The Front-Tracking method [9, 10], used extensively in this article, provides an accurate representation of the interface topology. The interface is represented by discrete Lagrangian markers from which the surface tension force $\propto \sigma \kappa$ can be computed accurately. However, this approach needs particular attention to remain conservative (compared to Volume Of Fluid approaches [2, 11, 12]) as the marker's advection at each time step could lead to an accumulation of the marker's position error [13].

Research groups have been focusing on conservative aspects of numerical methods in interfacial cells. However, it does not ensure that the variation of quantities is well captured near the interface. One of the key aspects of the numerical simulations is the interfacial conditions which can have a large influence on the results. In two-phase flow simulations, jump or transmission conditions are essential. At the interfaces, they are often implicitly taken into account by considering averaged properties, which are obtained through arithmetic or harmonic averaging of the two fluids' properties. It causes a lower convergence rate compared to boundary-fitted methods (such as Arbitrary Lagrangian-Eulerian methods [14–16]).

Moreover, if global conservation is aimed, diffusion operators are still defined in a Finite-Difference (FD) manner on a stencil straddling the interface. Patankar [17], Tryggvason *et al.* [18] or Toutant [10] have already underlined the necessity of using a direction-dependant viscosity across the interface (both arithmetic and harmonic mean viscosity weighted by the void fraction). At viscosity ratios μ_v/μ_l close to unity, either viscosity calculation will be valid and lead to decent results. The same issue arises in the heat flux prediction and the calculation of the thermal conductivity λ .

One can notice that the viscosity ratio of water liquid-vapour at saturation is relatively close to unity so the convergence of the velocity field can be obtained without much effort for various types of realistic flows using the so-called one-fluid approach. However, when solving for the energy *i.e.* the temperature, it becomes much more difficult to perform an accurate simulation at a low cost. Considering phase change, it can be noticed that the temperature at the interface will remain constant as the process takes place at saturation temperature (considered constant in this work). As a consequence, it is necessary to impose a constant Dirichlet boundary condition (one for each phase) at the exact position of the interface. As pre-

viously introduced methods are spreading the interface over a cell, it remains extremely difficult to impose such interfacial conditions accurately (**Sec. 2.1.3** will discuss the numerical approaches deeper). A so-called Ghost Fluid Method (GFM) is then used [19].

Various papers have implemented such methods. However, their simulations are performed on test cases or on single bubbles to answer problematic often linked to isolated nucleation:

- Stefan flow - 1D [2].
- Static bubble expansion (Scriven) - 2D axisymmetric and 3D [1, 2].
- Single rising bubble evaporating in an initially quiescent fluid [20].
- Single nucleating bubble - 2D axisymmetric [21].

These cases are very demanding and highly refined meshes are then required. 2D simulations of such complex phenomena have shown very promising results but going one dimension higher will not likely be accessible without any sub-grid scale modelling strategy.

In addition to this particular treatment of the temperature field, it is necessary to understand that in the presence of phase change, the dynamics and the temperature evolutions are coupled. An inaccurate prediction of the temperature variations close to the interface will inevitably lead to an inaccurate prediction of the interface velocity due to phase change ($\delta \mathbf{u}_{\Gamma} \propto [\![\lambda \nabla T \cdot \mathbf{n}_{\Gamma}]\!]_{\Gamma}$). Integral measures of error such as the bubble growth rate are then converging at a very low rate and extremely refined meshes are needed.

Various strategies have emerged in the literature to better capture the strong temperature variations in a given interface vicinity and at high Prandtl numbers (*i.e.* when the thermal diffusivity is lower than the momentum diffusivity). Strong temperature variations are not only observed in bubbly flows. They are present in single-phase flows near heated walls. In fact, some research groups [28] have been using a finer secondary mesh to resolve the temperature in single-phase flows. If the velocity is sufficiently converged (*i.e.* for a Prandtl number $Pr > 1$ in the presence of a non-slip wall), it can be interpolated onto the finer mesh to transport the temperature. Both the temperature strong variations appearing near walls and temperature fluctuations due to turbulence can thus be captured at a moderate cost.

Some noticeable approaches applied to the dynamic of particles (Particle-Resolved DNS) such as in the work of Vreman [22] are also interesting. In his work, Vreman uses a highly refined particle-attached mesh lying on a less refined Eulerian grid (see **Fig. 1.a**). A spherical coordinate system has been used to take advantage of the rigid particle aspect. He is finally able to capture accurately the velocity boundary layer which is demanding regarding the no-slip boundary condition. This method could be straightforwardly applied to predict the temperature evolution for a fixed particle at a constant temperature. For a weakly deformable bubble, the equation should be reformulated in curvilinear coordinates attached to the interface. Derivation of such equations may be cumbersome and implies the use of scale factors (metrics). Their application remains limited to small deformations.

Adaptive Mesh Refinement (AMR) techniques tend to be

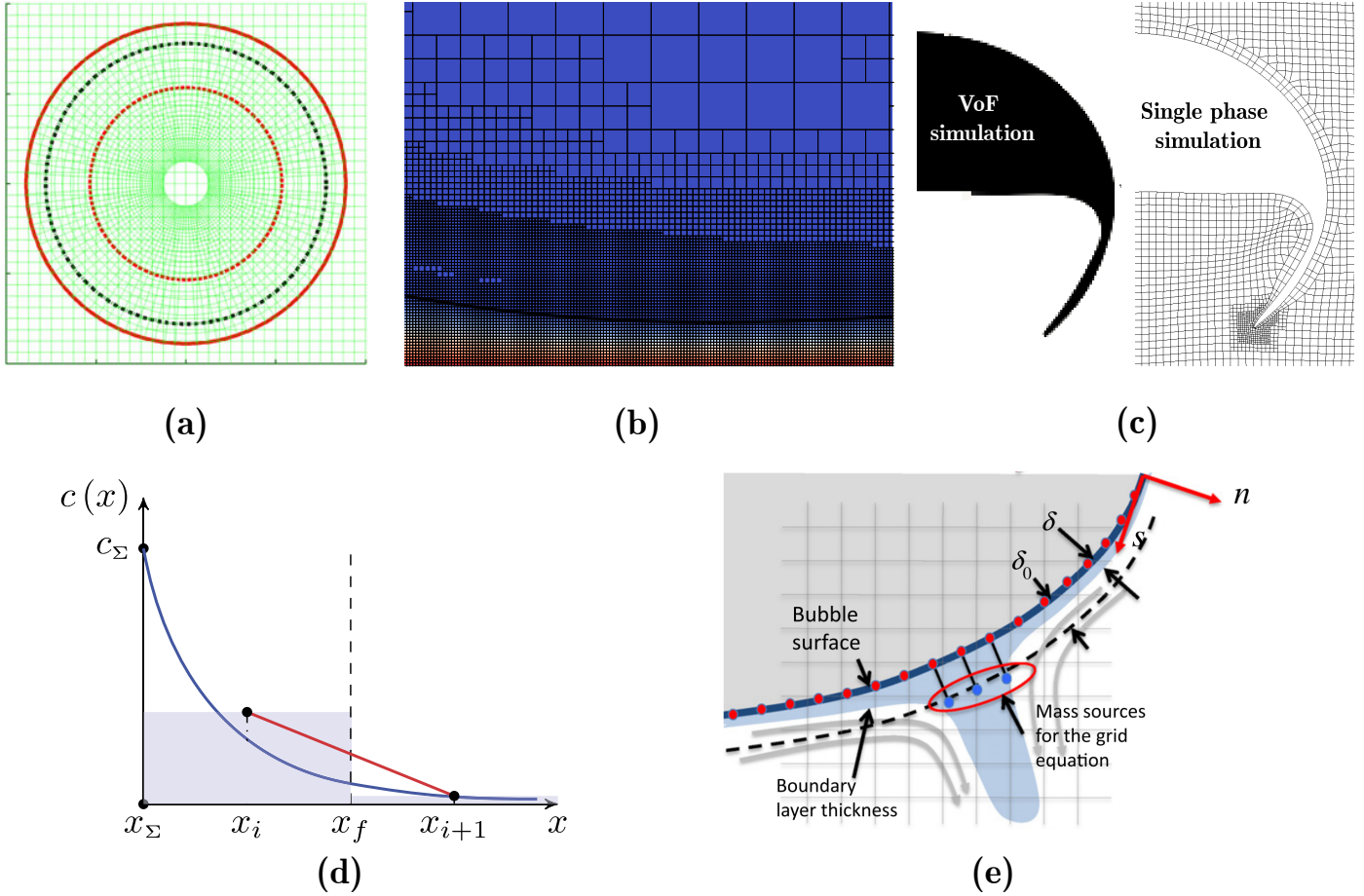


Figure 1: (a) Particle-attached mesh in polar coordinates (2D) from [22], (b) Adaptive Mesh Refinement from [23, 24], (c) VoF to single-phase simulation framework developed by Weiner [25], (d) Analytical profile fitted on the first mesh average concentration value: quasi-static approach of [26] (figure re-adapted from [26]), (e) Transient boundary layer approach developed by Aboulhasanzadeh *et al.* [27]

popular in the field of bubble dynamics and two-phase flows. Some researchers have taken advantage of Cartesian discretisation to implement AMR. It benefits from the multilevel octree representation which can be optimised to achieve better performance than classical uniformly refined meshes. State-of-the-art open source code like Basilisk [23] has been extensively used to perform phase change of droplets and bubbles [24] (see **Fig. 1.b**). However, as there is a dependency between the spatial scales and the time scale, refining the mesh locally implies penalising the overall time step. There is then always a compromise between accuracy and time calculation so there is still a need for sub-grid (in the manner of Large Eddy Simulations) and boundary layer modelling to capture most information of the flow fields.

Another novel approach developed by Weiner during his thesis, as detailed in [25], is interesting for single-rising objects and species transport. Briefly, the undertaken framework consists of realising a simulation of bubble dynamics in an axisymmetric configuration to capture its rising velocity, the local interfacial velocity and its shape. The latter parameters are reintroduced in a single-phase (ALE) simulation (see **Fig. 1.c**). The rising velocity plays the role of an inlet velocity while the interfacial velocity is applied as a Boundary Condition. The

shape is imposed over time and the mesh is adapted according to it through common ALE techniques. Several Artificial Neural Networks are used as surrogate models to represent the interface-related parameters over time. This approach allows a very high level of refinement at a low cost. This method is only applicable if the velocity field is already converged *i.e.* if the vapour-to-liquid viscosity ratio is kept low at moderate Reynolds numbers.

Finally, a new class of methods has aroused a growing interest in the scientific community of chemical transport phenomena (passive and reactive scalars). Liquid-gas systems involved in industrial applications are characterised by noticeably high mass diffusivity (high Schmidt numbers) and high levels of turbulence (high Reynolds numbers). The concentration boundary layer thickness as well as the degree of variation of the concentration near a reactive interface are directly related to the product of these two numbers (Peclet number Pe_b). The reaction rate is related to the normal concentration jump at the interface which is very similar to phase change physics. Concentration and temperature can be treated as two passive scalars as long as the phase change impact on velocity, as well as chemical reactions, are neglected.

To solve accurately these boundary layers using interface

tracking and capturing methods, dynamical regimes are sometimes chosen to be low. Some studies have been done at creeping flow ($Re \ll 1$) to access high Peclet numbers (up to 2×10^4) [26, 29].

Understanding that spatial scales taking place at the interface are much smaller and distinct from the scales involved in the mean flow, a local correction in the interface vicinity has been explored by many authors and can be classified into two categories:

- A quasi-static approach based on instantaneous fitting of the temperature field [26, 29–31].
- A transient method to track the energy contained in the temperature boundary layer over time [27, 32, 33].

These methods have been exposed and alleviate the problem of spatial refinement.

Both methods rely on an analytical solution or a form of solution to describe the scalar boundary layer. The solutions may have a physical justification or convenient properties to describe the strong scalar variation at the interface. One of the key aspects of these methods is that they rely on the fitting of a free parameter δ which is closely related to the thickness of the layer.

The quasi-static approach, also referred to as SGS model by its original authors [30], consists of fitting the free parameter at each time step to accommodate either a local scalar value or integral quantities (the amount of the corresponding extensive quantity inside the interfacial cell on the respective phase). Moreover, fluxes need to be corrected on all faces in a Finite Volume approach in order to obtain optimal results [26] (see **Fig. 1.d**). The application of the SGS model, featuring analytical profile functions, has also been employed to study mass transfer involving local volume changes in [34].

On the contrary, the unsteady approach integrates the profile over time which is appealing in the context of an unsteady simulation (*i.e.* governed by an unsteady PDE). The latter tracking of the mass (or energy) contained in the boundary layer knowing the shape of the concentration (or temperature) profile can lead to the deduction of the free parameter.

For the first class of methods, once the profile has been fitted, it is possible to enhance the scalar gradient prediction and eventually correct the fluxes in the neighbouring cells. On the contrary, the unsteady approach, described in **Fig. 1.e**, is unfortunately not a two-way coupling as the boundary layer is insensitive to the incoming fluid. Further details concerning both methods are given in **Sec. 3**. Unifying the two approaches or at least obtaining a two-way coupling for the temperature is our current research’s main objective.

Using such approaches in the presence of phase change is reasonable at moderate Jakob number $Ja \lesssim 1$ (defined in **Eq. (1)**). This dimensionless number characterises the phase change magnitude and the compression (evaporation) or dilatation (condensation) of the boundary layer as the interface is moving relatively to both fluids to accommodate the density difference.

$$Ja = \frac{\rho_l C_{pl} \Delta T_\infty}{\rho_v \left[\mathcal{L}^{vap} + (C_{pl} - C_{pv}) \Delta T_\infty \right]} \quad (1)$$

The current paper explores thermal boundary layer modelling that will be re-employed in phase change simulations or bubbly flows at saturation. However, to separate physical phenomena and to be able to compare solutions on several meshes (similar bubble mesh topology), the interfacial mass flow rate is neglected. In other words, the latent heat of vaporisation is assumed to be infinite which leads to the asymptotic Jakob number $Ja \rightarrow 0$ (more details about this hypothesis are given in **Sec. 2.1.1** and **Sec. 2.1.2**). The numerical treatment of the temperature field remains the same. On the other hand, the normal temperature gradient $\nabla T \cdot \mathbf{n}_\Gamma$ from which the mass flow rate \dot{m}_v is derived is no longer coupled to the velocity field.

The current paper first exposes the numerical method implemented in the software TrioCFD (see **Sec. 2**). Then, reference results on a single rising bubble in a sub-cooled liquid are presented. Global and local convergences on the Nusselt number are discussed depending on the grid resolution in **Sec. 2.5**. Two strategies consisting of enhancing the temperature gradient prediction are discussed and compared (see **Sec. 3**). New adaptations to thermal sub-resolutions are proposed. Finally, these approaches are applied to coarse-grained DNS results without the thermal fluxes’ feedback onto the macroscopic solution on our steady-state simulations to assess their capabilities and compare them (see **Sec. 4**). The essential components for optimising the efficiency of the sub-resolution method are meticulously identified and thoroughly examined in this study. **Sec. 5** draws the main conclusions of this work.

2 Direct Numerical Simulations

2.1 Numerical method

2.1.1 Mathematical formulation

The continuous formulation used to describe the local and instantaneous conservation of quantities *i.e.* mass, momentum, and temperature is the so-called one-fluid formulation. A single set of equations is obtained for the entire liquid-vapour domain. It is obtained using an indicator function $\chi_k \in \{0; 1\}$ to locate each phase. The system of equations involves one-fluid variables which are defined at every point of space. Any one-fluid parameter ϕ is expressed as follows:

$$\phi = \sum_{k \in \{v, l\}} \chi_k \phi_k \quad (2)$$

The overall system of equations is written in its conservative form in **Eq. (3)**. Physical properties are considered to be constant per phase, and surface tension variations, also referred to as the Marangoni effect, are neglected, *i.e.*, σ is constant. The assumptions are realistic considering the involvement of a phase change process at moderate sub-cooling

($\Delta T = \langle T_v \rangle - \langle T_l \rangle \leq 5\text{K}$ in liquid at saturation and at 155 bar leads to Jakob number value $Ja < 1$).

$$\nabla \cdot \mathbf{u} = -\dot{m}_v \left(\frac{1}{\rho_v} - \frac{1}{\rho_l} \right) \delta_\Gamma \quad (3a)$$

$$\begin{aligned} \partial_t(\rho \mathbf{u}) + \nabla \cdot (\rho \mathbf{u} \otimes \mathbf{u}) \\ = \nabla \cdot (\mathcal{D}\mathbf{u} - p\mathbf{I}) + \rho \mathbf{g} + \kappa \sigma \mathbf{n}_v \delta_\Gamma \end{aligned} \quad (3b)$$

$$\begin{aligned} \partial_t(\rho C_p T) + \nabla \cdot (\rho C_p \mathbf{u} T) \\ = \nabla \cdot (\lambda \nabla T) + \dot{m}_v \delta_\Gamma \mathcal{L}^{vap} \end{aligned} \quad (3c)$$

$$\partial_t \chi_v + \mathbf{u}_\Gamma \cdot \nabla \chi_v = 0 \quad (3d)$$

$$T_\Gamma = T|_\Gamma = T^{sat} = \text{const} \quad (3e)$$

$$\mathbf{u}_\Gamma = \mathbf{u}_l - \frac{\dot{m}_v}{\rho_l} \mathbf{n}_v \quad (3f)$$

$$\dot{m}_v = \rho_v (\mathbf{u}_v - \mathbf{u}_\Gamma) \cdot \mathbf{n}_\Gamma \quad (3g)$$

To avoid cumbersome notations, T represents the difference in temperature to the saturation one. Depending on the sign of T , we are dealing with a sub-cooled or super-heated fluid (*i.e.* the bulk fluid is below or above the saturation temperature).

$\mathcal{D}\mathbf{u}$ is the one-fluid diffusion tensor, constructed to eliminate the velocity jump at the interface ($\propto \dot{m}_v$). In fact, in the presence of phase change, the velocity field \mathbf{u} is embedding the discontinuity. This discontinuity results in a Dirac delta function δ_Γ in the expression of the one-fluid velocity gradient (see **Eq. (4)**) *i.e.* the equations are valid in the sense of the distributions.

$$\begin{aligned} \nabla \mathbf{u} &= \chi_v \nabla \mathbf{u}_v + \chi_l \nabla \mathbf{u}_l - (\mathbf{u}_v - \mathbf{u}_l) \otimes \mathbf{n}_v \delta_\Gamma \\ &= \chi_v \nabla \mathbf{u}_v + \chi_l \nabla \mathbf{u}_l - \dot{m}_v \left(\frac{1}{\rho_v} - \frac{1}{\rho_l} \right) \mathbf{n}_v \otimes \mathbf{n}_v \delta_\Gamma \end{aligned} \quad (4)$$

The viscous term of the N-S equations is obtained by a divergence operator ($\nabla \cdot \mathcal{D}\mathbf{u} \equiv \nabla \mathcal{D}\mathbf{u} : \mathbf{I}$). As a consequence, the discontinuity should be removed from the one-fluid diffusion tensor before applying the divergence operator as shown in **Eq. (5)** as the gradient of a Dirac delta function is not mathematically defined.

$$\mathcal{D}\mathbf{u} = \mu \left[\nabla \mathbf{u} + {}^T \nabla \mathbf{u} + 2\dot{m}_v \left(\frac{1}{\rho_v} - \frac{1}{\rho_l} \right) \mathbf{n}_v \otimes \mathbf{n}_v \delta_\Gamma \right] \quad (5)$$

In practice, the term used to annihilate the discontinuity due to phase change (last term proportional to \dot{m}_v in **Eq. (5)**) is not added to the diffusion operator $\mathcal{D}\mathbf{u}$; so the actual discretised one-fluid diffusion tensor $\mathcal{D}\mathbf{u}$ embeds a discontinuity. Here, in the limit of $Ja \rightarrow 0$, the effect of the phase change rate is neglected so this particular treatment has no impact on our results.

The conservation of entropy s , as well as the inequality condition on the entropy source $\Delta s \geq 0$, are translated into an interfacial temperature T_Γ equal to the saturation temperature T^{sat} at the interface. The additional hypothesis to derive this condition is to consider reversible interfacial transfers.

2.1.2 Velocity discretisation and Front-Tracking algorithm

The momentum and temperature equations are not numerically treated in the same manner. For the momentum equation, the

non-conservative form is employed and discretised over a staggered grid [35] (see **Fig. 2**). A concession is made on the dis-

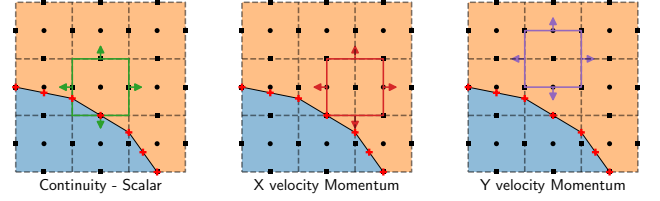


Figure 2: Marker and cells or Staggered grid discretisation: the interface is represented by Lagrangian markers (Red crosses) which are advected over time.

cretisation of the momentum equation to facilitate the numerical treatment of the discontinuity. There is no ideal solution yet and some other authors tend to separate the fluid velocity fields by building divergence-free velocity extensions [1–3]. They thus avoid the implicit treatment of the discontinuity in the Poisson equation but they have to consider it accurately.

The mixed cells are a convenient approach to make the numerical implementation much easier and give realistic results at reasonable jumps of properties. However, the meshes need to be highly refined in the interfacial regions which cause the computational cost to shoot up (hundred of cells per diameter).

In this work, an infinite latent heat, denoted as \mathcal{L}^{vap} , is considered. This hypothesis is realistic at low Jakob numbers (≤ 1), as the velocity scales in the bubbles' wakes are much larger than that of shrinking due to condensation. This will also allow us to achieve a steady heat transfer configuration. For deeper examples of numerical methods involving treatment of the velocity discontinuity, the reader may be interested in [1, 2, 36–39].

The major steps of the momentum solver are listed below:

- An intermediate velocity $\mathbf{u}^{(*)}$ is predicted explicitly without the pressure gradient term. This intermediate velocity does not respect mass conservation.

$$\begin{aligned} \mathbf{u}^{(*)} = \mathbf{u}^{(n)} + \Delta t \left[\frac{1}{\rho^{(n)}} \nabla \cdot \mathcal{D}\mathbf{u}^{(n)} - \nabla \cdot (\mathbf{u}^{(n)} \otimes \mathbf{u}^{(n)}) \right. \\ \left. - \mathbf{g} + \frac{\sigma}{\rho^{(n)}} \kappa^{(n)} \mathbf{n}_v^{(n)} \nabla \chi_v^{(n)} \right] \end{aligned} \quad (6)$$

- A pressure correction step is undertaken to project $\mathbf{u}^{(*)}$ onto the space of zero divergence:

$$\nabla \cdot \left(\frac{1}{\rho^{(n)}} \nabla p^{(n+1)} \right) = \nabla \cdot \mathbf{u}^{(*)} \quad (7)$$

Conservation of the momentum is not ensured as the density at time $t^{(n)}$ is used in the Poisson equation and the surface tension force is not conservative.

- The interface is advected by the velocity field $\mathbf{u}^{(n+1)}$, interpolated at each marker's location.
- To ensure mass conservation, a discrete Eulerian indicator function is advected algebraically. Markers are then shifted in an iterative process until the overall vapour volume is conserved [13].

- To conserve the topology of the interface and a uniformly distributed surface mesh, several routines are used. Smoothing, point addition and removal are performed to satisfy an empirical ideal length criterion and ensure a smooth curvature locally and a correct aspect ratio. The number of markers is limited voluntarily to avoid the establishment of a zig-zag surface [10, 13].

To reduce parasitic currents as much as possible, the curvature is computed using a differential approach. Computing the curvature is a key aspect of the numerical stability of the interface. Early work of Mathieu [9] proved the existence of a discrete equilibrium by considering that the potential energy of deformation is balancing with the surface energy *i.e.* coming from the Laplace pressure jump. Volume and surface differentials are calculated using normed vectors associated with each facet's markers and this method has proved to be effective for various problems.

The diffusion operator is 2^{nd} -order (centred) whereas a QUICK advection scheme is employed. The temporal scheme is an Euler explicit. The time step is kept low to ensure stability. As a consequence, it remains smaller than the Courant (CFL) and Fourier (Fo) time steps. Many stability criteria are available to avoid non-physical high-frequency noise on the interfacial mesh [40]. For the finest mesh at 90 cells per bubble diameter ($Re_b = 62.5$), the surface-tension related time-step [41] writes:

$$\Delta t_\sigma = \sqrt{\frac{\rho_v + \rho_l}{2\pi} \frac{\Delta_{x,y,z}^3}{\sigma}} \approx 1 \times 10^{-4} \text{s} \quad (8)$$

Such criterion will be later investigated in the presence of phase-change which can intensify the instabilities due to the velocity jump.

2.1.3 A special treatment for temperature: the ghost fluid approach

Contrary to the treatment of velocity discretisation, there is a clearer consensus regarding the treatment of temperature in interface tracking methods. Because bubbles commonly have a lower viscosity than the liquid, the velocity converges faster than the temperature due to the low shear at the bubbles' interface. The viscosity ratio plays an important role in the velocity variations in the vicinity of the interface. Unlike wall-bounded flows (where there is no slip velocity), the Peclet number Pe is insufficient to connect the velocity and thermal boundary layer thicknesses. A Peclet number of unity does not yield the same numerical error for both velocity and temperature, depending on the viscosity jump and on the thermal interfacial condition (for instance saturation).

Authors are usually solving for two separated and extended fields in the presence of phase change [1–3]. Numerical methods benefit from the constant saturation temperature condition which allows linking both temperature fields. As the physical process of phase change in bubbles after wall departure is almost at a constant temperature, the vapour temperature variations are often negligible. In the rest of this work, only the liquid temperature T_l is resolved. Numerical configurations in line

with this hypothesis are later discussed in **Sec. 2.2** and **Sec. 4** and are presented in **Tab. 1** and **Tab. 2**.

Some authors such as Bothe *et al.* or Cai *et al.* [26, 31] use geometric VoF advection which enables the resolution of two-phase variables within mixed cells (cut-cells approach). The adaptation to Front-Tracking, however, presents specific challenges concerning the advection step, particularly in cases where an interface portion is either entering or exiting a cell (fluxes reconstruction).

Solving the temperature fields separately raises new requirements in terms of numerical methods as the employed meshes are not fitted to the interface. The common single-phase convection and diffusion operators are very convenient to use. They involve large stencils which thus straddle the interface even if one wants to use them for one phase only. Consequently, a spreading procedure is necessary to populate, on a finite thickness, the mixed cells and the neighbouring phase domain referred to as the "ghost" domain (superscript $.^g$). Continuous extended liquid velocity \mathbf{u}_l^{ext} and temperature T_l^{ext} are expressed as follows:

$$\mathbf{u}_l^{ext} = \mathbf{u}_l \chi_l + \mathbf{u}_l^g \chi_v \quad (9a)$$

$$T_l^{ext} = T_l \chi_l + T_l^g \chi_v \quad (9b)$$

The temperature equation written in terms of extended fields writes:

$$\frac{\partial T_l^{ext}}{\partial t} + \nabla \cdot (\mathbf{u}_l^{ext} T_l^{ext}) = \alpha_l \Delta T_l^{ext} \quad (10)$$

The interfacial saturation condition is implicitly imposed on the liquid temperature at the interface during a spreading procedure. This procedure is a key aspect of the method. Several steps are necessary to extend the temperature. They can be summarised as follows:

- Pure liquid cells and mixed cells neighbours are localised.
- To avoid an excessive amount of computational time, the normal vector as well as the distance function, associated with a pure cell, are computed approximately in a certain interface vicinity. The normal vectors \mathbf{n}_Γ are first computed in the mixed cells. Then, \mathbf{n}_Γ values are spread out iteratively from near to far by a neighbourhood averaging procedure.
- The distance to the interface is not calculated in the form of a minimisation problem $d_i = \min_{\mathbf{x}_\Gamma, \mathbf{n}_\Gamma} (\mathbf{x}_c - \mathbf{x}_\Gamma) \cdot \mathbf{n}_\Gamma$. Instead, the normal distance is calculated iteratively starting from mixed cells and sweeping the space inward and outward of the bubble. The Cartesian grid spacing is used to determine the normal distance once projected in the normal direction.
- A continuous field of mean curvature can be established using the normal vector field as in Level-Set approaches (LS):

$$\kappa = -\nabla \cdot \mathbf{n}_\Gamma = -\text{Tr}(\nabla \mathbf{n}) = \kappa_1 + \kappa_2 \quad (11)$$

- We define a local radial coordinate system with a varying

parameter \check{r} such that $r = \check{r} + R$ and $\partial_{\check{r}}^n \equiv \partial_r^n, \forall n \in \mathbb{N}$. $\check{r} = 0$ locates the interface position while R is the equivalent bubble radius related to the curvature by $\kappa = 2/R$. The normal temperature gradient at the interface is computed in these first cells using the saturation temperature and the pure liquid cell temperature located at distance $\check{r} = d_i$. Instead of considering the first-order evaluation of this numerical derivative *i.e.* at the interface, we are considering its second-order evaluation at $\check{r} = d_i/2$ (see **Fig. 3**). Then,

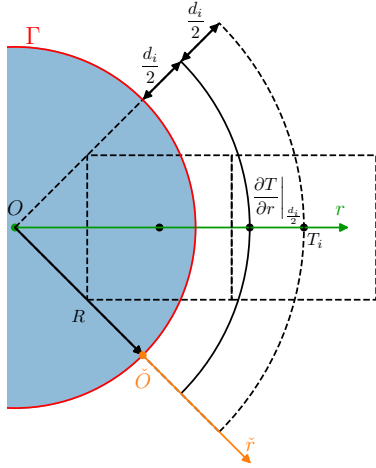


Figure 3: Normal temperature gradient calculation in the vicinity of the mixed cell. The coordinate system is such that $r = R + \check{r}$ and $\partial_{\check{r}}^n \equiv \partial_r^n, \forall n \in \mathbb{N}$. The cell size is exaggerated to emphasize the procedure.

a sub-grid pure diffusion model $\Delta_{sph}T = 0$ written in the local spherical coordinate system (see **Eq. (12)**) is used to correct the temperature gradient evaluated at the interface. The Dirichlet boundary condition is thus implicitly imposed at this particular step.

$$\Delta_{sph}T = \frac{2}{R + \check{r}} \frac{\partial T}{\partial r} + \frac{\partial^2 T}{\partial r^2} \approx \kappa \frac{\partial T}{\partial r} + \frac{\partial^2 T}{\partial r^2} = 0 \quad (12)$$

The analytical solution for the temperature gradient is straightforwardly found and approximated for numerical evaluation by **Eq. (13)**.

$$\frac{\partial T}{\partial r}(\check{r}) = \frac{\partial T}{\partial r} \Big|_{\frac{d_i}{2}} e^{-\kappa(\check{r} - \frac{d_i}{2})} \approx \frac{T_i - T_{sat}}{d_i} e^{-\kappa(\check{r} - \frac{d_i}{2})} \quad (13a)$$

$$\frac{\partial T}{\partial r}(\check{r}) = \frac{T_i - T_{sat}}{d_i} \times \left[1 - \kappa \left(\check{r} - \frac{d_i}{2} \right) \right] + o(\check{r}) \quad (13b)$$

$$\frac{\partial T}{\partial r} \Big|_{\Gamma} = \frac{\partial T}{\partial r} \Big|_{r=R} = \frac{\partial T}{\partial r} \Big|_{\check{r}=0} \quad (13c)$$

- Pure liquid cells can then be populated with the corrected interfacial gradient $\frac{\partial T}{\partial r} \Big|_{\Gamma}$. A spreading procedure similar to the curvature is undertaken to store the interfacial gradient in a finite thickness including the interface. This procedure is illustrated in **Fig. 4**.
- Once a continuous field of the gradient has been constructed, the temperature in the ghost field can be com-

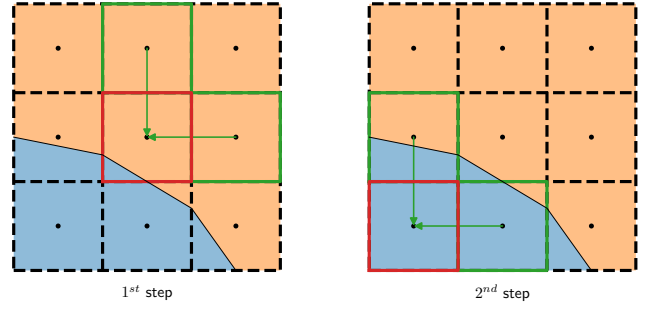


Figure 4: Spreading procedure to populate the interface neighbouring cells with the normal temperature gradient $\frac{\partial T}{\partial r} \Big|_{\Gamma}$. $\frac{\partial T}{\partial r} \Big|_{\Gamma}$ is initially evaluated locally for pure liquid cells (Green). Then the neighbouring mixed cells (Red) are populated with an average value of the normal temperature gradient. The spreading procedure keeps going in the ghost domain.

puted according to **Eq. (14)**.

$$T(\check{r}) = T_{sat} + \frac{1}{\kappa} \frac{\partial T}{\partial r} \Big|_{\Gamma} (1 - e^{-\kappa\check{r}}) \quad (14a)$$

$$T(\check{r}) = T_{sat} + \check{r} \frac{\partial T}{\partial r} \Big|_{\Gamma} \times \left[1 - \frac{\kappa\check{r}}{2} + \frac{\kappa^2\check{r}^2}{6} + o(\check{r}^2) \right] \quad (14b)$$

- A discrete divergence-free velocity field $\mathbf{u}_i^{g(d)}$ is established in presence of phase change. At $Ja \rightarrow 0$, the one-fluid velocity is continuous across the interface (not its derivatives) and the pure vapour (subscript \cdot_v) or mixed cells (subscript \cdot_m) velocity fields are used as an extension:

$$\mathbf{u}_i^{ext(d)} = \mathbf{u}_i^{(d)} \cup \mathbf{u}_i^{g(d)} = \mathbf{u}_i^{(d)} \cup \mathbf{u}_v^{(d)} \cup \mathbf{u}_m^{(d)} \quad (15)$$

High-order convection schemes (Quick) are favoured to ensure the capture of strong variations in the interface vicinity.

Once the temperature has been properly extended, the convection and diffusion can be evaluated at time (n) and the temperature is then advanced to the next time step straightforwardly:

$$T_l^{(n+1)} = T_l^{ext(n)} + \Delta t \left[\alpha_l \Delta T_l^{ext(n)} - \nabla \cdot (\mathbf{u}_l^{ext(n)} T_l^{ext(n)}) \right] \quad (16)$$

One can note that the temperature field $T_l^{(n+1)}$ is only valid in pure liquid cells. In mixed cells, the temperature field is extended at each time step. Such systematic correction can be referred to as a quasi-static approach because the local temperature field near the interface is then the solution to the steady diffusion equation $\Delta_{sph}T = 0$. Seeing that the sub-grid model is pure diffusion, the flux balance in the ghost cells is, in a sense, not predicted.

When the interface is leaving a cell, the temperature increment is not necessarily predicted well. There may still be a need to correct both the convective and diffusive fluxes as well as the mixed temperature values.

In other words, the cell is almost fully liquid before becoming pure.

Many authors rely on other methods such as the Aslam n^{th} order extrapolation [42]. It necessitates solving for n^{th} supplementary advection equations over a pseudo-time τ , starting from the highest-order normal derivative. The saturation temperature should then be imposed through an implicit diffusion scheme [1] which takes into account the interface position. It involves particular schemes to keep convenient matrix properties [37].

2.2 Numerical configurations

To perform temperature boundary layer modelling, it is necessary to generate DNS reference results that are fully converged: both global (integral) and local high-order quantities (gradients, second-order tensors) must be converged.

A bubble kept at a constant temperature and rising in a finite domain has been simulated until steady-state. Outflow boundary conditions for velocity and temperature are necessary to obtain a steady solution. They assume the normal diffusive fluxes are zero at the domain boundaries (*i.e.* the momentum and the heat flux are only transported outside the domain).

Moderate Reynolds and Prandtl numbers are aimed for our study. Instead of working directly with the Reynolds number, the modified Archimedes number Ar_b^* also referred to as the Galilei number is used. In dispersed two-phase flows, the characteristic velocity is often chosen to be the terminal velocity of the dispersed phase. The rising velocity is not imposed by a boundary condition but is determined *a posteriori*. To observe the convergence of the velocity field and interfacial shear depending on the increasing spatial refinement, the Archimedes number defined in **Eq. (17)** is used.

$$Ar_b = g \frac{\rho_l - \rho_v}{\rho_l} \frac{D_b^3}{\nu_l^2} = Ar_b^{*2} \quad (17)$$

This dimensionless number combines the viscous and buoyancy contributions. Ar_b^* reveals to be the same order of magnitude as the bubble Reynolds number in practice.

A set of two Archimedes numbers is used: $Ar^* \in \{10; 50\}$. Several liquid Prandtl numbers $Pr_l \in \{1; 2.5; 5\}$ are simulated to observe the effect of the boundary layer thickness on the interfacial quantities and the ability of the method to correct the local temperature gradient profiles. For the sake of comparison, it is worth noting that sub-grid approaches have been rigorously evaluated across a Prandtl number spectrum spanning from 1×10^1 to 1×10^7 in various works, as evidenced by studies conducted by Bothe *et al.* and Weiner *et al.* [26, 29]. In this work, larger boundary layers are considered. The Eötvös number, which determines the bubble aspect ratio (deformation), is chosen to be low ($EO = 0.1$) to keep the bubble spherical. We expect that the stall behind the bubble will appear faster for an oblate spheroid (later for a prolate spheroid) as the fluid streamlines will be increasingly perturbed by the rising object.

The other dimensionless numbers that influence the transfer are chosen such that the vapour-liquid combination corresponds to water at saturation at 155 bar [43]. The physical parameters

are summarised in **Tab. 1**. The ratio of density does not directly influence the results as shown by the work of Feng *et al.* [44, 45] on translating viscous spheres. In realistic scenarios, the ratio of density for a fixed bubble size is conditioning the rising velocity and the Reynolds number.

Table 1: Dimensionless parameters for the set of simulations $Ar^* \in \{10; 50\}$, $Pr_l \in \{1; 2.5; 5\}$

Dimensionless Parameters	Notation	Expression	Values - Range
Controlled	Archimedes	$Ar_b^* = \sqrt{Ar_b} \left(g D_b \frac{\rho_l - \rho_v}{\rho_l} \right)^{1/2} \frac{D_b}{\nu_l} = \frac{U_{term}^{pred} D_b}{\nu_l}$	{10; 50}
	Prandtl	$Pr_l = \frac{\rho_l c_{p,l}}{\mu_l} \frac{\lambda_l}{\sigma}$	{1; 2.5; 5}
	Jakob	$Ja_b = \frac{\rho_l c_{p,l} \Delta T}{\rho_v \mathcal{L}^{vap}}$	$\rightarrow 0$
	Eötvös	$EO_b = f(We, Fr, \rho_v) = \frac{\Delta \rho g D_b^2}{\sigma} = \frac{We}{Fr^2} = \frac{\rho_v g D_b^2}{\sigma}$	0.1
	Morton	$Mo_b = \frac{We^3}{Fr^2 Re_b^4} = \frac{g \mu_l^4 (\rho_l - \rho_v)}{\rho_l^2 \sigma^3}$	$\{1.0 \times 10^{-7}; 1.6 \times 10^{-10}\}$
Measured	Reynolds	$Re_b = \frac{\rho_l U_{term} D_b}{\mu_l} = \frac{U_{term} D_b}{\nu_l}$	{3.6; 62.5}
	Weber	$We_b = \frac{\rho_l U_{term}^2 D_b}{\sigma}$	{0.013; 0.16}
	Froude	$Fr_b^* = Fr_b^2 = \frac{U_{term}^2}{g D_b}$	{0.3; 1.14}

Table 2: Geometrical and physical parameters for the set of simulations $Ar^* \in \{10; 50\}$, $Pr_l \in \{1; 2.5; 5\}$. Liquid-vapour at saturation and at 155 bars.

Parameters	Notation	Unit	Values - Range	
Geometrical	Bubble diameter	D_b	mm 2	
	Cells per bubble diameter	$\Delta_{x,y,z}$	-	{12, 16, 24, 33, 48} ; $Ar^* = 10, Pr_l = 1$ {16, 24, 33, 48, 67, 96} ; $Ar^* = 10, Pr_l = 2.5$ {24, 33, 48, 67, 96} ; $Ar^* = 10, Pr_l = 5$ {16, 22, 32, 45, 64} ; $Ar^* = 50, Pr_l = 1$ {22, 32, 45, 64, 90} ; $Ar^* = 50, Pr_l = 2.5$ {22, 32, 45, 64, 90} ; $Ar^* = 50, Pr_l = 5$
		Domain size	$\Omega_{x,y,z}$	D_b
	Ω_l	Viscosity	μ_l	Pa s 6.82×10^{-5}
		Density	ρ_l	kg m^{-3} 594.4
Conductivity		λ_l	$\text{W m}^{-1} \text{K}^{-1}$ 0.69	
Specific heat capacity		$C_{p,l}$	$\text{J kg}^{-1} \text{K}^{-1}$ 10 110	
Ω_v	Viscosity	μ_v	Pa s 2.3×10^{-5}	
	Density	ρ_v	kg m^{-3} 101.9	
	Conductivity	λ_v	$\text{W m}^{-1} \text{K}^{-1}$ 0.14	
	Specific heat capacity	$C_{p,v}$	$\text{J kg}^{-1} \text{K}^{-1}$ 14 001	
Γ	Latent heat	\mathcal{L}^{vap}	J kg^{-1} ∞	
	Surface tension	σ	N m^{-1} 3.91×10^{-6}	
Ω	Gravity	g	m s^{-2} { 2×10^{-4} ; 4.97×10^{-3} }	

2.3 Qualitative outcomes

The simulations have been performed in 3D although the numerical configurations are 2D-axisymmetric. It is justified by the fact that complex 3D simulations are aimed at and will benefit from our boundary layer approach. Cartesian grid principal directions, interface portions' positions and angles cause a dispersion of the results as the numerical schemes' precision is directly impacted.

Two snapshots of the dimensionless temperature fields (denoted Θ , see **Eq. (18b)**) are plotted in **Fig. 5.a** and **Fig. 5.b**. For a single bubble rising in an infinite medium, it is possible to proceed to an overall non-dimensionalisation for the temperature using the far-field temperature T_∞ and a reference temperature T_0 (the interface temperature at saturation). In the case of

sub-cooling, it corresponds to ΔT_{sub} :

$$\Delta T_{sub} = T^{sat} - T_{\infty} = -\min(T) \quad (18a)$$

$$\Theta = \frac{T - T_{\infty}}{T_0 - T_{\infty}} = \frac{T - T_{\infty}}{T^{sat} - T_{\infty}} \in [0, 1] \quad (18b)$$

It can be observed that the boundary layer at $Ar^* = 10$ reaches the domain's boundaries. As a consequence, it is expected that the boundary conditions slightly influence the temperature field. However, it will not cause any problem to investigate our methods. The converged results are used to evaluate the ability of the method to enhance the temperature gradient. Our approach focuses on local enhancements but we are not expecting it to correct the compression of the boundary layer induced by the domain size.

At the highest Archimedes number ($Ar^* = 50$), the box has been chosen to be larger and longer to capture more precisely the thermal wake.

We can see that the bubble top region necessitates a very high refinement to capture the boundary layer thickness. According to the interface position and the mixed cell regions (a strip with a thickness of plus or minus one mesh's diagonal), it can be deduced that the mixed cell region thickness is large compared to the boundary layer thickness. The interfacial cells which appear to be a strength in terms of ease of implementation become a source of errors where quantities are spread.

2.4 General comments

2.4.1 Bubble rising velocity

The simulation aims to keep the bubble steady in the domain through the use of a variable inlet velocity boundary condition over time. For each dynamical regime explored, a first simulation has been done using the coarser mesh and a constant inlet velocity U_{term}^{pred} predicted roughly using the modified Archimedes number re-written to mimic a Reynolds number.

$$Ar_b^* = \sqrt{Ar_b} = \sqrt{g D_b \frac{\rho_l - \rho_v}{\rho_l} \frac{D_b}{\nu_l}} = \frac{U_{term}^{pred} D_b}{\nu_l} \quad (19)$$

The bubble has been stabilised in the domain but a minor component of its vertical velocity can remain because the parameters chosen to stabilise the bubble have been measured on the coarser simulations where the velocity boundary layer is not converged. In other words, if the velocity gradient is not captured well on both sides of the interface, the shear between both phases is underestimated. Such local errors, once integrated, are responsible for a bubble's relative velocity error.

Authors such as Weiner *et al.* [25] used a similar technique while imposing the tangential velocity in a single fluid simulation. It makes it possible to keep the bubble almost stationary over its transient phase.

In this paper, any post-processing of velocity is performed at a steady state in the bubble's reference frame, *i.e.* by removing the residual bubble velocity in the simulation frame of reference.

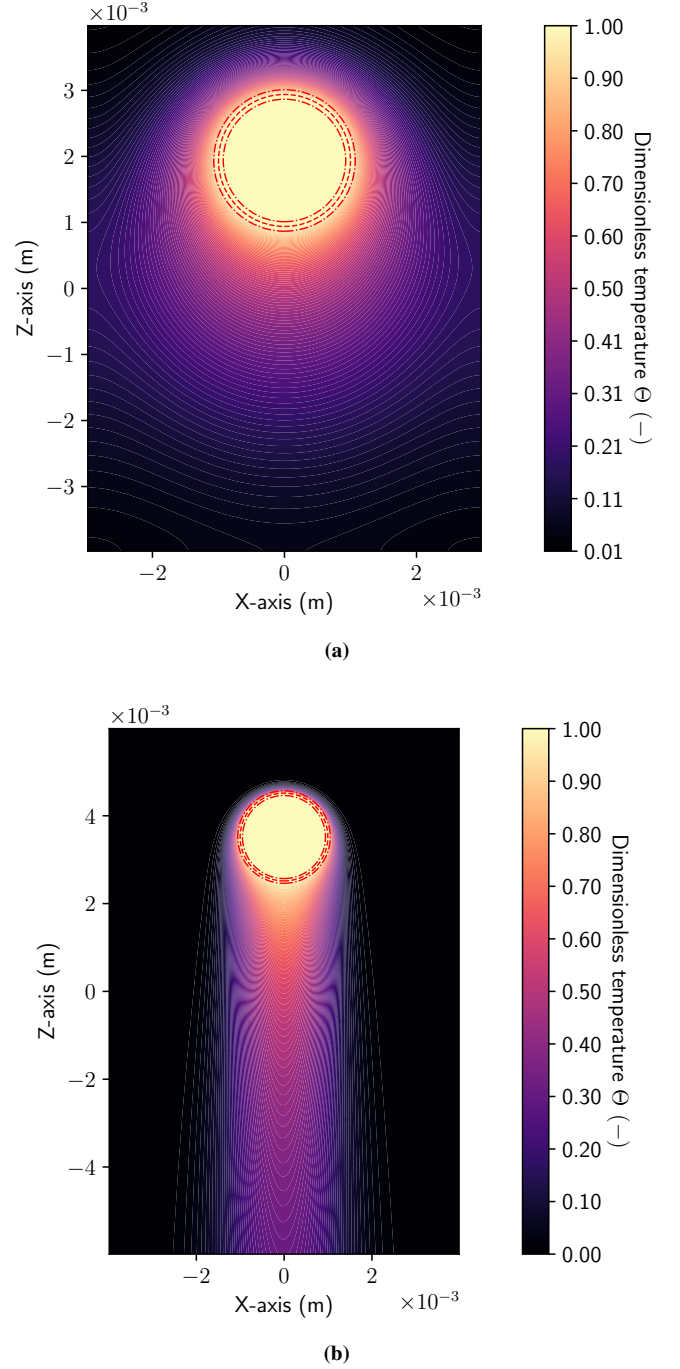


Figure 5: Final snapshots of the temperature fields for two cases to observe qualitatively the boundary layer thicknesses' dependency in Re_b . The red dashed line represents approximately the interface position whereas the two red lines (alternating dashes and dots) represent the contraction and dilation of

the interface by a distance of a cell diagonal $\pm \sqrt{\Delta_x^2 + \Delta_y^2 + \Delta_z^2}$

$$(a) Ar_b^* = 10, Re_b \approx 3.6, Pr_l = 1, \frac{D_b}{\Delta} = 48,$$

$$(b) Ar_b^* = 50, Re_b \approx 62.5, Pr_l = 1, \frac{D_b}{\Delta} = 64$$

2.4.2 Velocity profiles and drag coefficient value

A similar approach can be undertaken on the three components of the velocity field. The Cartesian velocity vector field

$\mathbf{u} = (u_x, u_y, u_z)$ can be projected onto each local facet coordinate system $(\tilde{\mathbf{e}}_r, \tilde{\mathbf{e}}_\theta, \tilde{\mathbf{e}}_\phi)$. This basis of vectors is associated with the osculating sphere of radius R .

The drag coefficient value is determined through a basic balance of forces applied to the rising bubble. Buoyancy (Pressure forces), gravity and drag forces are balancing at equilibrium and lead to the simple expression of drag coefficient C_d presented in Eq. (20). It entirely handles the physical complexity and is a function of several dimensionless parameters in the case of viscous bubbles: $C_d(Re, \mu_v/\mu_l, \rho_v/\rho_l)$.

$$C_d = \frac{2\Delta\rho g V_b}{\rho_l S_b^p U_{term}^2} = \frac{4}{3} \left(\frac{\rho_l - \rho_v}{\rho_l} \right) \left(\frac{g D_b}{U_{term}^2} \right) \quad (20a)$$

$$S_b^p = \frac{\pi}{4} D_b^2 \quad (20b)$$

$$V_b = \frac{\pi}{6} D_b^3 \quad (20c)$$

S_b^p is the cross-sectional surface area also known as the frontal area and V_b is the bubble volume.

In our case, the bubble terminal velocity is subdivided into two parts. The liquid inlet velocity U_{term}^{inlet} corresponds to the ideal bubble rising velocity as a Galilean transformation has been performed to work in the frame of reference of the bubble.

Measured values of the Drag coefficient C_d are exposed in **Tab. 3** and compared to the correlation of Feng *et al.* computed as Eq.23a in [45]. For the lowest Archimedes number $Ar^* = 10$, the finest mesh ($D_b/\Delta = 96$) value of drag is well predicted *i.e.* within a range of 3% around the correlation value. For the highest Archimedes number, a constant drag coefficient value is obtained with an accuracy of 15%. Domain size has surely an influence on the shear at the interface but the velocity field is resolved enough to perform our approach.

Table 3: Drag coefficients measured for each dynamic and spatial resolution. RF stands for refinement.

Archimedes number (Ar^*)	Spatial refinements	RF-1	RF-2	RF-3	RF-4	RF-5	Theoretical
10	Resolutions $\frac{D_b}{\Delta}$	12	16	24	33	48	
	Drag coefficient	11.06	10.81	10.59	10.49	10.42	10.82
50	Resolutions $\frac{D_b}{\Delta}$	16	22	32	45	64	
	Drag coefficient	0.85	0.84	0.84	0.84	0.85	0.74

2.4.3 Temperature error field

A post-processing tool has been developed to estimate the temperature error locally (see **Fig. 6**). A finer solution is interpolated on the coarse mesh cell centres and displaced to match the bubbles' centres. The error in the restricted domain Ω_ϵ (see **Eq. (21.a)**) is expressed by **Eq. (21.b)**.

$$\Omega_\epsilon = \Omega_{coarse} \cap \Omega_{fine} \quad (21a)$$

$$\epsilon_\phi = \left| \frac{\phi_{coarse} - \phi_{fine}}{\phi_{coarse}} \right| \times 100 \quad (\%) \quad (21b)$$

An example of the relative error is shown on two perpendicular planes in **Fig. 6a** and **Fig. 6b** for $Ar^* = 50$, $Pr_l = 1$ and $\frac{D_b}{\Delta}|_{coarse} = 16$, $\frac{D_b}{\Delta}|_{fine} = 64$.

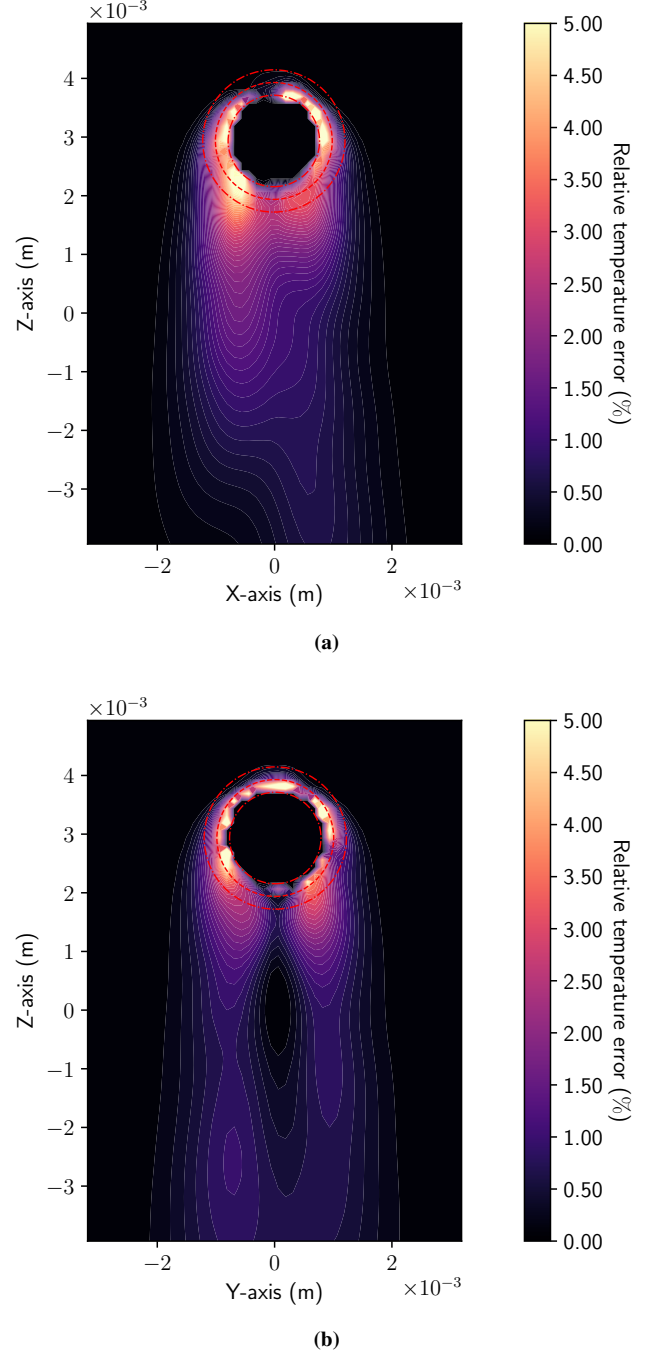


Figure 6: Temperature error field on two perpendicular planes: (a) ZX plane, (b) YZ plane. Both planes are approximately centred at $y = 0$ and $x = 0$, respectively. The maximum colour bar level is 5%. The error has been calculated between mesh resolutions of $D_b/\Delta = 16$ and $D_b/\Delta = 64$ at $Pr = 1$ and $Ar^* = 50$.

It can be seen in both figures that the relative temperature error is significantly below 5% (from a local temperature point of view). However, in the mixed cells, the error is increasing significantly. The presence of mixed cells does not affect the interfacial region's thickness the same way for coarse and fine mesh solutions. The extended temperature field established using a pure-diffusion model is impacting a larger region on the

coarse mesh.

Although the flow should theoretically exhibit axisymmetry, the Front-Tracking method generates a triangular mesh unconstrained by the Cartesian grid, resulting in a numerical setup that lacks inherent axisymmetry. Furthermore, the number of nodes in this triangular mesh depends significantly on the resolution of the Cartesian mesh, as detailed in the numerical strategy (see **Sec. 2.1.2**). The coarse and fine Lagrangian meshes do not align and lack a common axis of symmetry.

These phenomena contribute to the irregular patterns, especially pronounced in the wake of the bubble and at the interface.

The temperature field, which is a zeroth order quantity, is converged globally (under 5%) from the coarsest simulation. It is later confirmed while observing the radial profiles of the temperature depending on the spatial resolution (**Sec. 4.1.2**, **Fig. 16a**). The far-field temperature will be used as an input (to fit an analytical profile in **Sec. 4.2** or as a boundary condition in **Sec. 4.3**). As a consequence, it reinforces our trust in an *a priori* methodology (later exposed in **Sec. 3**).

Although the normal temperature gradient is not predicted well at the interface using the coarse grid, the error is not spread in the domain; it is contained in the interface's vicinity. In other words, the temperature error will have a reduced effect on the assessment of the method. Such local data is rarely post-processed and available in the literature due to the Lagrangian aspect of the method. The Python library developed for this purpose will be re-employed in future work involving multi-bubble configurations.

2.5 Global and local convergence of the temperature gradient and the Nusselt number

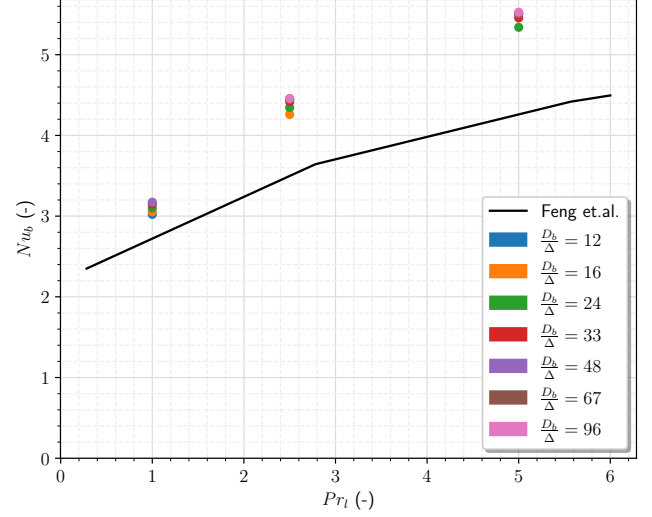
To evaluate the convergence of the simulations, the steady-state bubble Nusselt number Nu_b has been measured by integrating the normal temperature gradient at the interface Γ . Both the continuous $\cdot^{(c)}$ and discretised $\cdot^{(d)}$ expressions of the Nusselt number are summarised in **Eq. (22)**.

$$\begin{aligned}
 Nu_b^{(c)} &= \frac{hD_b}{\lambda_l} = \frac{D_b Q_{\text{vap} \rightarrow \text{liq}}}{\lambda_l \Delta T S_\Gamma} \\
 &= \frac{D_b}{\Delta T S_\Gamma} \int_\Gamma \nabla T_l^g \cdot \mathbf{n}_\Gamma dS \\
 Nu_b^{(d)} &= \frac{D_b^{(d)}}{\Delta T \sum_k^{\text{Facets}} S_k} \sum_k \nabla T_l^g \cdot \mathbf{n}_\Gamma^k S_k \\
 &= \frac{D_b^{(d)}}{\Delta T S_\Gamma^{(d)}} \sum_k \nabla T_l^g \cdot \mathbf{n}_\Gamma^k S_k
 \end{aligned} \tag{22}$$

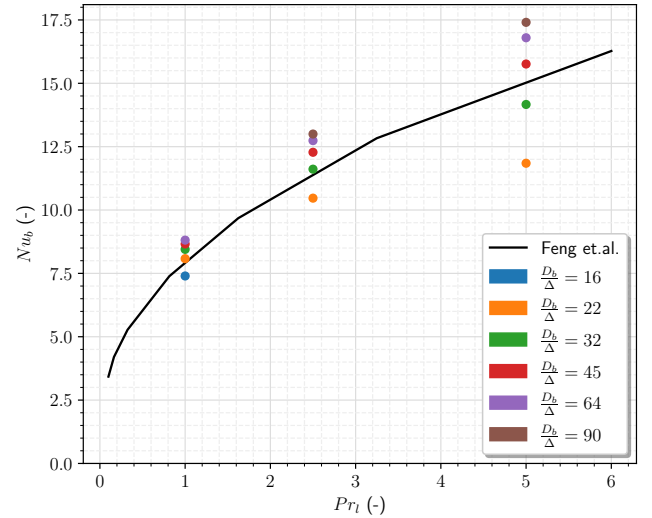
The global bubble Nusselt number measured for each simulation is plotted depending on the Prandtl number in **Fig. 7a** and **Fig. 7b**. The reference correlation has been chosen to be the one of Feng and Michaelides [44]. They performed a numerical simulation on a single translating bubble. Their innovative approach consists of solving for the stream and vorticity functions by finite difference. They were able to stretch the coordinate system through a change of variables which gives access to better accuracy at a lower cost. They managed to obtain a

minimum spatial resolution of $1/1000$ of the bubble radius in the layer whereas the domain size is 75 bubble's diameter large.

Fig. 7 shows first a good convergence of our numerical results and a reasonable agreement with respect to the reference correlation appearing as Eq.29a in [44]. The larger deviation observed at $Ar_b^* = 10$ can be attributed to the stronger impact of the different B.C.s used.



(a)



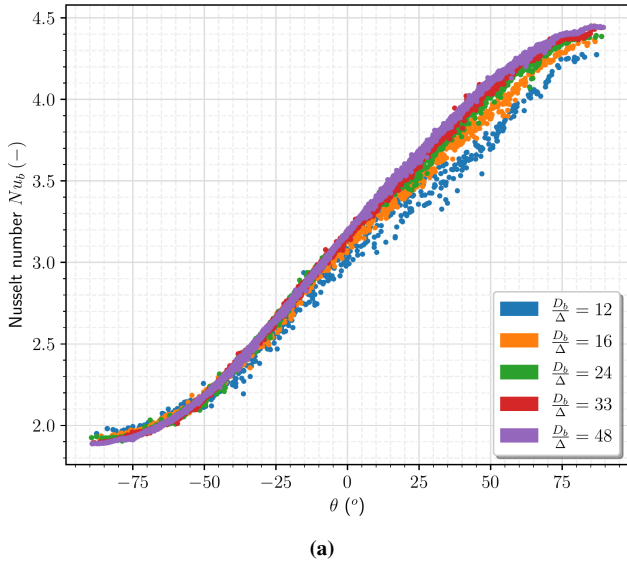
(b)

Figure 7: Bubble overall Nusselt numbers measured for several Prandtl numbers at two dynamical regimes. The modified Archimedes numbers Ar_b^* are evaluated using the physical parameters in **Tab. 2** while the bubble Reynolds number Re_b is computed *a posteriori* according to the liquid-vapour relative velocity (\equiv bubble terminal velocity U_{term}). The reference correlation appears as Eq.29a in [44].

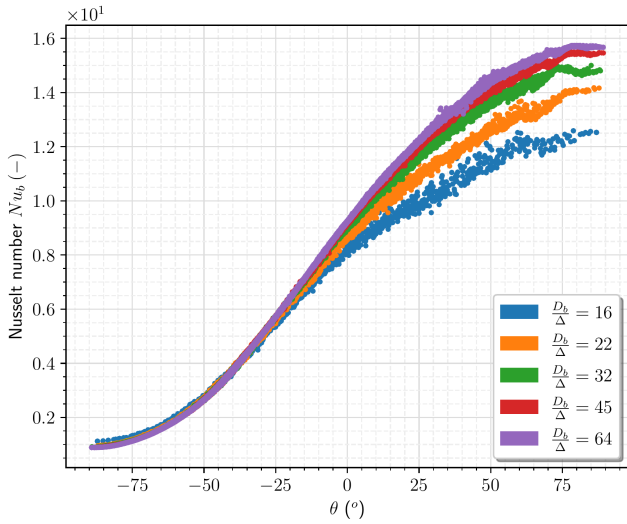
(a) $Ar_b^* = 10$ and $Re_b \approx 3.6$, (b) $Ar_b^* = 50$ and $Re_b \approx 62.5$

It is possible to compute the temperature gradient at the interface by computing an Eulerian gradient field using a second-order centred operator and interpolating it at each facet's centroid using a Tri-linear operator (1st order interpolation, 8 points in 3D). To observe the local convergence of the tempera-

ture gradient, the Nusselt number $Nu_b^{(l)}$ depending on the bubble elevation parameter θ has been plotted in **Fig. 8a** and **Fig. 8b**.



(a)



(b)

Figure 8: Local Nusselt number depending on the bubble elevation parameter $\theta \in [-90; 90]^\circ$.
(a) $Ar_b^* = 10$, $Re_b \approx 3.5$ and $Pr_l = 1$,
(b) $Ar_b^* = 50$, $Re_b \approx 62.5$ and $Pr_l = 1$

It can be seen that at low Reynolds and Prandtl numbers (see **Fig. 8a**), the local convergence is roughly obtained at a reasonable cost (from 33 cells per diameter) whereas the convergence is more costly at $Re_b \approx 62.5$ reaching 64 elements per diameter.

Increasing the Prandtl number up to 5.0 is demanding more than 90 elements to converge properly (see **Fig. 9**). At higher Prandtl numbers, some oscillations are visible at the bubble top where $\theta \approx 90^\circ$. Similar observations have been done on the numerical results of Bothe *et al.* [29]. The origin of the oscillations is numerical. It does not come from the post-processing approach but rather from the resolution itself. Bothe *et al.* argued that in the region of oscillations, the boundary layer is the

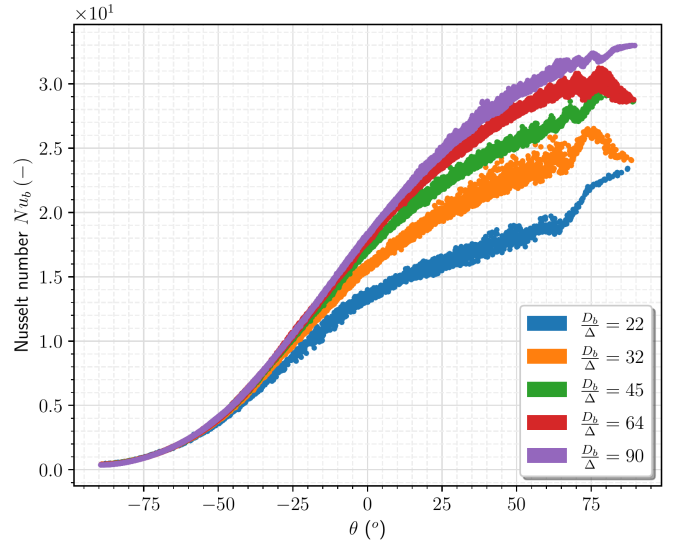


Figure 9: Local Nusselt number at higher Prandtl number $Pr = 5.0$ and $Re_b = 62.5$. Some oscillations are visible in the measurements, especially at the bubble's top.

finest. As a consequence, the location of the reconstructed interface (PLIC plane) has a larger effect on the temperature gradient measure. In our case, the facets' position may also influence the solution. We expect that the error is dependent on the vapour volume fraction contained in the mixed cell. These oscillations are less and less visible as the spatial resolution increases.

Based on these validated numerical results, we present our strategy to model the thermal boundary layer in the following section.

3 Boundary-layer modelling strategy

3.1 Introduction to existing boundary layer enhancement techniques

The chemical transport community has been developing various approaches to enhance both passive and reactive scalar gradient prediction in a single rising bubble vicinity. Some of them have been briefly introduced in **Sec. 1**. In each case, it should be noticed that the variable of interest is the concentration c . In the rest of the paper, we focus on passive scalars. For applications of these approaches with chemical reactions, mass transfer and change in volume please refer to [34, 46]. In fact, as long as phase change is not taken into account, a parallel can be made between concentration and dimensionless temperature through the diffusivity coefficient α_l . The advection-diffusion equation does not contain any additional source term.

On the other hand, the community of wall-bounded turbulence has developed several methodologies to capture strong varying quantities in the walls' vicinity. Some of the strategies are analytical and empirical. However, few of them are based on numerical sub-resolution (LES-RANS solvers) in the turbulent boundary layer and inspired us to develop a second type of approach for DNS-layer coupling.

We are considering a single rising bubble at a steady state. Both the dynamic and thermal boundary layers are settled. Based on these hypotheses, three literature methodologies present reasonable applicability. We can classify the approaches into two categories:

1. Gradient correction using an analytical profile:
 - (a) **Quasi-static correction (QSC)**¹ also referred to as sub-grid model in [30] and re-employed in [26, 29, 31]: A fit is done at each time step. The analytical profile is permeable to the numerical resolution underneath.
 - (b) Unsteady boundary layer energy tracking (UBLET)¹ [27, 32, 33]. It consists of tracking the temporal evolution of the energy contained in the boundary layer: A given profile is introduced into a simplified advection-diffusion equation. The governing equation is integrated radially over a finite fixed thickness in the interface vicinity. The energy contained within the layer is resolved over time and is therefore unsteady/transient. Energy is transferred to the neighbouring cells solely through convection, via a source term for the macroscopic field resolved by the CFD.
2. **Laminar radial sub-resolution (LRS)**¹: For each interface facet, a probe with a certain length is set and a temperature equation is resolved over the 1D probe. The boundary condition at the probe's tip is deduced from the interpolation of the temperature field or its derivative. Tangential effects may be incorporated as source terms.

Analytical profile approaches.

In each analytical approach 1a (QSC) and 1b (UBLET), several radial problems are considered locally all over the interface portions². Radial profiles are imposed by the choice of a form of the analytical solution. Some local information on the surrounding flow field such as local derivatives $\tau = \frac{\partial u}{\partial x} = -\frac{\partial v}{\partial y}$ is used in the time-dependant approach 1b.

The first class of methods 1a uses one temperature value to calibrate a free parameter δ appearing in a simple analytical form of solution. At each time step, this parameter is adjusted based on the mixed cell temperature value, which can be regarded either as the local value or the integral value, as guided by insights from previous studies (specifically, Weiner *et al.* [26]), treating it as an extensive quantity in a Finite Volume approach. Bothe *et al.* [30] originally introduced a self-similar form of solution to describe the scalar boundary layer appearing at an inviscid interface (No-shear, see **Fig. 10**). Later on, Bothe *et al.* [29], Cai *et al.* [31] or Weiner and Claassen [26, 33] re-employed this form of solution to investigate thin concentration layers developing around bubbles. The general form of

solution, in terms of a dimensionless temperature Θ , and the associated hypotheses are reminded by **Eq. (23)** and **Eq. (24)** respectively.

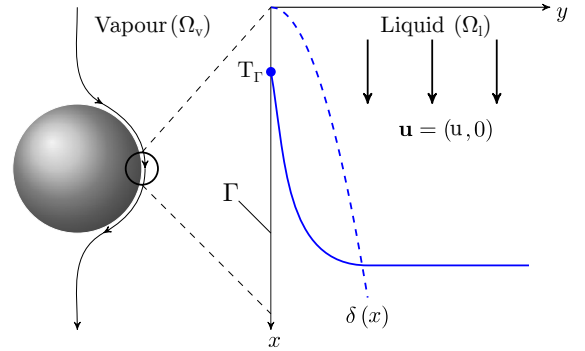


Figure 10: Figure extracted from [46] and adapted to the paper's nomenclature.

$$U \frac{\partial \Theta}{\partial x} = \alpha_l \frac{\partial^2 \Theta}{\partial y^2} \quad (23a)$$

$$\Theta(x, y) = 1 - \operatorname{erf}\left(\frac{y}{\delta(x)}\right) = \operatorname{erfc}\left(\frac{y}{\delta(x)}\right) \quad (23b)$$

$$\delta(x) = 2 \sqrt{\frac{\alpha_l x}{U}} \quad (23c)$$

$$\kappa = 0 \quad (\text{Plane interface}) \quad (24a)$$

$$U = \text{const} \quad (\text{Inviscid interface}) \quad (24b)$$

$$V = 0 \quad (\text{Planar flow}) \quad (24c)$$

Here, x is the curvilinear abscissa, the position from the bubble's top.

This analytical profile (23b) has been extensively used at high Prandtl numbers from 1×10^1 to 1×10^7 in [29] and [26] (Peclet numbers from 1×10^2 to 2×10^4).

On the contrary, Aboulhasanzadeh *et al.* [27] (1b) have decided to use a parabola to describe the concentration profile on a finite controlled thickness δ_0 while exhibiting certain properties:

$$\Theta \equiv \bar{c} = \frac{c}{c_0} = 1 - 2 \left(\frac{y}{\delta}\right) + \left(\frac{y}{\delta}\right)^2 \quad (25)$$

Through **Eq. (25)**, Aboulhasanzadeh *et al.* consider that the concentration profile and its derivative cancel at a certain distance δ . At the interface, the concentration is assumed to be constant and equals c_0 .

The scalar derivative at the interface can be simply evaluated using **Eq. (26)**.

$$\left. \frac{\partial \Theta}{\partial y} \right|_{y=0} \equiv \left. \frac{\partial \bar{c}}{\partial y} \right|_{y=0} = -\frac{2}{\delta} \quad (26)$$

Instead of fitting directly the free parameter δ using a concentration value, Aboulhasanzadeh *et al.* have integrated the pro-

¹Acronym chosen by the authors

²The original papers [26, 27, 29–32] consider the local concentration c and dimensionless concentration \bar{c} , but we transposed it to the thermal problem for the presentation here.

file in the radial direction and over a fixed and arbitrary finite-thickness $\delta_0(\theta, \phi)$. Only normal linear velocity variations have been considered (with a slope $\tau = \partial_x u = -\partial_y v$: the surface divergence of the velocity).

The mass \bar{M} or energy \bar{E} contained in the layer is then expressed as follows:

$$\bar{E} = \int_0^{\delta_0} \Theta dy \quad \left(\equiv \bar{M} = \int_0^{\delta_0} \bar{c} dy \right) \quad (27)$$

Finally, replacing the previous integral **Eq. (27)** in the overall layer integrated equation yields:

$$\frac{D\bar{E}}{Dt} = -\tau\bar{E} + \tau\delta_0 \Theta|_{\delta_0} - D_m \left(\frac{\partial\Theta}{\partial y} \Big|_{\Gamma} - \frac{\partial\Theta}{\partial y} \Big|_{\delta_0} \right) \quad (28)$$

The parameters describing the profile can be deduced by the instantaneous level of energy contained in the layer \bar{E} . The resolution of **Eq. (28)** replaces locally the Eulerian temperature field. Temperature and thermal fluxes are not coupled within this resolution. **Eq. (28)** is then discretised taking advantage of the surface mesh and solved over the interface.

It should be noticed that the analytical profiles of methods 1a and 1b are only described by one free parameter δ . As a consequence, they can be fitted with a single value, e.g. a local temperature value or the mass or energy value contained in the mixed cell or layer. Both the time-dependency and the Eulerian-grid coupling cannot be achieved conjointly through these existing methods. The thickness $\delta^{(n)}$ at instant (n) is obtained through the energy value $\bar{E}^{(n)}$ in **Eq. (27)** and **Eq. (28)**. However, there is no reason that $\Theta|_{\delta_0^{(n)}}$, evaluated from the profile at the end of the layer (at distance δ_0), matches the Eulerian field.

Finally, in the method 1a, the fluxes on the Eulerian control volumes are evaluated through the analytical profile. It supposes that the analytical profile substitutes the numerical temperature resolution locally. Weiner *et al.* [26] performed complex integration over the cells' wetted surface area and it proved more accurate than correcting the cell face centre value. In 1b, a source term is used to transfer the fluxes of excess energy to the Eulerian grid but there is no further precision concerning the treatment of the region impacted by this coupling. The assessment of flux correction and its benefits over time will be addressed in future work.

Laminar radial sub-resolution (LRS).

The second approach 2 has been inspired by the thesis work of Bizid [47]. It aimed to enhance the velocity prediction near a solid curved shape (turbine blades...). His method is related to the thin boundary layer equation also referred to as turbulent boundary layer equations (TBLE) [48–50] in which the Reynolds Averaged Navier Stokes momentum equations are solved unidirectionally near a solid boundary while interpolating the pressure term to avoid further computational resource requirements. Such methods fail when adverse pressure gradients are dominating.

In the thesis of Chatelain [51], some work has been undertaken to solve for the temperature boundary layer in a channel. He employed the uni-directional solving procedure for a thermal planar problem. A turbulent diffusivity α_T is added to the temperature equation to account for sub-grid fluctuations. The latter thermal method has been applied to very simple geometries. A combination of [47] (non-planar shapes) and [51] (thermal considerations) has inspired the present work.

Credit is also due to Gruending *et al.* [52] who solved non-linear ordinary differential equations (ODEs) locally and in the normal direction to the interface in the context of reactive scalars.

Their numerical approach focuses on chemical reactions and is not fed by the interpolated velocity field. Consequently, it incorporates a theoretical form of solution that acts as a tangential convective source term.

To the best of our knowledge, there is currently no comprehensive method that encompasses all of the aforementioned approaches and is applied to a thermal problem involving bubbles or droplets.

Velocity correction could also be combined with the thermal approach proposed here.

3.2 Discussion and improvement of existing strategies

The QSC approach among two of the listed approaches is relevant to us in the first attempt because it does not necessitate further major developments and is partially achievable in a post-processing tool. Moreover, we propose a novel approach similar to thin/turbulent boundary layer equations where several 1D problems are solved in each facet's normal direction over a finite length.

Both retained approaches (1a and 2) rely on using the close but resolved temperature field. In other words, it is necessary to exploit the field at a distance that should be close to the interface to contain enough information without being too erroneous.

In the case of 1a, it is required to work with a dimensionless temperature profile Θ because analytical profiles are often derived using self-similar hypothesis (dimensionless equations) and two Dirichlet boundary conditions bounding the range of temperature values. Therefore, we should dispose of more than one free parameter. Indeed, an additional parameter (T_∞^θ or T_δ^θ depending on the position where it is defined) is needed to non-dimensionalise the problem locally. One of the biggest difficulties with the time-dependant approach is that the far-field temperature used to non-dimensionalise the problem will evolve over space and time in a multiple bubbles configuration. No research has been conducted to consider this effect to the best of the authors' knowledge. Therefore, the application is not straightforward.

Besides, to apply methods 1a and 1b, another free parameter has to be used to fit the radial profile instantaneously; it can be determined either from a local quantity (concentration or temperature) or an extensive one (energy or mass). If an instantaneous quantity is used, the coupling is done with the local temperature field but the energy is not necessarily conserved over time ($\partial_t \Theta$ is considered to be zero at each fitting step but

changes over time for the CFD solver). On the contrary, if the energy within the boundary layer is conserved over time, the resulting temperature field may be inconsistent with the instantaneous Eulerian field lying underneath (temperature or fluxes). That is why the latter method 1b annihilates the underlying Eulerian solution. Finally, the last method 2 is coupled to the CFD resolved field by interpolating a single temperature value.

The dimensionless temperature profile that has been developed in **Appendix A** exhibits two parameters (δ_1 and δ_2) which are linked by the mean curvature $\kappa = \kappa_1 + \kappa_2$, normal velocity u_r and thermal diffusivity α_l . As a consequence, we can not satisfy both a local instantaneous temperature or energy value and the time evolution of the energy in the layer.

In the case of 2, the temperature does not require necessarily a non-dimensionalisation. Further modelling at the local scale is not considered and the fluctuations are assumed to be resolved. The benefits of the method rely on the fact that the local coordinate system is perfectly aligned with the principal direction of variations. Hence, the discretisation is consistent everywhere and is no longer influenced by the relative collinearity of the facets' normal vectors to the Cartesian directions.

Sec. 3.3 and **Sec. 3.4** present the methodology to apply the **QSC** and **LRS** approaches to the resolution of the temperature in boundary layers, respectively.

3.3 Quasi static analytical profiles applied to temperature

3.3.1 Overall approach

The analytical expression of the temperature used in the literature comes from a planar problem. As underlined previously a more complex form of solution could be looked for in a local spherical frame of reference attached to the interface (see **Fig. 11**).

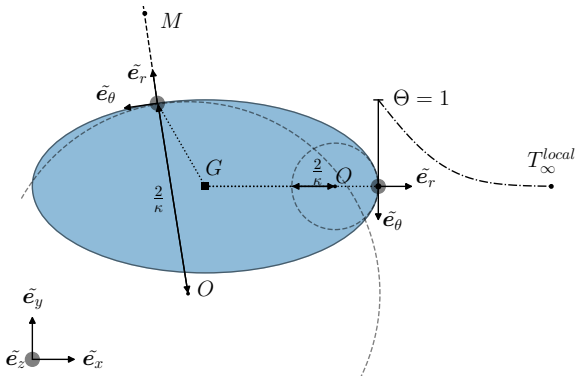


Figure 11: Schematic and notations employed in the derivation of the analytical approach. The osculating radius is related to the local mean curvature $R = 2/\kappa$. The principal curvatures are assumed to be identical.

In this osculating frame of reference, the advection-diffusion equation is directly related to the curvature which has to be considered.

There, diffusion has a significant impact, and the term $\frac{2}{r} \frac{\partial \Theta}{\partial r}$, when approximated as $\kappa \frac{\partial \Theta}{\partial r}$, remains non-negligible. Accounting for the mean curvature allows a better mathematical representation of the interface locally (a first-order surface as op-

posed to a zeroth-order surface in the context of a planar problem). **Appendix B** demonstrates that employing the mean curvature provides a good approximation for the diffusion term arising due to basis variations when considering two similar radii of curvature values (R_1 and R_2).

In the particular case where the velocities are considered constant in space at a given time and by taking the first order approximation of $1/r$, the steady convection-diffusion equation writes:

$$\left(\frac{u_r}{\alpha_l} - \kappa \right) \frac{\partial \Theta}{\partial r} + \frac{\kappa u_\theta}{2\alpha_l} \frac{\partial \Theta}{\partial \theta} = \frac{\partial^2 \Theta}{\partial r^2} \quad (29)$$

One can note that azimuthal variations have been neglected. The choice of using a spherical frame of reference is justified and tangential variations are expected to remain much stronger in the direction of relative velocity between the two phases even in more complex configurations. Besides, it enables the re-employ of the original sub-grid diffusion model while complexifying it. The spherical coordinate system embeds a singularity on the symmetry axis *i.e.* azimuthal temperature variation $\partial_\phi \Theta$ should be zero although u_ϕ could be non-zero.

By aligning the osculating sphere equator's normal direction with the facet's normal vector, the equations correspond to the curvilinear coordinates with two identical and constant principal curvatures.

An analytical solution exhibiting a double exponential combination has been found using a separation of variable method (see the development in **Appendix A.1**). A strong assumption is made concerning the tangential variations. Because of the separation of variables method, the latter can not be a function of the radial distance to the interface. As a consequence, the considered velocity profile considered does not verify the divergence-free condition. The overall temperature profile is given by **Eq. (A.25)** reported here:

$$\Theta = \left(1 - e^{\delta^*} \right)^{-1} \times \left(e^{\delta^*} - e^{\delta^*} e^{-\frac{r}{\delta_1}} \right) \quad (30a)$$

$$\delta^* = \frac{\alpha_l \delta_1}{2\alpha_l + \delta_1 (u_r - \kappa \alpha_l)} \quad (30b)$$

$\Theta = (T_\delta^\theta - T) / T_\delta^\theta$ is cancelling at $r = \delta$. At this distance, $T = T_\delta$. In other words, by picking a temperature at a distance $r = \delta$ to non-dimensionalise the problem, the fitting procedure consists in fitting δ_1 knowing the normal velocity u_r and the curvature κ .

Although the chosen velocity field is not divergence-free, the effect of the liquid flow impacting the bubble front is embedded in an average normal velocity $u_r \leftarrow \overline{u_r}$ (**Eq. (31)** calculated using Simpsons' method over the probe). It differs for each value of θ considered. Deriving an exact solution while taking every aspect into account could not be achieved in the authors' knowledge. The potential effect of phase change proportional to \dot{m}_v could also be embedded. It should be emphasised that the goal is to look for a form of solution that could adapt and capture the non-linearity in the near interface profile compared

to classical linear schemes. The solution must degenerate to the fine mesh solution.

$$\bar{u}_r = \frac{1}{\delta} \int_{r=R}^{r=R+\delta} u_r(r) dr \quad (31)$$

Alternatively, as u_r and κ are difficult to define and evaluate, a second parameter δ_2 (see **Eq. (32)**) can also be fitted along with δ_1 to be used in **Eq. (30a)** in order to assess u_r and κ indirectly.

$$\delta_2 = \frac{\alpha_l \delta_1}{\alpha_l + \delta_1 (u_r - \kappa \alpha_l)} \quad (32)$$

If so, the fit is based only on the temperature field but the number of points to achieve the fitting step is higher (fitting interval wider). It is interesting to investigate this aspect because it may save computational resources (reducing interpolations and projections).

3.3.2 Fitting procedure

Two forms of solutions are used in the current section: the **Erfc** function, extensively used in the literature, as well as the authors' derived solution referred to as the **SoV** approach. Two fittings techniques have been explored: a fitting technique based on locally evaluated values and a second one, based on integral values of the profile on a finite thickness still in the interface surrounding area. The choice of point locations (local values and integral bounds) and point spacing, in the case where multiple unknowns should be found, are presented in **Tab. 4**.

Local fitting procedure.

First, the solutions are fitted according to the temperature field using Newton's method on the finest meshes. In the case of the Erfc solution, the function f to minimise is monotonous according to its set of free parameters Φ . Some known values of parameters ξ for whom f is null are mandatory to solve for Φ . f is expressed for each angle θ as follows:

$$\mathbf{Erfc}: \quad \xi = \{r, T\}; \quad \xi' = \{r\}; \quad (33a)$$

$$\Phi = \{T_\infty^\theta, \delta\}$$

$$\Theta \leftarrow \mathbf{Eq. (23b)}$$

$$f(\xi, \Phi) = T_\infty^\theta [1 - \Theta(\xi', \Phi)] - T \quad (33b)$$

$$\mathbf{SoV}: \quad \xi = \{r, \delta, T, T_\delta^\theta\}; \quad \xi' = \{r, \delta\}; \quad (33c)$$

$$\Phi = \{\delta_1\} \quad \text{or} \quad \Phi = \{\delta_1, \delta_2\}$$

$$\Theta \leftarrow \mathbf{Eq. (30a)}$$

$$f(\xi, \Phi) = T_\delta^\theta [1 - \Theta(\xi', \Phi)] - T \quad (33d)$$

The free parameters Φ associated with each form of solution are given in **Eq. (33a)** and **Eq. (33c)**. T corresponds to a local temperature value measured on the Eulerian mesh at steady-state.

The matrix conditioning of the Jacobian matrix (appearing in Newton's algorithm) could cause convergence problems. The problem can arise due to the nature of the analytical solution.

Weiner *et al.* [26] underlined that the erfc derivative according to δ tends to zero for increasing δ values. The problem is further exposed in **Appendix C**.

Integral fitting procedure.

To improve the robustness of the method, efforts were made to utilise unidirectional integral quantities, while the consideration of a 3D integral within the mixed cell, although having the potential to improve accuracy [26], is not currently investigated. The integration region depends on the number of unknowns and the type of approach. This information is summarised in **Tab. 4**. In that case, the function to minimise, denoted F , is expressed as follows:

$$F(\xi, \Phi) = \int_a^b f(\xi, \Phi) dr \quad (34)$$

$$= (T_{\delta, \infty}^\theta - \bar{T})(b - a) - T_{\delta, \infty}^\theta \int_a^b \Theta(\xi', \Phi) dr$$

The integral value \bar{T} is obtained by numerical integration over the probe where the reference DNS solution has been interpolated.

The two methods have been tested on both erfc profile (see **Eq. (23b)**) and the current paper SoV derived solution (see **Eq. (30a)**). The profile proposed by [29, 30] assumes a Dirichlet boundary condition for Θ when $r \rightarrow \infty$. On the contrary, the profile formulated in this paper (**Eq. (30a)**) uses local information to non-dimensionalise the temperature. T_∞^θ is deduced from the simulation setup or fitted in the first case whereas T_δ^θ is measured in the second case.

The fitting ability of these solutions is studied and exposed in **Sec. 4.2**. The derivatives of the candidate functions can be found in **Appendix C.1** and **Appendix C.2**.

3.4 A radial sub-resolution with tangential source terms

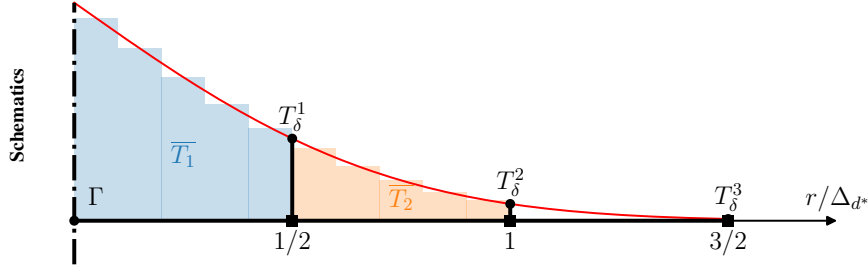
Taking into consideration that the quasi-static analytical profile of the planar problem (QSC) has been formulated under specific assumptions (see **Eq. (24)**) which are difficult to meet in the configurations considered here, the Laminar Radial Sub-resolution (LRS) has been assessed in parallel.

Sec. 4.1 extensively explores the hypotheses in **Eq. (24)** by analysing post-processed quantities within the interfacial region, illustrating their radial variations. In the considered configuration, the velocity variations in the radial direction are expected to be sufficiently significant over the thickness of a mesh cell to consider at least a one-dimensional numerical resolution approach. It is clearly visible in the next sections (see **Sec. 4.1.2**). The current approach for temperature has been explored without using any turbulent thermal diffusivity hence it is referred to as a **Laminar Radial Sub-resolution (LRS)**.

This second approach relies on solving numerically the same laminar advection-diffusion equation considered to derive the analytical solution (see **Eq. (35)**) for $r \in [R; R + 3\Delta_d]$. In that case, the velocity components are interpolated on a one-dimensional simulation domain associated with each facet whereas the tangential term (RHS of **Eq. (35a)** and **Eq. (35b)**)

Table 4: Associated equations, figures and tested cases for the two forms of solutions and their five associated fitting approaches (FIT-A, B, C, D and E). The red profile is obtained by interpolation.

		Erfc		SoV		
General	Equations	Eq. (23b)		Eq. (A.25)		
	Figures	Fig. 19a, Fig. 20a		Fig. 19b, Fig. 20b		
	Cases	FIT-A	FIT-B	FIT-C	FIT-D	FIT-E
	Unknowns Φ	δ	$\{\delta; T_\infty^\theta\}$	δ_1	δ_1	$\{\delta_1; \delta_2\}$
	Specificity	$T_\infty^\theta = T_\infty$		$\kappa \neq 0$ $u_r = 0$	$\kappa \neq 0$ $u_r \neq 0$	u_r, κ, α_l not required
Local	Number of points	1 (T_δ^1)	2 (T_δ^1, T_δ^2)	2 ($T_\delta^1, T_\delta^\theta = T_\delta^2$)	3 ($T_\delta^1, T_\delta^2, T_\delta^\theta = T_\delta^3$)	
	Positions r/Δ_d^*	1/2	{1/2; 1}	{1/2; 1}	{1/2; 1; 3/2}	
Integral	Number of points		0	1 ($T_\delta^\theta = T_\delta^1$)	1 ($T_\delta^\theta = T_\delta^2$)	
	Number of integral values	1 (\bar{T}_1)	2 (\bar{T}_1, \bar{T}_2)	1 (\bar{T}_1)	2 (\bar{T}_1, \bar{T}_2)	
	Integral bounds					
	$[a, b]$ and positions r/Δ_d^*	[0; 1/2]	{[0; 1/2]; [0; 1]}	{[0; 1/2]; 1/2}	{[0; 1/2]; [0; 1]; 3/2}	



can be interpolated from the coarse mesh or modelled using fine simulations. In the current work, only interpolations from coarse or converged DNS results are addressed. This tangential term acts as a source term in the heat equation (see continuous and discretised forms in Eq. (35.a) and Eq. (35.b), respectively). The discretised equation Eq. (35.b) requires obviously two boundary conditions to be resolved. In its dimensionless form, $\Theta = (T_\infty - T)/T_\infty = 1$ at the interface whereas $\Theta = 0$ at the 1D domain's end. Also, instead of imposing the temperature, a zero derivative value has been implemented at the domain's end. Coupling the measured fluxes at the probes' end (Neumann) does not give interesting results and will not be discussed extensively. The Dirichlet boundary condition is preferred.

$$\text{Continuous: } \frac{\partial^2 \Theta}{\partial r^2} + \left(\frac{2}{r} - \frac{u_r(r)}{\alpha_l} \right) \frac{\partial \Theta}{\partial r} \quad (35a)$$

$$= \frac{u_\theta(r)}{\alpha_l r} \frac{\partial \Theta}{\partial \theta}(r) - \frac{1}{r^2} \frac{\partial^2 \Theta}{\partial \theta^2}(r)$$

$$\text{Discrete: } \frac{\Theta_{i+1} - 2\Theta_i + \Theta_{i-1}}{\Delta r^2} \quad (35b)$$

$$+ \left(\frac{2}{r} - \frac{u_{ri}}{\alpha_l} \right) \frac{\Theta_{i+1} - \Theta_{i-1}}{\Delta r}$$

$$= \frac{u_{\theta i}}{\alpha_l r_i} \frac{\partial \Theta}{\partial \theta} \Big|_i - \frac{1}{r_i^2} \frac{\partial^2 \Theta}{\partial \theta^2} \Big|_i$$

Convective and diffusive terms can be identified with the fol-

lowing notations (later reused in Sec. 4.3):

$$C^r = \frac{u_r(r)}{\alpha_l} \frac{\partial \Theta}{\partial r} \quad (36a)$$

$$D^r = \frac{\partial^2 \Theta}{\partial r^2} + \frac{2}{r} \frac{\partial \Theta}{\partial r} \quad (36b)$$

$$C^\theta = \frac{u_\theta(r)}{\alpha_l r} \frac{\partial \Theta}{\partial \theta}(r) \quad (36c)$$

$$D^\theta = \frac{1}{r^2} \frac{\partial^2 \Theta}{\partial \theta^2}(r) \quad (36d)$$

Particular attention should be given to the evaluation of velocity in the mixed cells. A wrong sign could cause the convective term to sweep heat unrealistically. It has been observed that at the exact position of the facets, the normal component of the interpolated interface velocity is not null numerically whereas it should be. The weak transmission condition (balance of stress) at the interface in a one-fluid approach could cause the interface to be offset virtually for the velocity field. This offset could be a result of the viscosity calculation. For the discrete model resolution, the velocity profile is corrected to recover the correct interfacial velocity ($u_r|_\Gamma = 0$). A simple shift of the velocity profile is applied. The tangential velocity u_θ is not affected by the correction and is assumed to be sufficiently resolved (low interfacial shear stress because $\mu_v/\mu_l \leq 1$).

The two methods presented in this section are assessed based on their interfacial temperature gradient prediction in the following section. Their strengths and weaknesses are discussed and the best candidate approach is examined to perform multi-

bubble configuration in future scenarios, especially under low spatial resolution conditions. This examination considers both the physical aspects and the numerical implementation.

4 Evaluation of the boundary-layer modelling strategies

Sub-section 4.1 begins with the hierarchy of terms, aiming to determine the leading terms of the thermal advection-diffusion equation.

Sub-section 4.2 shows that in our operational conditions, *i.e.* coarse grids and large thermal boundary layers, the applicability of the analytical profile to replace locally the coarse-grid resolution is limited.

Then, sub-section 4.3 presents the promising results obtained through the laminar radial sub-resolution in terms of local and global heat flux prediction.

4.1 Convection and diffusion terms measurements on reference simulations

To derive the simplified problems presented in **Sec. 3.3** and **Sec. 3.4**, it has been necessary to make several assumptions. Identifying the dominating terms in the temperature equation **Eq. (35a)** is then the first step to legitimate our approach. Depending on the flow regime, it is expected that some terms will vanish because either the velocity component or the temperature gradient component is strongly decreasing at the interface.

The focus is made on both convection terms and the radial diffusion term in spherical coordinates (*i.e.* in the local osculating sphere coordinate system). Aboulhasanzadeh *et al.* [27] are neglecting the tangential component variation while other research groups such as Weiner *et al.* [26, 29] are neglecting the normal convective term through their choice of the analytical solution. It depends on which frame of reference we are working in. Quasi-static methods see the interface as a non-material object which displaces only in the normal direction whereas Aboulhasanzadeh *et al.* [27] are expressing the problem in a material frame of reference *i.e.* convected tangentially. Both researchers are unanimous on the predominance of the radial diffusion term over the tangential one.

Hypotheses such as the omission of the curvature effect and velocity variations, as made in **Eq. (24)** to derive the simplified planar solution, are tested in the subsequent section.

Terms are evaluated for each facet at a distance Δ_{d^*} ($= \frac{3}{2} \sqrt{\Delta_x^2 + \Delta_y^2 + \Delta_z^2}$) from the interface which corresponds to 1.5 times the diagonal of a cell. Such a minimum is necessary to avoid totally using mixed cell values when performing a Tri-linear interpolation scheme. Results are presented in **Sec. 4.1.1**.

Terms that have been computed radially on several probes are later exposed in **Sec. 4.1.2**. The local convergence of quantities over the probe length can be directly observed.

4.1.1 Hierarchy of terms at several regimes

Terms hierarchy over the three identified regions.

The thermal boundary layer thickness δ_0 around the bubble does not follow any known analytical laws or correlations. It has also multiple definitions which are no longer straightforward when we deal with more than one rising object in a finite domain. In particular configurations (self-similarity, pure slip condition) such as on flat planes or walls, analytical expressions or forms of solution can be found [53]. The particular geometry of the bubble favours stall and recirculation which have a direct impact on the boundary layer thickness and thus heat transfers. In the case of the spherical bubble, we can divide the heat transfer profile depending on the bubble's elevation parameter θ in three distinct regions which are observable in **Fig. 12** and **Fig. 13**: the bottom region denoted (1) and the equator and top regions denoted (2) and (3), respectively. The division of the interface into three regions serves solely to emphasize the hierarchy of terms and to assess whether the simplified equation remains valid within these regions. The methods are applied independently of the region.

At the bubble's top (3), the liquid is decelerating and the tangential velocity component is increasing to ensure mass conservation until the bubble's zero elevation (coordinate $\theta = 0^\circ$). As a consequence, heat is increasingly swept along the tangential direction. As in every forced convection flow, there is a competition between diffusion and advection. In a condensation case, the normal convective component is positive which signifies that convection is acting against diffusion (see **Eq. (37)**). The same reasoning, but with the opposite sign, applies to evaporation.

$$\text{Top (3):} \quad \underbrace{\left(u_r - \frac{2\alpha_l}{r}\right)}_{<0} \underbrace{\frac{\partial\Theta}{\partial r}}_{<0} \approx \alpha_l \underbrace{\frac{\partial^2\Theta}{\partial r^2}}_{>0} \quad (37)$$

The boundary layer is compressed so the normal temperature gradient varies rapidly. It then decreases along the curvilinear abscissa (when θ decreases). In the equator's region (2), the tangential convective term reaches a maximum and ultimately prevails over the normal one (see **Eq. (38)**).

$$\text{Equator (2):} \quad \underbrace{\frac{u_\theta}{r}}_{>0} \underbrace{\frac{\partial\Theta}{\partial\theta}}_{>0} \approx \alpha_l \underbrace{\left(\frac{2}{r} \frac{\partial\Theta}{\partial r} + \frac{\partial^2\Theta}{\partial r^2}\right)}_{>0} \quad (38)$$

Finally, at the bottom, the normal convective term is changing sign and acts in the same direction as diffusion if u_r exceeds $2\alpha_l/r$ (see **Eq. (39)**). The boundary layer is then expanding and normal heat transfer is decreasing. Mathematically, in the absence of the tangential term and at a steady state, the value on the symmetry axis is the saturation temperature. In a turbulent configuration, the recirculation will create fluctuating contributions. Both tangential convective and diffusive terms exist in this region and are essential although their magnitude is low. Their contributions are at the origin of a non-constant temperature field at steady-state ($\partial_t\Theta = 0$) in the bubble wake.

$$\begin{aligned}
\text{Bottom (1):} \quad & \underbrace{\left(u_r - \frac{2\alpha_l}{r} \right)}_{\substack{>0 \\ \sim u_r \\ >0 \text{ if } u_r > \frac{2\alpha_l}{r}}} \underbrace{\frac{\partial \Theta}{\partial r}}_{<0} \\
& \approx \underbrace{\alpha_l \frac{\partial^2 \Theta}{\partial r^2}}_{>0} + \underbrace{\left(\frac{\alpha_l}{r^2} \frac{\partial^2 \Theta}{\partial \theta^2} - \frac{u_\theta}{r} \frac{\partial \Theta}{\partial \theta} \right)}_{\text{small but } \neq 0}
\end{aligned} \tag{39}$$

Using the Erfc profile presented in **Eq. (23b)** assumes that the tangential convective term is dominating *i.e.* that the central region is the largest over the whole θ range. It is no longer the case in the stagnation points' regions whose width is inversely proportional to the Prandtl number Pr_l .

General observations.

The convective terms have been post-processed on the reference mesh for both Reynolds numbers and are shown in **Fig. 12a** and **Fig. 12b** for $Pr_l = 1.0$.

The advective term of the simplified temperature equation **Eq. (35a)** in spherical coordinates is superimposed with the total convective term (Cartesian) computed from the simulation. As a consequence, it is a first validation to ensure that the current problem is governed by **Eq. (35a)** and that the reconstructed azimuthal variations are zero.

The normal convective term is globally prevailing at both Reynolds numbers. However, three zones are observed.

At the bubble's front $\theta \gg 0^\circ$, the radial convective term is dominating whereas the tangential convective term decreases from the equator until it cancels at the stagnation point.

In the bubble's equator region ($|\theta| \leq 20^\circ$ in **Fig. 12a**, **Fig. 12b**), the tangential term tends to dominate over the radial convective term. It is especially visible at the higher Reynolds numbers. At $\theta \approx 10^\circ$, the maximum tangential velocity u_θ is reached while a zero normal velocity u_r is measured. However, at this location, the tangential convective term is not at its maximum value. Something important to notice is that the maximum of the tangential term is not reached exactly at $\theta = 0^\circ$ but rather at $\theta = -10^\circ$. Behind the bubble, the boundary layer expands so the temperature field tends to stretch in the tangential direction. The tangential convective term thus increases faster than the tangential velocity decreases. We expect that the symmetry in the tangential term distribution around $\theta = 0^\circ$ will be influenced by the level of turbulence which conditions the position of the separation point.

At the bubble's rear ($\theta \ll 0^\circ$), the tangential convective term is decreasing. We expect this region to have a strong dependency on the flow regimes. At higher Reynolds numbers, we expect a stall to occur due to an adverse pressure gradient. In that case, recirculations may be observed which will influence this region of low heat transfer.

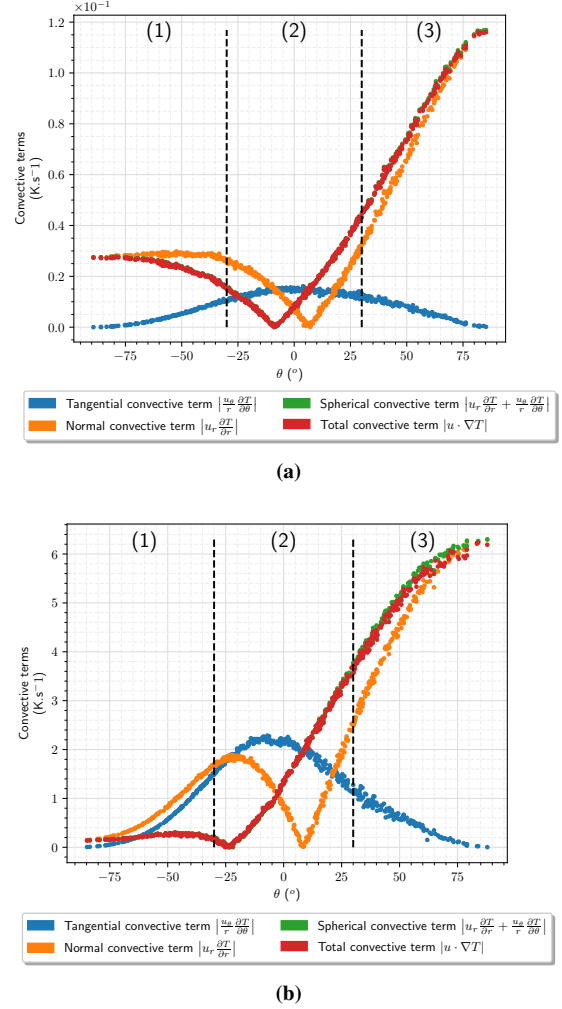


Figure 12: Convective term hierarchy in the interface vicinity:

- (a) $Re_b \approx 3.6$, $Pr_l = 1.0$, $\frac{D_b}{\Delta} = 48$,
- (b) $Re_b \approx 62.5$, $Pr_l = 1.0$, $\frac{D_b}{\Delta} = 45$

Regarding diffusion, its normal component is dominant (see **Fig. 13a**, **Fig. 13b**). The tangential diffusive term is comparatively more significant at the lowest Reynolds number. It is not negligible especially at the bubble's top and bottom according to **Fig. 13a** for this low Re_b value. We were expecting this term to be low as the configuration related to **Fig. 13a** is closer to a pure radial diffusion problem. The error may come from a stronger effect of the finite domain size which is not large enough and the outflow boundary conditions are influencing more significantly the results. As the domain cross-section is a square, the azimuthal symmetrical aspect of the flow is lost. It explains the discrepancies in the values for a given angle θ at a low Reynolds number. The fact that this assessment of tangential diffusion does not go to zero at the symmetry axis was expected as the singularity of the solution is difficult to capture in a 3D discrete solution where the discrete surface does not show any symmetry.

We can observe that the variations of the normal diffusion are dominant at high Reynolds numbers (see **Fig. 13b**). The tangential diffusive term remains negligible for all θ values com-

pared to the normal diffusion term which is sufficient to neglect it in a first modelling procedure. **Sec. 4.3** shows that this term has importance in regions that are already resolved and it avoids the sub-resolution approach to deteriorate the original solution.

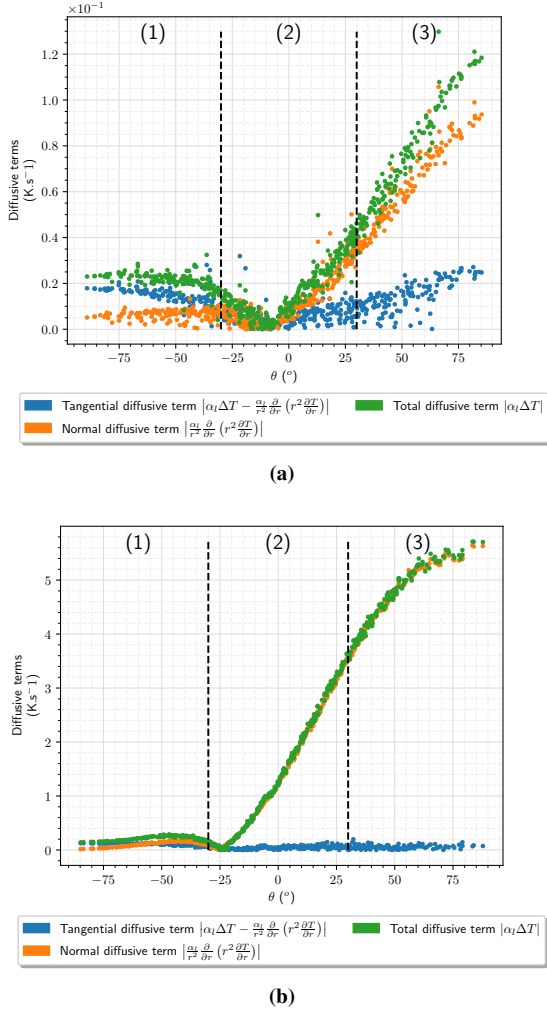


Figure 13: Diffusive term hierarchy in the interface vicinity: **(a)** $Re_b \approx 3.6$, mesh resolution of 48 elements per bubble diameter. **(b)** $Re_b \approx 62.5$, mesh resolution of 45 elements per bubble diameter.

4.1.2 Radial evolution of the terms

Quantities have been post-processed on radial probes all over the bubble surface. In our approach, we propose to model the temperature only. The velocity is considered to be well captured in the working conditions *i.e.* at viscosity ratios close to unity $\mu_b/\mu_i \lesssim 1$, or for $Pr_l \geq 1$ (Thick velocity boundary layer). **Fig. 14a** and **Fig. 14b** show that the velocity high order variations are captured close to the interface. The interpolated profiles are sufficiently resolved to be used in a sub-resolution process. The legend for the next figures is shown at the end of the current section (see **Fig. 18**). The following figures present the useful quantities at $Re_b \approx 62.5$ and $Pr_l = 1$.

The normal velocity component evaluated at each facet is non-zero in **Fig. 14a**. It causes the normal convective term to show the wrong sign if assessed directly, which raises problems

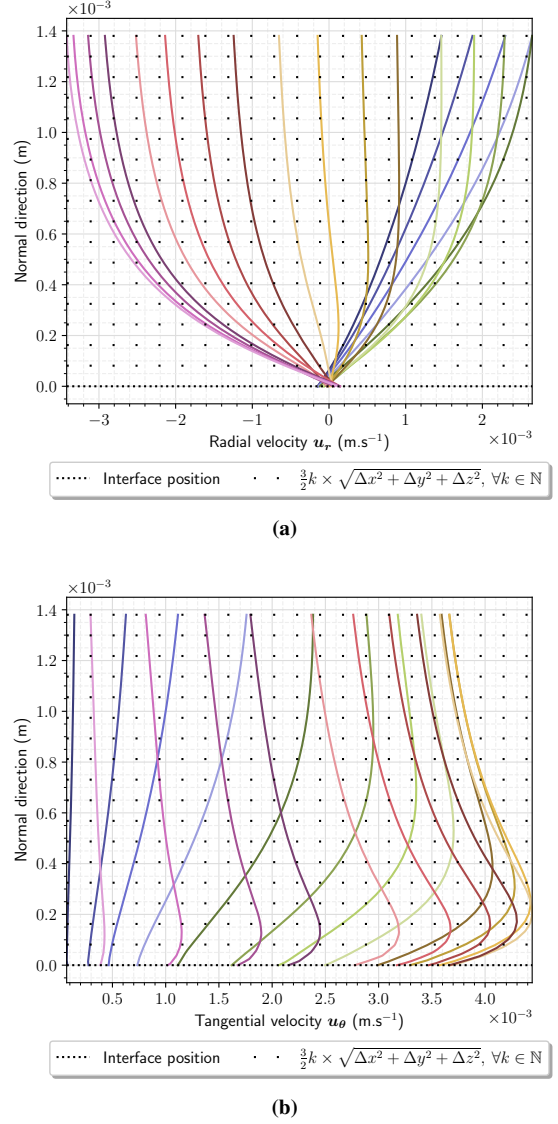


Figure 14: Radial and tangential velocity profiles at $Re_b \approx 62.5$ and $Pr_l = 1$ and for a mesh resolution of 64 elements per bubble diameter (fine mesh): **(a)** Radial velocity u_r (m s^{-1}), **(b)** Tangential velocity u_θ (m s^{-1}). The velocity along \hat{e}_ϕ is zero.

in the radial sub-resolution approach. These profiles are all offset to cross exactly $u_r|_\Gamma = 0$ in the subsequent convective terms assessment.

Fig. 14a shows that the velocity is not constant in the interface vicinity. As a consequence, we expect the analytical solution to mispredict the temperature field if the velocity is evaluated locally when looking for the free parameter (root-finding routines). As presented in **Sec. 3.3.1**, the free parameters are fitted based on the temperature field. An averaged velocity characterising the incoming fluid $u_r \leftarrow \bar{u}_r$ (see **Eq. (31)**) is also used in method **FIT-D** (see **Tab. 4**).

Strong variations of temperature can be observed in **Fig. 15**. For all the cases treated in this paper, the interfacial flux is strictly decreasing from the bubble's top to bottom. **Fig. 16a** shows that the far-field value of temperature is rapidly converg-

ing (end of range $[0; \Delta_d^*]$) whereas the error is very significant between the two mesh resolutions of 16 and 64 cells per diameter in the near interface region.

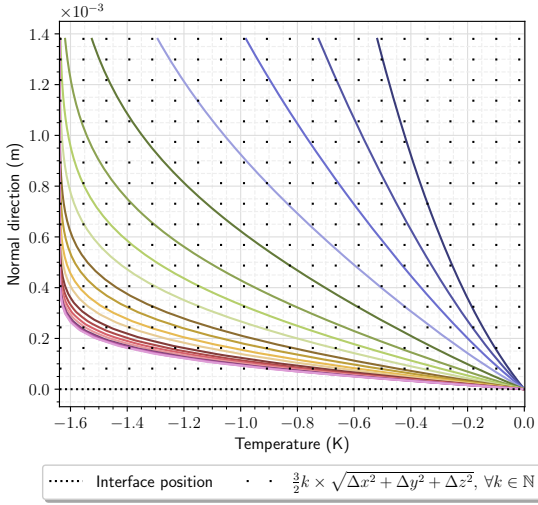
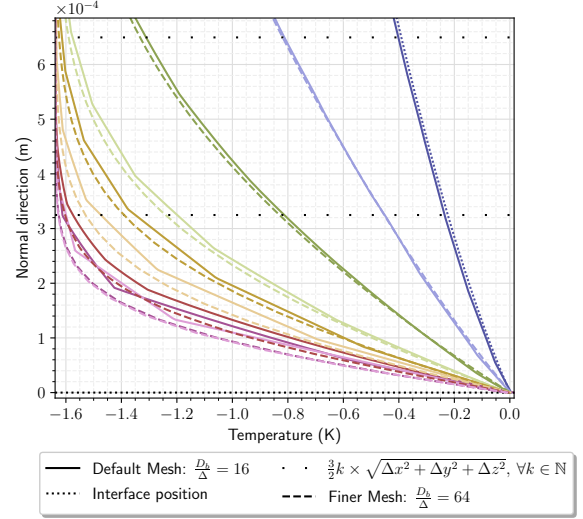


Figure 15: Temperature distribution at the interface and at several elevations θ at $Re_b \approx 62.5$ and $Pr_l = 1$ and for a mesh resolution of 64 elements per bubble diameter. The temperature varies drastically in the interface vicinity.

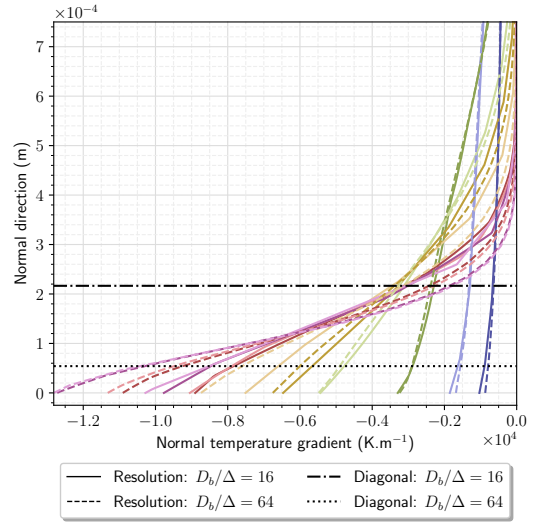
The normal temperature gradient varies very rapidly close to the interface (see **Fig. 16b**). As a consequence, a poor mesh will be unable to capture such strong variations. A simple first-order (forward finite difference) scheme to measure the interfacial flux, which is very often used in numerical approaches, fails to predict it. Such systematic errors have a strong effect on the global Nusselt number prediction. For example, the global Nusselt number values exposed in [29] at high Pr present relative errors within a 50% range around the converged value. In our case, up to 30% underestimation is observed on the bubble's top with respect to the coarse mesh.

The radial variations are dominant. It was highlighted in the **Sec. 4.1.1** through the post-processing of the convective terms. One can conclude that the tangential variation should be easily captured by coarser meshes. Surprisingly, the tangential temperature variations interpolated over the probes are somehow noisy for coarser meshes as presented in **Fig. 17a**. It is mainly attributed to both interpolation and differentiation errors in post-processing as well as the local application of the temperature extension in the numerical method (DNS solver). Several local problems are imposing weakly the saturation temperature at the interface ($T_\Gamma = 0$). The same applies to its tangential derivatives.

As the Peclet number increases, the tangential convective term should gain importance in comparison with the normal convective term at the bubble $\theta = 0^\circ$ elevation coordinate. It legitimates our will to consider every convective term in the laminar sub-resolution equation. The use of the classical numerical method based on Ghost-fluid and a local diffusion problem (presented in **Sec. 2.1.3**) is no longer appropriate for low mesh resolutions at high Reynolds numbers.



(a)



(b)

Figure 16: Temperature (a) and Normal temperature gradient $\frac{\partial T}{\partial r}$ ($K m^{-1}$) (b) at $Re_b \approx 62.5$ and $Pr_l = 1$ and for two mesh resolutions of 16 (coarse) and 64 (fine) elements per bubble diameter.

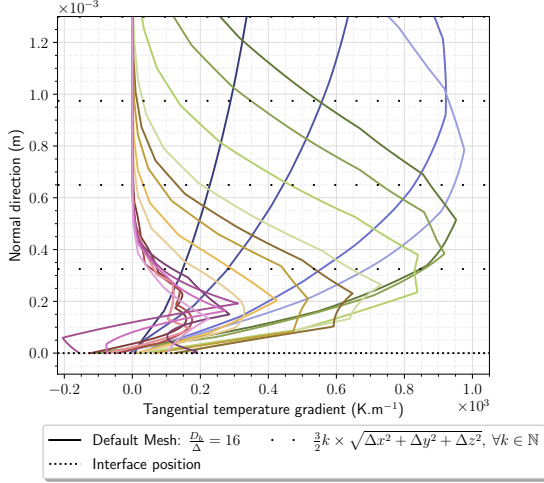
4.2 Analytical profiles: fitting assessment in two steps (fine, coarse) of the quasi-static approach (QSC)

4.2.1 Best fit on the finest mesh solutions

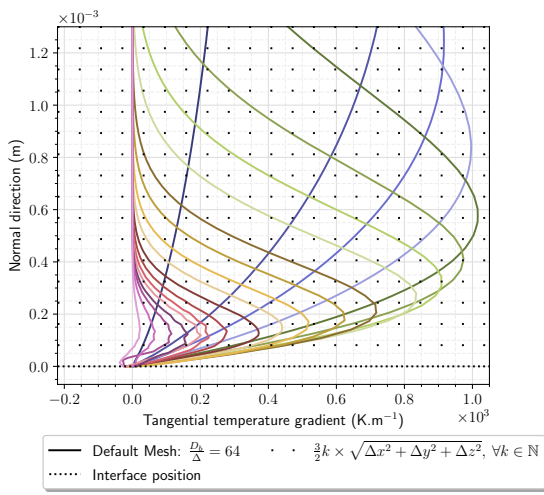
To evaluate the ability of the previously introduced profiles to capture the temperature variations properly (**Sec. 3**), the fields coming from the fine simulations are used first in the fitting process.

Two calibrations performed with the various methods discussed in **Sec. 3.3.2** are shown in **Fig. 19a** and **Fig. 19b** for the Erfc and the SoV profiles, respectively.

All methods are using fine mesh information. The fitted profiles' capabilities are characterised in the following section by the value of the interfacial temperature gradient as a figure of merit. Indeed, it is one of the most important pieces of information that will be used in the application of the model.



(a)



(b)

Figure 17: Tangential temperature gradient $\frac{\partial T}{\partial \theta}$ (K) at $Re_b \approx 62.5$ and $Pr_l = 1$ and for two mesh resolutions of 16 (coarse) (a) and 64 (fine) (b) elements per bubble diameter.

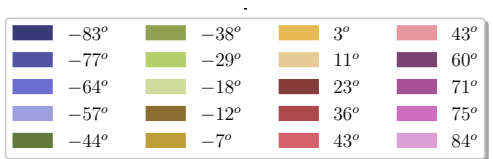
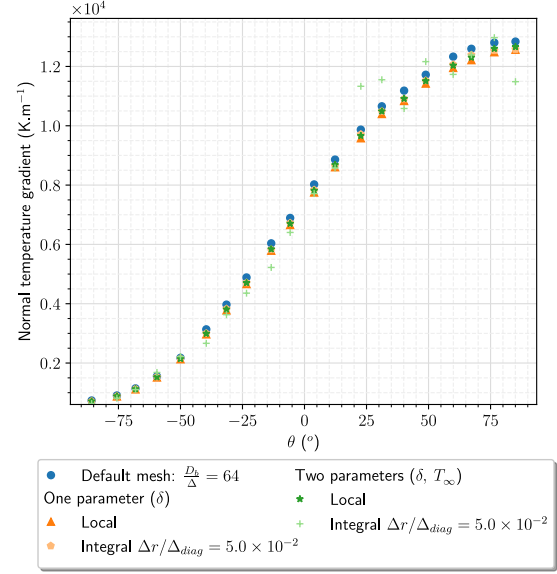
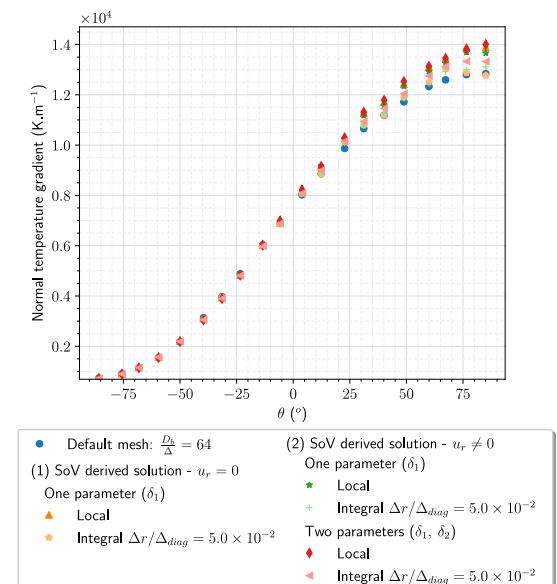


Figure 18: (a) Probe locations for **Fig. 14** to **Fig. 17** at $Re_b = 62.5$, $Pr = 1.0$ and $D_b/\Delta = 16 - 64$.

In **Fig. 19a** (Erfc), the reference profile is globally captured for each tested fitting method both using the local and integral value of temperature. Using one free parameter δ and knowing the infinite temperature value T_∞^θ , it is possible to fit the profile accurately in the interface vicinity. The integral method requires a numerical calculation which should be avoided in an *a posteriori* implementation. However, seeing the near-cell temperature value as an integral could also be considered as emphasised previously in **Sec. 3.1**.



(a)



(b)

Figure 19: Fitted temperature profile in a narrow band around the interface: (a) Erfc function, (b) SoV derived solution. Profiles have been fitted on the finest simulation at $Re_b \approx 62.5$, $Pr = 1.0$ and at a resolution of $D_b/\Delta = 64$

With two temperature values, it was also possible to retrieve the "infinite" temperature T_∞^θ quite accurately in addition to the first parameter δ . It is still working pretty well using local temperature values. In the integral case, two integral values are given to the root finding algorithm but it proves to give more dispersed values as this information is contained infinitely far from the interface. This type of profile does not suit exactly future complex configurations well as it requires an infinite reference.

Analytical solutions in CFD are derived in an idealised situation in semi-finite domains. Defining and measuring a temperature value at infinity is tedious in a closed domain. There are

then two paradigms. On one hand, we can look for analytical solutions describing exactly the physics in the layer (expression of δ and T_∞ known) which is impossible in practice. Determining T_∞^θ by looking for the best fit could be surprising but works well in practice. In the paradigm of this article, we aim to utilise an analytical solution incorporating physical considerations that could replicate the non-linear interfacial temperature variations, as suggested by Bothe *et al.* [29].

Fig. 19b (SoV) shows more dispersed values according to the method employed. Using local temperature values leads to an overestimation of the temperature gradient for both zero and non-zero normal incoming bulk velocity \bar{u}_r . The best prediction is given by the two methods employing integral values of the temperature. In that case, feeding the fitting procedure with an average normal velocity does not have a significant influence on the results. It is mainly because the incoming fluid has already decelerated in the fine mesh tested region *i.e.* $u_r \rightarrow 0$. It may be no longer the same when the boundary layer thickens $\bar{u}_r > 0$. Using two parameters δ_1 and δ_2 instead of measuring κ and u_r explicitly (and using relation **Eq. (32)**) tends to overestimate the temperature gradient prediction.

Fig. 19b could then be employed legitimately to fit the temperature radial distribution at each time step.

4.2.2 A priori interfacial gradient corrections on under-resolved steady simulations

The same process can be undertaken for coarse and non(entirely)-resolved simulations. This section aims to judge the ability to correct the temperature gradient from the coarse mesh using the fitting procedure. Corrected temperature profiles could later be coupled to the Eulerian field control volumes through convective and diffusive fluxes.

Fig. 20a shows that the use of an Erfc profile does not allow enhancing the temperature gradient evaluation whatever the fitting procedure employed. The hypotheses made to derive this profile are not always met in the interfacial region, and the simulation setup fails to align with all of these prerequisites (e.g., $Pr_l \gtrsim 1$). Consequently, its applicability to extrapolate to a broader range of operating conditions, such as ours with a large thermal layer and low spatial resolution ($\lesssim 40$ cells per bubble diameter), is not possible. Although the fitted profile continues to faithfully replicate the values on the coarse mesh, the expectations of improving the gradient prediction remain unfulfilled. Therefore, we have decided to discard this profile, no longer considering it as the best candidate in our research on temperature gradient correction at moderate Peclet numbers.

The SoV profile (see **Fig. 20b**) shows again a large dispersion depending on the fitting method employed. Methods using local values of temperature for calibration are not working well from a global point of view and tend to overestimate the gradient (Orange, Red and Green). Methods referred to as integral are closer to the fine mesh solution. Considering $u_r = 0$ (Light orange), some local enhancements are observed but it is too dispersed to assert the capability of the method. Finally, the two fitting types which show a clearer agreement with the fine mesh values are the two last integral methods:

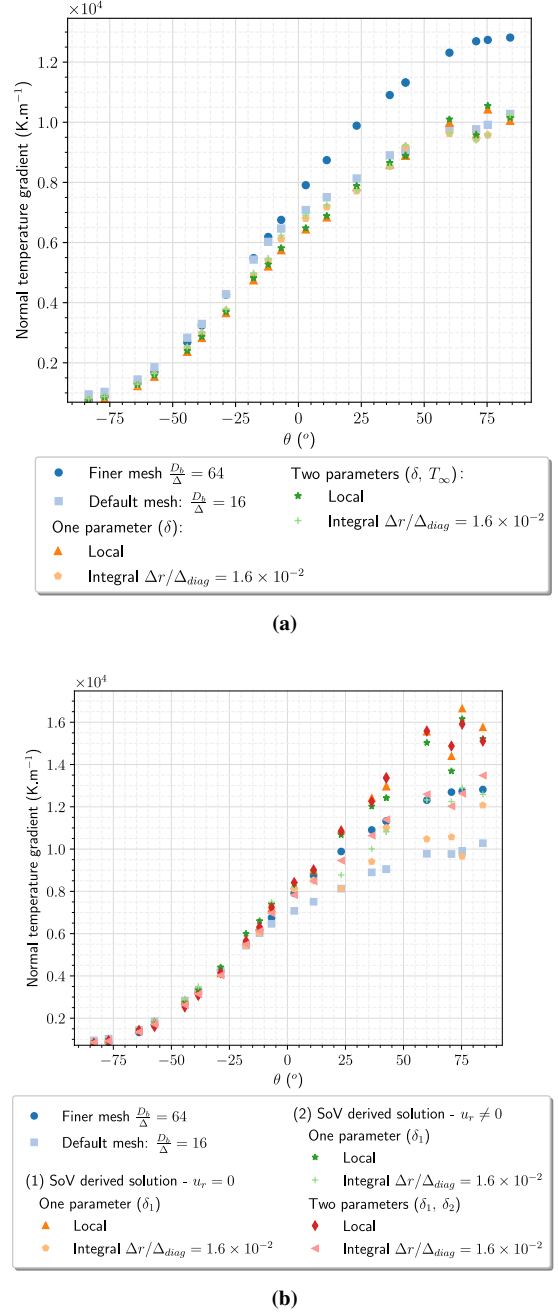


Figure 20: Fitted temperature profile in a narrow band around the interface: (a) Erfc function, (b) SoV derived solution. Profiles have been fitted on the coarse simulation at $Re_b \approx 62.5$, $Pr = 1.0$ and at a resolution of $D_b/\Delta = 16$

- δ_1 determination considering $u_r \neq 0$ (Light green in **Fig. 20b**): an overall agreement is observed in the bubble's equator and top regions $\theta > 0^\circ$ while the bubble's bottom which was already converged is well fitted. It is now clear that the two parameters should be linked by the direct relation using the curvature κ and the averaged normal velocity u_r .
- Fitting both free parameters δ_1 and δ_2 (Light red): omitting the relation linking δ_2 to δ_1 through curvature and averaged incoming bulk velocity is beneficial from a numerical

point of view (not velocity and curvature measurement requirements). It appears that the gain in prediction is good on the entire θ range.

Considering an averaged normal velocity component, even though it is not consistent with the mass conservation, is relevant as it embeds the effect of the upcoming fluid. Some further investigation at higher Prandtl confirms our observations. The predicted interfacial temperature gradient does not show a huge dispersion depending on the azimuthal ϕ coordinate which could be explained by the fact that the input of the method is only a zeroth order quantity (local or integral temperature value). **Fig. D.26** in **Appendix D** further illustrates the dispersion.

Finally, the second derivative of the post-processed quantity appears to be in better agreement (**Fig. 16**). In contrast, the derivative of the Erfc profile shows a plateau and linear variations at the interface (**Eq. (40)** and **Eq. (A.28)**), while the SoV-derived solution allows for a non-zero second derivative value and high-order variations when evaluated at the interface (see **Eq. (41)** and **Eq. (A.27)**). The fitted temperature and normal temperature gradient variations in the interface vicinity are illustrated in **Fig. D.27** and **Fig. D.28** of **Appendix D**. They illustrate the difficulties of the fitted solutions to significantly improve the prediction in the interface vicinity near the bubble top.

$$\frac{\partial \Theta^{Erfc}}{\partial r} = \frac{2}{\delta} \frac{e^{-\frac{r^2}{\delta^2}}}{\sqrt{\pi}} \left(\frac{2}{\delta} \text{ at } r = 0 \right) \quad (40a)$$

$$\frac{\partial^2 \Theta^{Erfc}}{\partial r^2} = -\frac{4r}{\delta^3} \frac{e^{-\frac{r^2}{\delta^2}}}{\sqrt{\pi}} \quad (0 \text{ at } r = 0) \quad (40b)$$

$$\frac{\partial \Theta^{SoV}}{\partial r} = \left(1 - e^{\frac{\delta}{\delta^*}} \right)^{-1} \times \left(\frac{\delta}{\delta_1 + \delta^* e^{\frac{\delta}{\delta^*}}} \right) \quad (\text{at } r = 0) \quad (41a)$$

$$\frac{\partial^2 \Theta^{SoV}}{\partial r^2} = \left(1 - e^{\frac{\delta}{\delta^*}} \right)^{-1} \times \left(\frac{\delta}{(\delta_1 \delta^*)^2} \right) \quad (\neq 0 \text{ at } r = 0) \quad (41b)$$

Supplementary results using this method are not extensively addressed in this paper as the second approach (LRS) is revealed to be more versatile (transposable to velocity) and interesting in the scope of simulating moderately large thermal boundary layers with low mesh requirements.

4.3 Laminar radial sub-resolution

In a second approach, the laminar radial sub-resolution has been performed on the simulation results. We expect the method to enhance the temperature gradient for coarse meshes. It is also

desirable that the method degenerates to the same underlying field value by increasing spatial resolution. A simple advection-diffusion equation is resolved for a given probe associated with a facet. The problem is resolved on a length of three diagonals of the coarse mesh ($D_b/\Delta = 16$) i.e. $2\Delta_{d^*} \approx 5\Delta$ with an increased resolution of around 32 points in the local 1D discretisation of **Eq. (35b)** i.e. we are considering around 6 times more points locally. For a simulation at 16 cells per diameter, the surface mesh counts roughly 1200 facets. Solving the problem on each one represents 38 400 degrees of freedom for the temperature field. It is therefore a very reasonable supplementary cost compared to the 0.4M and 25M cells of the coarse and fine simulations performed with 16 and 64 cells per diameter, respectively.

Interfacial temperature gradient enhancement study.

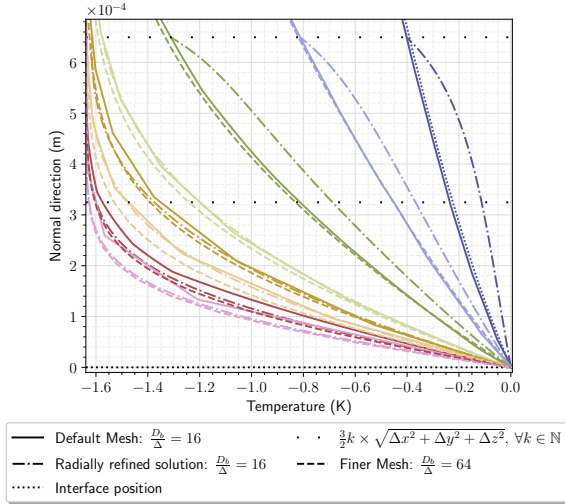
The velocity components are interpolated from the coarse field, while the tangential temperature gradient $\partial_\theta \Theta$, as per **Eq. (36d)**, and the tangential diffusion term, as indicated in **Eq. (36d)**, can be interpolated from either the coarse or fine Eulerian field. These tangential convective terms serve as radial source terms.

The idea is to observe the effect of considering different tangential source terms, starting with the convective effect alone and progressing to the inclusion of both tangential convection and diffusion, along with interfacial corrections, to ensure $\frac{\partial^r \Theta}{\partial \theta^r} = 0$. A summary of the seven tested combinations can be found in **Tab. 5**. The complexity of the source terms increases from cases (A) to (C), while the influence of using well-resolved terms is also explored in cases (D), (E), and (F).

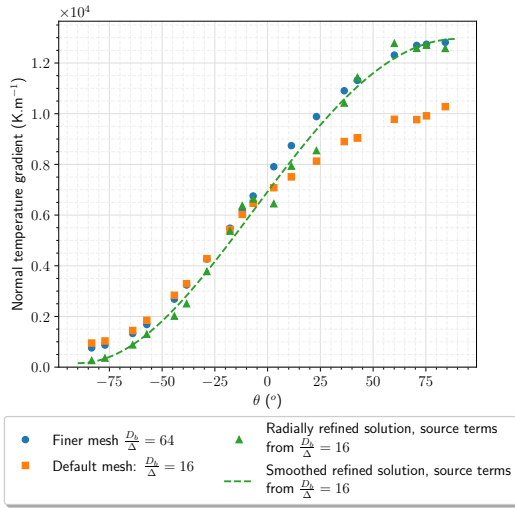
Cases (A), (B), and (F), as outlined in **Tab. 5**, are initially discussed in this section. This discussion is complemented by figures **Fig. 21**, **Fig. 22**, and **Fig. 23**, respectively. Each of these figures consists of two sub-figures: one illustrating the interfacial temperature gradient based on the bubble's position, and another for observing the predicted temperature profile over a finite length, which will prove valuable in a future coupling process.

According to **Fig. 21a** presenting the case (A) i.e. with a single tangential convective term only, the difference in the temperature field in the interface vicinity is small for the probes situated in the bubble's top region. However, for bottom probes, at the end of the sub-resolution domain $r = 2\Delta_{d^*}$, the normal temperature field derivative differs from the Eulerian one. We can incriminate the error made on the tangential term (convective term C^θ , defined in **Eq. (36)**) that influences the temperature variations significantly.

Heat is constantly injected at the interface because of the constant interfacial temperature (and the mass transfer being disabled) and is transported toward the subdomain's end. At the bubble's bottom, the liquid is pushed outward the bubble which causes the radial convective and diffusive terms to have the same sign if the tangential variations are not well captured. It explains the wrong slope of the temperature at the probe's end. Sign and evolution of the terms have been discussed in **Sec. 4.1.1**. According to **Fig. 12a**, a non-zero diffusion term is still visible at the bubble's bottom. This term is neglected in



(a)



(b)

Figure 21: The convective tangential term C^θ has been interpolated from the coarse simulation in case (A). (a) Refined temperature profile. (b) Local Nusselt number enhanced by the laminar radial sub-resolution. The technique has been performed at $Re_b = 62.5$ and $Pr = 1.0$ and for a resolution of $D_b/\Delta = 16$ and compared to the reference profile at $D_b/\Delta = 64$.

case (A) which contributes to the discrepancy observed (blue probes in **Fig. 21a**).

In case (A) presented in **Fig. 21b**, the normal temperature gradient near the interface is enhanced from the bubble's top until $\theta \approx 30^\circ$. However, the approach misses correcting the temperature gradient in the equator region and the bubble's wake. Once again it may be caused by a coarse evaluation of the tangential convective term. At the bubble's bottom, the temperature gradient is underestimated but it is less critical as it is quite small and it concerns a small area. It is also due to the second-order tangential derivative $\partial_\theta^2 \Theta$ which is neglected in the heat equation **Eq. (35)** but has a significant effect in this region.

The smoothed profile shown in **Fig. 21b** has been computed from a tweaked Levich-Ruckenstein profile (**Eq. (42)**) reformulated from [16] with coefficient in **Eq. (43)**). In particular when

$\theta = -\pi/2$, c should equal $\frac{\nabla T \cdot \mathbf{n}_\Gamma|_{\theta=-\pi/2}}{\nabla T \cdot \mathbf{n}_\Gamma|_{\theta=\pi/2}}$. The profile has been under-constrained to be fitted without using any top or bottom temperature gradient value ($\theta = \pi/2$ and $-\pi/2$, respectively). It is convenient when the maximum predicted value is not necessarily at the bubble's top (because of numerical variations). The ability of our LRS method can be better visualised.

$$\frac{\nabla T \cdot \mathbf{n}_\Gamma(\theta)}{\max(\nabla T \cdot \mathbf{n}_\Gamma)} = \frac{\sqrt{a} \cos^2\left(\frac{\pi/2-\theta}{2}\right)}{\sqrt{b + \cos(\pi/2 - \theta)}} + c \quad (42)$$

for $\theta \in [-\pi/2; \pi/2]$

$\max(\nabla T \cdot \mathbf{n}_\Gamma) = \nabla T \cdot \mathbf{n}_\Gamma _{\pi/2}$	Theoretical
$a = 3; \quad b = a - 1 = 2; \quad c = 0$	
$a = 9.37; \quad b = 8.35; \quad c = 1.22 \times 10^{-2}$	Fitted, Case (A)
$a = 1.80 \times 10^7; \quad b = 1.92 \times 10^7; \quad c = 4.56 \times 10^{-2}$	Fitted, Case (B)
$a = 4.23; \quad b = 3.40; \quad c = 3.90 \times 10^{-2}$	Fitted, Case (F)

In the second case (B), the diffusion term $\partial_\theta^2 \Theta/R^2$ is added to the resolution as a source term taken from the coarse solution. At the exact bubble's equator ($\theta = 0^\circ$), where tangential convective effects are the greatest, there is no particular enhancement. However, the prediction is better in the upper range $\theta \approx \{10^\circ; 25^\circ\}$ in **Fig. 22b**. The predicted values on both sides of the equator $\theta \approx \{-5^\circ; 5^\circ\}$ are quite dispersed and are still coarser than the reference measurement. These discrepancies are studied more precisely in the light of the Nusselt number integrand to ensure a global convergence of the Nusselt number although some dispersion in the predicted values is observed.

By interpolating both tangential terms C^θ and D^θ from the finest mesh, a clear improvement can be observed (Case F, see **Fig. 23a** and **Fig. 23b**). The source terms have been slightly offset to ensure a physical zero value at the exact interface position. In case (F), the velocity field is still coming from the coarse mesh (see **Tab. 5**). On average, an improvement in the temperature gradient prediction is visible in the bubble equator region. Bubble's top and bottom regions are still well resolved.

The particular case (F) is the best combination to mitigate the error in the configuration characterised by dimensionless values $Ar^* = 50$ and $Pr_l = 1$. It can be concluded from our analysis of cases (A-F) that it is required to model properly the tangential terms in the equator region to perform a decent temperature gradient correction. It becomes more and more significant as the Prandtl number increases.

Non-zero tangential temperature derivatives at the interface $\partial_\theta^2 \Theta|_\Gamma$ have a non-negligible effect as well. These terms must be treated with caution to not alter the regions where the solution is already converged (bubble's rear part). As our approach is systematic, it does not involve specific region detection. Therefore, it became necessary to ascertain the source of this deterioration.

Enhancement on the integral prediction and dispersion of the values.

Table 5: Summary of the observations depending on tested methods. Velocity is systematically corrected to ensure zero velocity at the probe end lying on the interface. It is done to respect the frame of reference in which we are working.

Case	Description	Related figures	Mesh related velocity field	Tangential terms	Mesh related tangential terms	Corrections
A	Raw sub-resolution	Fig. 21, Fig. 24a	Coarse	Convective C_{coarse}^θ	Coarse	-
B	Raw sub-resolution Diffusive term	Fig. 22	Coarse	Convective C_{coarse}^θ Diffusive D_{coarse}^θ	Coarse	-
C	Raw sub-resolution Interfacial correction	-	Coarse	Convective $C_{coarse, corr}^\theta$ Diffusive $D_{coarse, corr}^\theta$	Coarse	Tangential terms $\frac{\partial \Theta}{\partial \theta} \Big _\Gamma = 0; \frac{\partial^2 \Theta}{\partial \theta^2} \Big _\Gamma = 0$
D	Enhanced sub-resolution	-	Coarse	Convective C_{fine}^θ	Fine	-
E	Enhanced sub-resolution	Fig. 24b	Coarse	Convective C_{fine}^θ Diffusive D_{fine}^θ	Fine	-
F	Enhanced sub-resolution Interfacial correction	Fig. 23, Fig. 24c	Coarse	Convective $C_{fine, corr}^\theta$ Diffusive $D_{fine, corr}^\theta$	Fine	Tangential terms $\frac{\partial \Theta}{\partial \theta} \Big _\Gamma = 0; \frac{\partial^2 \Theta}{\partial \theta^2} \Big _\Gamma = 0$

If a local improvement has been observed in previous figures **Fig. 21**, **Fig. 22** and **Fig. 23**, it is mandatory to study the robustness of the approach over all the facets. Their orientation or their position in the mixed cells might have a significant effect on the method's efficiency. The integrand has been calculated for each facet (a thousand at $D_b/\Delta = 16$) and for each treatment of the source terms. Finally, the effect of three tested corrections on the integrand value of the temperature gradient (so the bubble Nusselt number) can be visualised in **Fig. 24a**, **Fig. 24b** and **Fig. 24c** for cases A, E and F respectively. The integrand is evaluated locally keeping in mind that the facet's surface area is uniformly distributed. In each case, the tangential term treatment has a clear effect on the dispersion especially in the equator region.

In case (A), the gain in the temperature gradient prediction at the bubble top is encouraging (see **Fig. 24a**) but it is not sufficient to correct its integral quantity. Introducing both fine tangential convective and diffusive source terms C^θ and D^θ , respectively (case E), an overall improvement is observed (**Fig. 24b**). Around the bubble equator, it still lacks a component that sweeps the heat and makes the transfer more intense.

Finally, in the present case ($Ar^* = 10, Pr_l = 1$), the use of the finer source terms coupled to a correction of both tangential terms (case F) by bringing them to zero at the interface makes the best prediction once regularised (**Fig. 24c**). The prediction in the region around $\theta \approx 25^\circ$ is very dependent on the convective tangential term evaluation C^θ . Using the fine field velocity does not improve significantly the results and is thus not presented here. Once again, the boundary condition applied for the velocity in the mixed cell is not directly geometrically related compared to the one employed in the temperature extension.

To sum up, an overall improvement is observed given the coarse source terms in **Fig. 24a**. Some values are underestimated in the equator region *i.e.* where the normal velocity is almost zero and in which stall will occur at higher Reynolds numbers. A wrong prediction of the tangential source terms in this region can be critical. The maximum value of the integrand is overestimated and the distribution is offset in the bubble's top region. The dispersion is relatively high but is balanced as the computation of the overall Nusselt number shows a significant improvement.

Using finer source terms allows a net gain in dispersion as exposed in **Fig. 24b**. However, the collection of points is again offset in the bubble's top region. The dispersion is mitigated using finer terms.

Finally, by correcting the source terms **Fig. 24c** (Case F), the dispersion is slightly increased but the average values at a given θ are close to the fine mesh. The regularisation (dash-line) is in excellent agreement with the fine mesh solution.

For each tested treatment of the source terms, the overall Nusselt number with correction has been computed and compared to the reference (see **Tab. 6**). Overall Nusselt number is given for a perfect sphere of radius R_b (diameter D_b) by **Eq. (44)**.

$$Nu_b = D_b R_b^2 / \Delta T \int_{S_\Gamma} (\nabla T \cdot \mathbf{n}_\Gamma) \sin(\theta) d\theta d\phi \quad (44)$$

where ϕ varies between 0 and 2π . Results are presented in **Tab. 6**. The column "Reference errors" gives the Nusselt underestimation of the coarse mesh for each case.

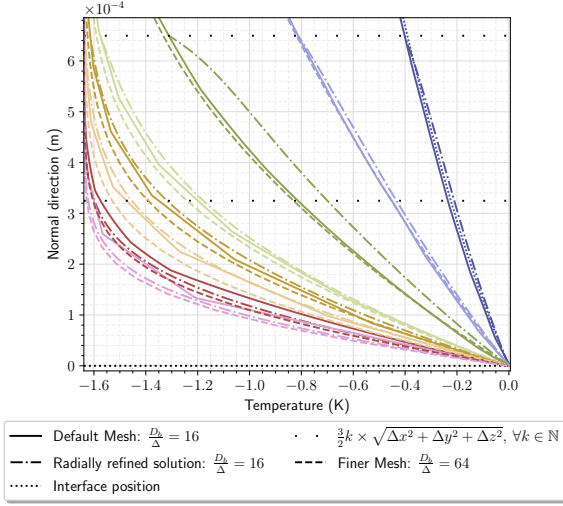
A clear improvement is observed at a moderate Reynolds number reducing the relative error to reach 8-12 % of the reference solution depending on the liquid Prandtl value Pr_l *i.e.* depending on the thermal boundary layer thickness. Relative error drops to a range of 1-4 % using the tangential source terms interpolated from the finest mesh solution in case (F).

Adding a surface diffusion source term from the coarse field in case (B) reduces the gain in precision. It is incriminated to the high-order character of this term which is not well captured in some regions in the actual coarse simulations without a sub-model. However, once corrected to ensure a zero value at the interface (*i.e.* shifting the profile to enforce $D^\theta = 0$ on cases (C) and (F)), the gain can be significant. Correcting the interfacial value of the surface diffusion D^θ to zero allows to mitigate the error in regions of high variations while keeping the benefits in well-resolved regions.

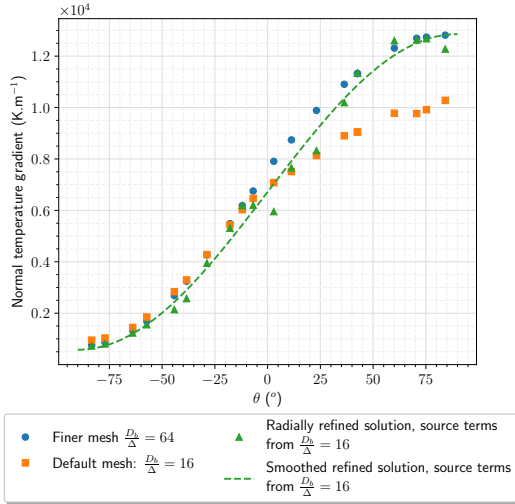
Surprisingly, the use of D^θ is no longer beneficial when the source terms come from the finest simulation at high Prandtl numbers. When the Prandtl increases, the boundary layer thickness is thinner. D^θ must be less well captured for both $Pr = 2.5, 5$ than for $Pr = 1$. This term and the higher order derivatives of Θ along θ are thus potentially showing a greater

Table 6: Overall Nusselt number prediction according to each tested method (A-F) exposed in **Tab. 5**. Reference error is coloured in red. The green colour indicates the best prediction for both coarse and fine source terms.

Archimedes number (A_r)	Prandtl number (Pr)	$\frac{D_b}{\Delta}$		Resolution ratio	Reference error (%)	A		B		C		Best gain factor	D		E		F		Best gain factor		
		Value	Value			Value	Error (%)	Value	Error (%)	Value	Error (%)		Value	Error (%)	Value	Error (%)	Value	Error (%)			
10	1.0	12	3.02	48	3.17	4	4.76	3.10	2.18	3.09	2.71	3.14	1.17	4.06	3.12	1.78	3.11	2.08	3.13	1.21	3.92
	2.5	16	4.26	96	4.46	6	4.48	4.26	4.42	4.25	4.58	4.29	3.73	1.20	4.34	2.66	4.34	2.74	4.37	2.06	2.17
	5.0	24	5.34	96	5.53	4	3.38	5.34	3.44	5.33	3.54	5.36	3.10	1.09	5.40	2.29	5.40	2.28	5.41	2.06	1.64
50	1.0	16	7.40	64	8.81	4	16.06	7.96	9.67	7.95	9.76	8.05	8.67	1.85	8.24	6.46	8.26	6.32	8.49	3.61	4.44
	2.5	22	10.47	90	13.00	4.1	19.46	11.87	8.65	11.85	8.87	11.88	8.61	2.26	12.80	1.53	12.79	1.60	12.35	5.02	12.70
	5.0	22	11.87	90	17.41	4.1	31.78	15.19	12.72	15.17	12.87	15.27	12.29	2.59	17.28	0.73	17.27	0.77	16.28	6.45	43.46



(a)



(b)

Figure 22: Both convective and diffusive tangential terms C^θ and D^θ have been interpolated from the coarse simulation (Case B). (a) Refined temperature profiles. (b) Normal temperature gradient enhanced by the laminar radial sub-resolution. The technique has been performed at $Re_b = 62.5$ and $Pr = 1.0$ and for a resolution of $D_b/\Delta = 16$ and compared to the reference profile at $D_b/\Delta = 64$.

error although it is decreasing in magnitude with the boundary layer thickness. Sticking to the tangential term C^θ for a higher-aimed Reynolds number appears to be the best option.

At the lowest Reynolds number, the gain in precision is not as high as the relative error was already low with the coarse

resolution. The error is still reduced by a factor 1.6 to 4 depending on the Prandtl number and it reaches a very low level. For this flow regime, the resolution required to resolve correctly the bubble shape and velocity is already satisfied. In that case, the thermal sub-resolution approach is not very interesting for $Pr \in [1; 5]$.

Overall, the **LRS** method proposed in this paper is promising even using the coarse source terms and especially at higher Peclet numbers *i.e.* when the boundary layer will get thinner. The source terms (C^θ and D^θ) need to be corrected to ensure a better prediction of the temperature in the interfacial region. A possible improvement of the sub-resolution method could be achieved by modelling these terms. It could potentially lighten vector projection procedures along the tangential axis. Some investigations will be conducted using the fine simulation results to perform further modelling and draw a clear tendency according to local variations such as velocity gradient (and other invariant fields).

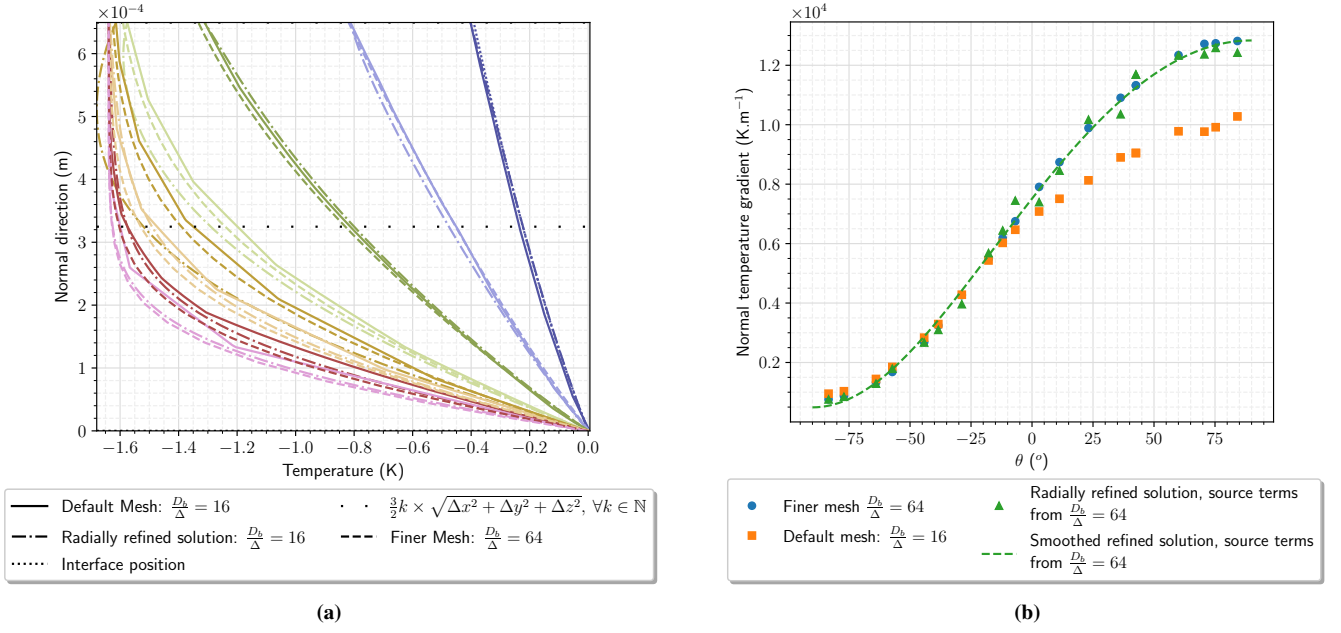


Figure 23: Both convective and diffusive tangential terms C^θ and D^θ have been interpolated from the fine simulation (Case F). (a) Refined temperature profiles. (b) Normal temperature gradient enhanced by the laminar radial sub-resolution. The technique has been performed at $Re_b = 62.5$ and $Pr = 1.0$ and for a resolution of $16 D_b/\Delta$ and compared to the profile at $64 D_b/\Delta$.

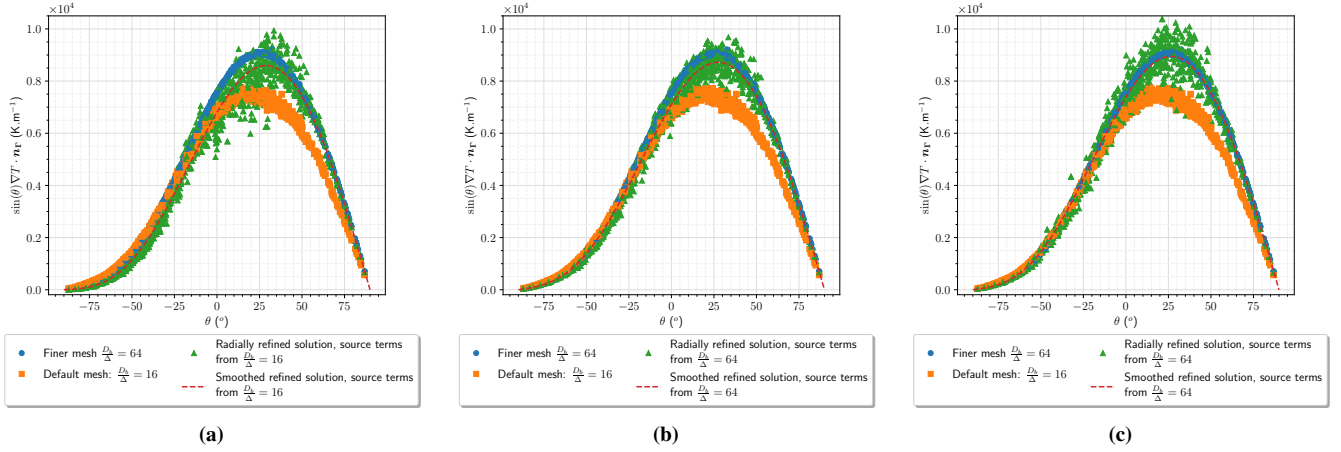


Figure 24: Normal temperature gradient integrand for a perfect sphere considering axisymmetry: $\sin(\theta)\nabla T \cdot n_\Gamma$. The solution has been computed for all the interface's facets. (a) Source terms and velocity from the coarse mesh (Case A), (b) Source terms from the fine mesh and velocity from the coarse mesh (Case E), (c) Source terms from the fine mesh and velocity from the coarse mesh. Convective (C^θ) and diffusive (D^θ) tangential source terms are corrected to exhibit a zero interfacial value (Case F).

5 Conclusions

The present work has been carried out on thermal boundary layer modelling near a viscous bubble interface. DNS reference data of heat transfer around a rising bubble was produced by a Front-Tracking solver in addition to a ghost fluid approach and a quasi-static sub-grid diffusion model in the interface vicinity. Two steady dynamical regimes have been obtained at $Ar^* = \{10; 50\}$ corresponding to bubble Reynolds numbers of $Re_b = \{3.6; 62.5\}$. Thermal cases have been simulated for each dynamical regime at three different liquid Prandtl

numbers $Pr_l = \{1, 2.5, 5\}$. Spatial resolutions expressed in cells per bubble diameter vary from 12 to 96 for $Ar^* = 10$ and between 16 and 90 for $Ar^* = 50$, respectively.

A hierarchy of radial and tangential convective and diffusive terms showed three distinct regimes. The tangential and normal convective terms are relevant to consider in the interface vicinity. On the other hand, the normal diffusive term is dominant over the tangential one at every bubble elevation coordinate.

Global Nusselt numbers measured in each case have been compared to a robust correlation of the literature. The convergence study shows that the spatial resolution requirement is

proportional to the Prandtl number.

A literature review on sub-grid models for boundary layers has been performed where different aspects were discussed and some improvements have been proposed. Either semi-analytical profiles undergoing a fitting process or 1D laminar sub-resolutions were considered.

Regarding the fitting of an analytical solution, the SoV profile **Eq. (30)**, established within an osculating sphere frame of reference, incorporates considerations for the local mean curvature and the tangential convective term, contrasting with the commonly used plane solution (zeroth order surface, erfc function) found in the existing literature. Furthermore, the impact of a constant normal velocity has been incorporated.

Fitting the resulting SoV profile has shown some enhancement in the gradient prediction. However, the difficulties linked to the free-parameter determination (Newton's algorithm), coupled with its limited applicability, make it difficult to work with. This analytical approach poses challenges when dealing with larger boundary layers ($\delta \lesssim R$, $\Delta_{x,y,z} \lesssim R$).

The numerical radial sub-resolution is very interesting in enhancing the temperature gradient evaluation at the interface from coarse initial meshes. It proved to be particularly effective in the region subjected to the incident fluid where a local steady-state is ensured even when tangential derivatives, feeding the sub-resolution, are poorly reconstructed.

The effect of the tangential terms around the bubble equator is also clearly observed and the necessity to capture properly the latter is key to performing sub-grid modelling. The temperature gradient once weighting by the surface area in this region brought the main contribution to the overall bubble Nusselt number.

The LRS approach has demonstrated better capabilities than the analytical approach. Besides, it exhibits a greater improvement at higher Prandtl numbers (with thinner thermal layers) while the original sub-grid pure diffusion approach (as in Ghost-Fluid methods) becomes less representative of the underlying physics for a given mesh cell resolution (higher Peclets lead to weaker thermal diffusion). Our approach benefits from the scale separation that occurs as the thermal boundary layer thickness diminishes, constituting one of its strengths.

The degrees of freedom added to the numerical resolution are reasonable. Besides, an extension of the method could be achieved in the case of a two-phase LES simulation by incorporating a turbulent contribution into the thermal diffusion term. This approach still remains independent of the resolution of the velocity field.

6 Declaration of Competing Interest

The authors declare no conflicts of interest or personal relationships that could have interfered with the present paper.

7 Acknowledgement

The authors would like to thank CEA/DES and TGCC for providing reliable computational resources for performing the

DNS calculations. This work was granted access to the IRENE supercomputer's HPC resources under the allocations A0102B07712 and A1202B07712.

8 CRediT author statement

Mathis GROSSO: Conceptualisation, Validation, Formal Analysis, Investigation, Data Curation, Visualisation, Writing - original draft, review & editing.

Guillaume BOIS: Conceptualisation, Validation, Formal Analysis, Writing - review & editing, Supervision, Project administration, Funding acquisition.

Adrien TOUTANT: Conceptualisation, Validation, Formal Analysis, Supervision, Writing - review & editing.

Appendix A Derivation of an analytical solution

Appendix A.1 Temperature equation in the osculating sphere frame of reference

To derive an analytical solution or to work with simplified equations taking into account the local curvature, some analytical developments have been conducted. By choosing to use the spherical equation, *i.e.* by re-writing the problem in the osculating sphere frame of reference we wish to align with the principal direction of variations. The general instantaneous and local temperature equation expressed for a single phase and in non-conservative form (only the liquid phase is resolved) can be written in dimensional and dimensionless forms by **Eq. (A.1a)** and **Eq. (A.1b)** respectively.

$$\frac{\partial T}{\partial t} + \mathbf{u} \cdot \nabla T = \alpha_l \Delta T \quad (\text{A.1a})$$

$$\frac{\partial \Theta}{\partial t^*} + \mathbf{u}^* \cdot \nabla^* \Theta = \frac{1}{Re_b Pr_l} \Delta^* \Theta \quad (\text{A.1b})$$

For this particular problem, the characteristic length could be chosen to be the bubble diameter $L = D_b$. The characteristic velocity U is chosen to be the terminal velocity. A characteristic time t^* is built upon both previously introduced characteristic variables.

A hypothesis is made concerning the non-dimensionalisation of the temperature. In the case where it is not possible to define an infinite temperature, a local temperature value denoted T_δ is used (for each sub-problem). The reference temperature is $T_0 = T^{sat}$. It is common to solve around the constant saturation temperature *i.e.* $T \leftarrow (T - T^{sat})$. One can write:

$$\Theta = \frac{T_\delta - T}{T_\delta - T^{sat}} = 1 - \frac{T}{T_\delta} \quad (\text{A.2a})$$

$$d\Theta = \frac{\partial \Theta}{\partial T} dT + \frac{\partial \Theta}{\partial T_\delta} dT_\delta = -\frac{dT}{T_\delta} + T \underbrace{\frac{dT_\delta}{T_\delta^2}}_{\approx 0} \quad (\text{A.2b})$$

From **Eq. (A.2)**, the variations of dT_δ are assumed to be zero locally. It is noticeable that the characteristic variable T_δ used

to non-dimensionalise the current problem is inherently related to a single bubble configuration.

The single-phase instantaneous and local temperature equation in a moving spherical coordinate system writes:

$$\begin{aligned}
& \overbrace{\frac{D_t \Theta}{Dt}}^{D_t \Theta} + \overbrace{(u_r - u_{r,\Gamma}) \frac{\partial \Theta}{\partial r}}^{C^r} + \overbrace{\frac{u_\theta}{r} \frac{\partial \Theta}{\partial \theta}}^{C^\theta} + \overbrace{\frac{u_\phi}{r \sin(\theta)} \frac{\partial \Theta}{\partial \phi}}^{C^\phi} \\
D^r \left\{ \right. &= \frac{\alpha_l}{r^2} \frac{\partial}{\partial r} \left(r^2 \frac{\partial \Theta}{\partial r} \right) \\
D^\theta \left\{ \right. &+ \frac{\alpha_l}{r^2 \sin(\theta)} \frac{\partial}{\partial \theta} \left(\sin(\theta) \frac{\partial \Theta}{\partial \theta} \right) \\
D^\phi \left\{ \right. &+ \frac{\alpha_l}{r^2 \sin(\theta) \cos(\theta)} \frac{\partial^2 \Theta}{\partial \phi^2}
\end{aligned} \tag{A.3}$$

$u_{r,\Gamma}$ denotes the interface radial velocity.

As each local frame of reference is moving over time, the time derivative appearing in the spherical equation is a material derivative denoted D_t in each marker frame of reference (or associated osculating sphere in **Fig. 11**):

$$\begin{aligned}
\left. \frac{D\Theta}{Dt} \right|_\Gamma &= \frac{\partial \Theta}{\partial t} + \frac{d\mathbf{OM}_{sph}}{dt} \cdot \nabla \Theta \\
&= \frac{\partial \Theta}{\partial t} + \left[\frac{dr}{dt} \tilde{\mathbf{e}}_r + r \frac{d\tilde{\mathbf{e}}_r}{dt} \right] \cdot \nabla \Theta \\
&\approx \frac{\partial \Theta}{\partial t} + (\mathbf{u}_\Gamma \cdot \mathbf{n}_\Gamma) (\nabla \Theta \cdot \mathbf{n}_\Gamma) \\
&= \frac{\partial \Theta}{\partial t} + u_{r|\Gamma} \frac{\partial \Theta}{\partial r}
\end{aligned} \tag{A.4}$$

The time derivative of $\tilde{\mathbf{e}}_r$ is neglected. It could potentially be linked to the curvature evolution over time.

As a consequence, the fluid velocity is thus referring locally to the liquid relative velocity to the interface *i.e.* the liquid velocity from which the normal interface velocity component has been subtracted:

$$\begin{aligned}
\mathbf{u}_{l \leftrightarrow \Gamma} &= \mathbf{u} - (\mathbf{u}_\Gamma \cdot \mathbf{n}_\Gamma) \mathbf{n}_\Gamma \\
&= \mathbf{u} - u_{r|\Gamma} \mathbf{n}_\Gamma
\end{aligned} \tag{A.5}$$

Only the normal component of the interface velocity is employed. In fact, because of the shear of the two moving fluids, the tangential velocity is not zero at the interface even in a steady-state configuration. It implies that the basis is associated with a geometric displacement of the interface *i.e.* the markers are not advected by the fluid tangentially.

For the sake of clarity, \mathbf{u} will be kept in the following section but will refer to $\mathbf{u}_{l \leftrightarrow \Gamma}$ defined in **Eq. (A.5)**. To derive our analytical approaches, the total derivative $D_t \Theta$ in **Eq. (A.3)** is assumed to be zero. This is especially true at the interface where the temperature is kept constant. The quasi-steadiness of the solution in the interface vicinity can be justified by the fact that the boundary layer around the bubble will be only slightly perturbed by other bubbles' wakes once settled. It is expected that the bubbles' acceleration will be low in a statistically stationary swarm. The initial transient will rapidly affect the local far-field

temperature T_δ^θ , which in turn influences the sub-resolution approach boundary conditions. It might be sufficient to capture the transient accurately. Capturing the overall vapour growth rate is already a difficult task and we think the proposed approach will lead to a useful gain in accuracy and knowledge for industrial applications related to heat transfer.

The solution is expected to vary strongly in the radial direction $\tilde{\mathbf{e}}_r$. As a consequence, the normal convective term as well as the second-order normal diffusive term are kept in the general equation **Eq. (A.3)**. To simplify our study in the first approach, an axisymmetric problem has been chosen. Variations along direction $\tilde{\mathbf{e}}_\phi$ are then zero in any bubble-osculating sphere frame of reference. Finally, the first-order tangential term has been kept. The tangential diffusive term has been neglected according to preliminary observations shown in **Sec. 4.1** and according to numerous works performed in the literature [26, 27, 29, 32]. However, it has been observed that locally, it can have a positive effect on the prediction capability of the method.

As underlined previously, the tangential component of the velocity u_θ is non-zero and there is not a real consensus on considering this term in the temperature equation. Some authors are favouring this term against the normal convective term [26, 27] by using an analytical solution of the simplified problem (see **Eq. (23a)**).

To avoid any lack of generality, the simplified steady-state advection-diffusion **Eq. (A.6)** has been extensively considered in the current paper and **Sec. 3**.

$$\begin{aligned}
u_r \frac{\partial \Theta}{\partial r} + \frac{u_\theta}{r} \frac{\partial \Theta}{\partial \theta} &= \frac{\alpha_l}{r^2} \frac{\partial}{\partial r} \left(r^2 \frac{\partial \Theta}{\partial r} \right) \\
&= \alpha_l \left(\frac{2}{r} \frac{\partial \Theta}{\partial r} + \frac{\partial^2 \Theta}{\partial r^2} \right)
\end{aligned} \tag{A.6}$$

The tangential diffusive terms employed in the sub-resolution process write:

$$D^\theta = \frac{\alpha_l}{r^2 \sin(\theta)} \frac{\partial}{\partial \theta} \left(\sin(\theta) \frac{\partial \Theta}{\partial \theta} \right) \tag{A.7a}$$

$$\begin{aligned}
&= \underbrace{\frac{\alpha_l \cos(\theta)}{r^2 \sin(\theta)} \frac{\partial \Theta}{\partial \theta}}_{D_1^\theta} + \underbrace{\frac{\alpha_l}{r^2} \frac{\partial^2 \Theta}{\partial \theta^2}}_{D_2^\theta} \\
&= \frac{\alpha_l}{r^2} \frac{\partial^2 \Theta}{\partial \theta^2} \quad \text{for } \theta = \pi/2
\end{aligned} \tag{A.7b}$$

Appendix A.2 Forms of solution of a simplified equation

To achieve an interfacial gradient correction in the style of Weiner *et al.* [26], Cai *et al.* [31] at steady state or like in the approach of Aboulhasanzadeh *et al.* [27] or Classen *et al.* [32] in a time-dependent fashion (see **Sec. 3.1**), an equation describing the boundary layer radially is needed.

Previous authors have not taken into account the mean curvature κ in their previous forms of solutions. Moreover, they

made some assumptions concerning the convective terms to settle their approaches.

To find a solution to **Eq. (A.6)**, a method of separation of variables (SoV), commonly used in heat transfer problems, has been explored. In our case, this method is applicable because the temperature equation is linear and the boundary conditions are finite (Θ equals 1 at the interface and 0 from a certain distance).

As a reminder, the methods of SoV consist of expressing the variable Θ into a product of a function of one variable. In our case, Θ writes:

$$\Theta(r, \theta) = f(r)g(\theta) \quad (\text{A.8})$$

Eq. (A.8) is then re-introduced in **Eq. (A.6)** but u_r and u_θ directions of variation are constrained to solve the problem. u_r can only vary in the radial direction whereas u_θ can vary in either radial or tangential directions. Two forms are possible and are expressed through **Eq. (A.9a)** and **Eq. (A.9b)**.

$$A = \frac{\frac{\partial g(\theta)}{\partial \theta}}{g(\theta)} = \frac{\frac{\partial^2 f(r)}{\partial r^2} + \left(\frac{2}{r} - \frac{u_r(r)}{\alpha_l}\right) \frac{\partial f(r)}{\partial r}}{f(r)} \frac{\alpha_l r}{u_\theta(r)} \quad (\text{A.9a})$$

$$A' = u_\theta(\theta) \frac{\frac{\partial g(\theta)}{\partial \theta}}{g(\theta)} = \frac{\frac{\partial^2 f(r)}{\partial r^2} + \left(\frac{2}{r} - \frac{u_r(r)}{\alpha_l}\right) \frac{\partial f(r)}{\partial r}}{f(r)} \alpha_l r \quad (\text{A.9b})$$

As we wish to solve this simplified problem locally and radially, it is more consistent to look for the solution of equation **Eq. (A.9a)**. It is also expected that the variables are strongly varying in the normal direction including the tangential velocity u_θ (see **Fig. 14.b**).

Besides, $\Theta(r, \theta)$ is not cancelling at the interface so neither $g(\theta)$ or $f(r)$ are zero at the interface. However, Θ is cancelling at a certain distance from the interface while its derivatives are decreasing as well. As a consequence, it is physically admissible to find a solution using the SoV method.

Given **Eq. (A.9a)**, both sides of the equations are functions of separate variables. As a consequence, each side of the equation is equal to an undetermined constant A which leads to two separate Ordinary Differential Equations (ODEs) given by **equation (A.10)**.

$$\frac{\partial g(\theta)}{\partial \theta} - Ag(\theta) = 0 \quad (\text{A.10a})$$

$$\frac{\partial^2 f(r)}{\partial r^2} + \left(\frac{2}{r} - \frac{u_r}{\alpha_l}\right) \frac{\partial f(r)}{\partial r} - \frac{Au_\theta(r)}{\alpha_l r} = 0 \quad (\text{A.10b})$$

g can be solved straightforwardly according to constant A . Another constant of integration $B \in \mathbb{R}$ appears in the **Eq. (A.11)** and will be determined later.

$$g(\theta) = Be^{A\theta} \quad (\text{A.11})$$

To be able to solve **Eq. (A.10b)** analytically, it is required to make further simplifications. The coefficients of the characteristic polynomials are *a priori* some functions of r . However, to find a solution, the velocity components must be constants and

the terms $\propto 1/r$ can be approached at zero order by the mean curvature value κ in the interface vicinity (see **Eq. (A.12)** given **Eq. (A.13)**).

$$\kappa = \kappa_1 + \kappa_2 = \frac{1}{R_1} + \frac{1}{R_2} = \frac{2}{R} \quad (\text{A.12})$$

$$\begin{aligned} \frac{2}{r} &= \frac{2}{R} + o(1) \\ &= \kappa + o(1) \end{aligned} \quad (\text{A.13})$$

One can see that the continuity equation should also be approximated to be coherent with a constant velocity field:

$$\begin{aligned} \nabla_{sph} \cdot \mathbf{u} &= \frac{2u_r}{r} + \frac{\partial u_r}{\partial r} + \frac{1}{r} \frac{\partial u_\theta}{\partial \theta} \\ &\approx \kappa u_r + \frac{\partial u_r}{\partial r} + \frac{\kappa}{2} \frac{\partial u_\theta}{\partial \theta} \end{aligned} \quad (\text{A.14})$$

A zero divergence can not be achieved with a constant normal velocity $u_r \neq 0$ except if a source term is taken into account in the *RHS*.

Symbolic mathematical software such as SageMath was not able to determine a general form of solution for higher-order expansions of u_r , u_θ and $1/r$. The ODE in the radial direction **Eq. (A.10b)** can be simplified in the interface vicinity $r = R$ to **Eq. (A.15a)** and leads to characteristic **equation (A.15b)**.

$$\frac{\partial^2 f(r)}{\partial r^2} + \left(\frac{\kappa\alpha_l - u_r}{\alpha_l}\right) \frac{\partial f(r)}{\partial r} - \frac{\kappa Au_\theta}{2\alpha_l} \approx 0 \quad (\text{A.15a})$$

$$\lambda^2 + \left(\frac{\kappa\alpha_l - u_r}{\alpha_l}\right) \lambda - \frac{\kappa Au_\theta}{2\alpha_l} = 0 \quad (\text{A.15b})$$

The problem now reduces to a simple second-order system whose discriminant is:

$$\begin{aligned} \Delta &= \left(\frac{\kappa\alpha_l - u_r}{\alpha_l}\right)^2 + \frac{2\kappa u_\theta A}{\alpha_l} \\ &= \frac{\kappa^2 \alpha_l^2 + u_r^2 + 2\kappa\alpha_l (Au_\theta - u_r)}{\alpha_l^2} \end{aligned} \quad (\text{A.16})$$

Sticking to non-oscillatory solutions (*i.e.* $\Delta > 0$), the two roots $\lambda_{1,2}$ equal:

$$\lambda_{1,2} = \frac{(u_r - \kappa\alpha_l) \pm \sqrt{\kappa^2 \alpha_l^2 + u_r^2 + 2\kappa\alpha_l (Au_\theta - u_r)}}{2\alpha_l} \quad (\text{A.17})$$

For the sake of simplicity, let us define in **Eq. (A.18)** δ_1 and δ_2 , which are characteristic length scales associated with the general forms of solutions of **Eq. (A.15b)**. The relations between δ_1 and δ_2 are derived by combining the two roots λ_1 and

λ_2 .

$$\delta_1 = -\frac{1}{\lambda_1} = \frac{\alpha_l \delta_2}{\alpha_l + \delta_2 (\kappa \alpha_l - u_r)} \quad (\text{A.18a})$$

$$\delta_2 = \frac{1}{\lambda_2} = \frac{\alpha_l \delta_1}{\alpha_l + \delta_1 (u_r - \kappa \alpha_l)} \quad (\text{A.18b})$$

The general form of function f is straightforwardly found given two constants $C, D \in \mathbb{R}$:

$$\begin{aligned} f(r) &= C e^{\lambda_1 r} + D e^{\lambda_2 r} \\ &= C e^{-\frac{r}{\delta_1}} + D e^{\frac{r}{\delta_2}} \end{aligned} \quad (\text{A.19})$$

Overall non-oscillatory forms of solution for Θ are finally given by **Eq. (A.20)**.

$$\Theta(r, \theta) = B e^{A\theta} \left[C e^{\frac{r}{\delta_1}} + D e^{\frac{r}{\delta_2}} \right] \quad (\text{A.20})$$

Constants A, B as well as C and D in \mathbb{R} should then be found. However, simplifications made to solve for Θ have already constrained the solution space so that imposing a constant temperature at the interface leads to a constant solution. Since, $e^{A\theta} > 0, \forall A \in \mathbb{R}$, A or B must equal zero to satisfy the "global" interface zero tangential temperature gradient. In other words the saturation temperature condition $\Theta(r=0, \theta) = 1, \forall \theta \in [0, \pi]$ lead to $A = 0$ to have a non-trivial solution.

However, it should be kept in mind that we are solving several heat transfer problems locally *i.e.* for each osculating sphere (subscript (θ)). Instead, the saturation temperature can be weakly imposed locally by letting B, C and D vary with respect to θ so that the following boundary condition holds:

$$\begin{aligned} \text{B.C.1: } \Theta(r=0, \theta) &= 1 \\ \Leftrightarrow B_{(\theta)} &= \frac{1}{C_{(\theta)} + D_{(\theta)}} \end{aligned} \quad (\text{A.21})$$

In a real 3D scenario, the \tilde{e}_θ direction should then be chosen such as the direction of the tangential velocity corresponds to the surface projection of \mathbf{u} :

$$u_\theta \tilde{e}_\theta \equiv \mathbf{u} - (\mathbf{u} \cdot \mathbf{n}_\Gamma) \mathbf{n}_\Gamma \quad (\text{A.22})$$

To consider further local complexity like the two principal directions of curvature, the equations should be entirely rewritten in curvilinear coordinates.

If the second boundary is imposed at $r \rightarrow \infty, \exists (C_{(\theta)}, D_{(\theta)}) \in \mathbb{R}^2, \Theta(r \rightarrow \infty, 0) = 0$. $C_{(\theta)}$ and $D_{(\theta)}$ can take multiple values over \mathbb{R} to satisfy the second boundary condition and the problem is under-determined. Instead, it will be considered that Θ equals zero at a certain distance $\delta(\theta)$. In other words, the problem is re-constrained by local information on the far-field temperature T_δ^θ . It is translated by the following boundary condition:

$$\begin{aligned} \text{B.C.2: } T(r=\delta(\theta), \theta) &= T_\delta^\theta \\ \Leftrightarrow \Theta(r=\delta(\theta), \theta) &= 0 \end{aligned} \quad (\text{A.23})$$

This second boundary condition can be introduced to relate $C_{(\theta)}$ to $D_{(\theta)}$:

$$C_{(\theta)} = -D_{(\theta)} e^{\delta\left(\frac{1}{\delta_2} + \frac{1}{\delta_1}\right)} \quad (\text{A.24})$$

The overall solution is finally given through **Eq. (A.25)**.

$$\begin{aligned} \Theta(r, \theta) &= \frac{C_{(\theta)}}{C_{(\theta)} + D_{(\theta)}} e^{-\frac{r}{\delta_1}} + \frac{D_{(\theta)}}{C_{(\theta)} + D_{(\theta)}} e^{\frac{r}{\delta_2}} \\ &= \left(1 - e^{\delta\left(\frac{1}{\delta_2} + \frac{1}{\delta_1}\right)}\right)^{-1} \left(e^{\frac{r}{\delta_2}} - e^{\delta\left(\frac{1}{\delta_2} + \frac{1}{\delta_1}\right)} e^{\frac{r}{\delta_1}}\right) \\ &= \left(1 - e^{\frac{\delta(2\alpha_l + \delta_1(u_r - \kappa\alpha_l))}{(\alpha_l \delta_1)}}\right)^{-1} \\ &\times \left(e^{\frac{r(2\alpha_l + \delta_1(u_r - \kappa\alpha_l))}{(\alpha_l \delta_1)}} - e^{\frac{\delta(2\alpha_l + \delta_1(u_r - \kappa\alpha_l))}{(\alpha_l \delta_1)}} e^{\frac{r}{\delta_1}}\right) \end{aligned} \quad (\text{A.25})$$

In the case where $u_r = 0$ (free-divergence field), the equation writes:

$$\begin{aligned} \Theta(r, \theta) &= \frac{C_{(\theta)}}{C_{(\theta)} + D_{(\theta)}} e^{-\frac{r}{\delta_1}} + \frac{D_{(\theta)}}{C_{(\theta)} + D_{(\theta)}} e^{\frac{r}{\delta_2}} \\ &= \left(1 - e^{\frac{\delta(2 - \kappa\delta_1)}{\delta_1}}\right)^{-1} \left(e^{-\frac{r(\kappa\delta_1 - 1)}{\delta_1}} - e^{\frac{\delta(2 - \kappa\delta_1)}{\delta_1}} e^{\frac{r}{\delta_1}}\right) \end{aligned} \quad (\text{A.26})$$

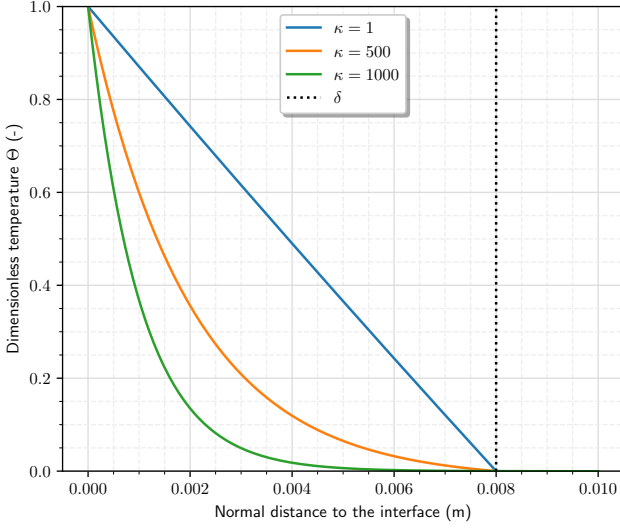
This form of solution is plotted in **Fig. A.25a** for given values of constant A, u_r, u_θ and three values of curvature κ . It leads to three values of δ_1 giving the root expression **Eq. (A.17)**. When $\kappa \rightarrow 0$ and $u_r = 0$, the approximated tangential term $u_\theta \kappa / 2 \partial_\theta \Theta$ cancels naturally. Then, the discriminant Δ tends to 0 and the solution tends to be a planar diffusion problem. In the case where $\kappa \rightarrow 0, u_r < 0$, the solution corresponds to a decreasing exponential solution. It embeds a normal velocity component u_r .

It should be underlined once again that our approach, as presented here, remains quasi-static. The value of $T_\delta^\theta, \delta(\theta)$ are re-evaluated at each time-step and for each value of θ thanks to interpolation of the far-field a certain distance from the interface. Time dependency as introduced by Aboulhasenzadeh *et al.* [27] will be much more difficult to put in place. Even by fixing $\delta(\theta) = \text{const}$ and integrating the heat equation over a radial portion, one can see that T_δ^θ is now time-dependent. Its temporal variations might have some impact on the model.

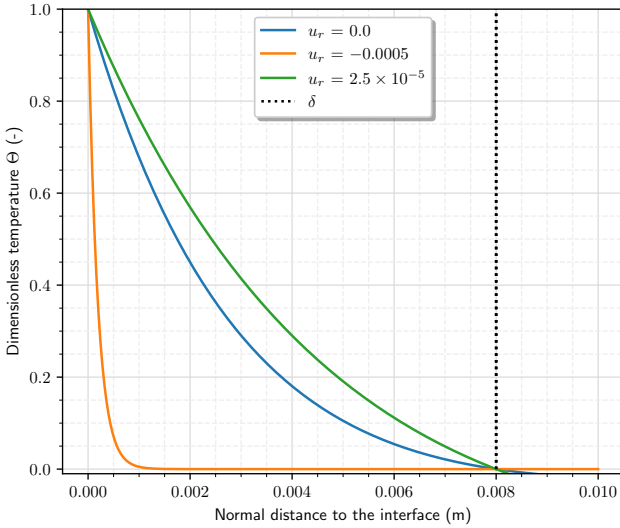
Around $r = 0$, the second-order term that emerges in the Taylor expansion of **Eq. (A.25)** does not cancel out, and its magnitude depends on the radial distance to the boundary layer thickness values $\frac{r}{\delta_1}$ and $\frac{r}{\delta_2}$, indicating that the profiles exhibit higher-order behaviour at the interface.

$$\begin{aligned} f(r) \underset{r=0}{=} & 1 + \frac{1}{C + D} \left(\frac{D}{\delta_2} - \frac{C}{\delta_1}\right) r \\ & + \frac{1}{C + D} \left(\frac{C}{\delta_1^2} + \frac{D}{\delta_2^2}\right) \frac{r^2}{2} + o(r^2) \end{aligned} \quad (\text{A.27})$$

Finally, conducting a Taylor expansion of the error function



(a)



(b)

Figure A.25: Form of the solution developed for the simplified problem.
(a) Effect of the curvature κ on the dimensionless temperature variations for given parameters: $\{A = -1 \times 10^{-5}; u_\theta = 1 \times 10^{-3} \text{ m s}^{-1}; \delta = 0.8 \times 10^{-2} \text{ m}; \alpha_l = 1 \times 10^{-5} \text{ m}^2 \text{ s}^{-1}; u_r = 0 \text{ m s}^{-1}\}$.
(b) Effect of the velocity u_r on temperature variations for given parameters: $\{\delta_1 = 0.5 \times 10^{-2} \text{ m}; \kappa = 500 \text{ m}^{-1}; \delta = 0.8 \times 10^{-2} \text{ m}; \alpha_l = 1 \times 10^{-7} \text{ m}^2 \text{ s}^{-1}\}$.

Eq. (23b) around $r = 0$ results in a linear profile:

$$f(r) \Big|_{r=0} = 1 - \frac{2}{\sqrt{\pi}} \frac{r}{\delta} + o(r^2) \quad (\text{A.28})$$

Appendix B Error assessment using a mean curvature

Incorporating the mean curvature $\kappa = \kappa_1 + \kappa_2$ into the solution implies a description of surface variation at the first order while employing two radii of curvature yields a second-order representation of the problem. Utilising a planar solution represents

only a zeroth order approximation, and the diffusion term $\propto \frac{\partial \Theta}{\partial r}$, scaled by $\frac{2}{r+R}$ due to the change of the basis vectors in the tangential directions (e.g. $\frac{\partial \mathbf{e}_r}{\partial \theta}$), remains non-zero in the context of significant thermal diffusion.

Indeed, within a curvilinear framework where we assume the local uniformity of radii of curvature and positivity ($R_1 = \text{const} > 0$ and $R_2 = \text{const} > 0$), the derivatives of the basis vectors along orthogonal curvilinear directions emerge from the diffusion term, resulting in two additional terms that vary with the normal direction r .

$$A \frac{\partial \Theta}{\partial r} = \frac{1}{r+R_1} \frac{\partial \Theta}{\partial r} + \frac{1}{r+R_2} \frac{\partial \Theta}{\partial r} = \left(\frac{R_1 + R_2 + 2r}{R_1 R_2 + r^2 + r(R_1 + R_2)} \right) \frac{\partial \Theta}{\partial r} \quad (\text{B.1})$$

Through the approximation of the term $A \frac{\partial \Theta}{\partial r}$ from Eq. (B.1) as $B \frac{\partial \Theta}{\partial r}$ in Eq. (B.3), by employing the osculating radius expression as depicted in Eq. (B.2), we can quantify the associated error.

$$R = \frac{2}{\kappa} = \frac{2}{\kappa_1 + \kappa_2} = \frac{2R_1 R_2}{R_1 + R_2} \quad (\text{B.2})$$

$$\frac{2}{R+r} \frac{\partial \Theta}{\partial r} = \frac{2(R_1 + R_2)}{2R_1 R_2 + r(R_1 + R_2)} \frac{\partial \Theta}{\partial r} = B \frac{\partial \Theta}{\partial r} \quad (\text{B.3})$$

This error is directly proportional to the radial distance to the interface, denoted as r , and to the square of the difference between the radii of curvature, expressed as $(R_1 - R_2)^2$ (for a detailed derivation, refer to Eq. (B.4)).

$$(A - B) \frac{\partial \Theta}{\partial r} = \left[\frac{1}{r+R_1} + \frac{1}{r+R_2} + \frac{2}{R+r} \right] \frac{\partial \Theta}{\partial r} - \left[\frac{R_1 + R_2 + 2r}{R_1 R_2 + r^2 + r(R_1 + R_2)} - \frac{2(R_1 + R_2)}{2R_1 R_2 + r(R_1 + R_2)} \right] \frac{\partial \Theta}{\partial r} \quad (\text{B.4})$$

$$\propto r \left(4R_1 R_2 - (R_1 + R_2)^2 \right)$$

$$\propto |r(R_1 - R_2)^2|$$

One can proceed to quantify the error by substituting R_2 with $R_1 + \varepsilon$ in Eq. (B.4) and subsequently conducting a Taylor expansion of the expression, where ε serves as a variable parameter around zero. This analysis reveals a distinctive third-order polynomial dependence on ε at the denominator, accompanied by second-order variations in the numerator, as illustrated in Eq. (B.5). In this equation, the coefficients $a_i(R_1, r)$ represent the polynomial coefficients, and k remains a constant term in the equation.

$$A - B = \frac{-r\varepsilon^2}{a_0(r, R_1) + a_1(r, R_1)\varepsilon + a_2(r, R_1)\varepsilon^2 + a_3(r, R_1)\varepsilon^3} = -r\varepsilon^2 \left[\frac{1}{a_0} + o(1) \right] = r \left[k\varepsilon^2 + o(\varepsilon^2) \right] \quad (\text{B.5})$$

Expression of coefficient a_0 is given in **Eq. (B.6)**.

$$a_0(R_1, r) = 2R_1^4 + r(6R_1^3) + r^2(6R_1^2) + r^3(2R_1) \quad (\text{B.6})$$

Performing a first-order Taylor expansion of the denominator in **Eq. (B.5)** and reordering the terms yields the final equation, as denoted by **Eq. (B.7)**. The influence of two curvature values may come into play in highly elongated bubbles, which, however, falls outside the scope of this study.

$$B \frac{\partial \Theta}{\partial r} = \left[A + r \underbrace{[k\varepsilon^2 + o(\varepsilon^2)]}_{\text{error}} \right] \frac{\partial \Theta}{\partial r} \quad (\text{B.7})$$

Appendix C Additional equations to perform Newton's algorithm

Appendix C.1 Literature's form of solution: error function (Erfc)

The two derivatives that are necessary to solve for the root of the function f (see **Eq. (33a)**) introduced in **Sec. 3.3.2** are:

$$\frac{\partial f}{\partial T_\infty^\theta}(\xi, \Phi) = \text{erf}\left(\frac{r}{\delta}\right) \quad (\text{C.1a})$$

$$\frac{\partial f}{\partial \delta}(\xi, \Phi) = -T_\infty^\theta \frac{2}{\sqrt{\pi}} \frac{r}{\delta^2} e^{-\left(\frac{r}{\delta}\right)^2} \quad (\text{C.1b})$$

One can notice that the local infinite temperature could be chosen to be the overall infinite temperature T_∞ imposed in the simulation.

The **Erfc** form of solutions **Eq. (23b)** introduced in **Sec. 3.3.2** presents a few problems in Newton's algorithm. The derivative of the function according to the free parameter δ tends to zero when δ tends to infinity. It can cause a convergence issue in the case where the initial guess $\delta^{(0)}$ is far from its optimal value. That is why Weiner *et al.* [26] has promoted the use of the integrated profile.

Derivatives shown in **Eq. (C.2)** are non zero which is preferable to perform Newton's algorithm.

$$\frac{\partial F}{\partial T_\infty^\theta}(\bar{\xi}, \Phi) = \left[\text{rerf}\left(\frac{r}{\delta}\right) + \delta \frac{e^{-\left(\frac{r}{\delta}\right)^2}}{\sqrt{\pi}} \right]_{r-\Delta/2}^{r+\Delta/2} \quad (\text{C.2a})$$

$$\frac{\partial F}{\partial \delta}(\bar{\xi}, \Phi) = \left[\frac{T_\infty^\theta}{\sqrt{\pi}} e^{-\left(\frac{r}{\delta}\right)^2} \right]_{r-\Delta/2}^{r+\Delta/2} \quad (\text{C.2b})$$

Appendix C.2 SoV form of solution: double exponentials profile

The derivative of the function f (see **Eq. (33c)**) derived in the present paper and employed in Newton's algorithm can be ex-

pressed as follows:

$$\frac{\partial f}{\partial \delta} = \frac{-T_\delta^\theta (1/\delta_1 + 1/\delta_2) e^{\delta(1/\delta_1 + 1/\delta_2)}}{(1 - e^{\delta(1/\delta_1 + 1/\delta_2)})^2} (e^{r/\delta_2} - e^{-r/\delta_1}) \quad (\text{C.3a})$$

$$\frac{\partial f}{\partial \delta_1} = \frac{-T_\delta^\theta e^{\delta(1/\delta_1 + 1/\delta_2)}}{\delta_1^2 (1 - e^{\delta(1/\delta_1 + 1/\delta_2)})^2} \times \left[\delta (e^{-r/\delta_1} - e^{r/\delta_2}) + r e^{-r/\delta_1} (e^{\delta(1/\delta_1 + 1/\delta_2)} - 1) \right] \quad (\text{C.3b})$$

$$\frac{\partial f}{\partial \delta_2} = \frac{-T_\delta^\theta}{\delta_2^2 (1 - e^{\delta(1/\delta_1 + 1/\delta_2)})^2} \times \left[e^{\delta(1/\delta_1 + 1/\delta_2)} ((r - \delta) e^{r/\delta_2} + \delta e^{-r/\delta_1}) - r e^{r/\delta_2} \right] \quad (\text{C.3c})$$

In the case of an integral approach, the derivatives of the function F (see **Eq. (34)**) according to the free parameters equal:

$$\frac{\partial F}{\partial \delta} = -T_\delta^\theta \left[\frac{(1/\delta_1 + 1/\delta_2) e^{\delta(1/\delta_1 + 1/\delta_2)}}{[1 - e^{\delta(1/\delta_1 + 1/\delta_2)}]^2} \times (\delta_2 e^{r/\delta_2} + \delta_1 e^{-r/\delta_1}) \right]_{r-\Delta/2}^{r+\Delta/2} \quad (\text{C.4a})$$

$$\frac{\partial F}{\partial \delta_1} = -\frac{T_\delta^\theta (1/\delta_1 + 1/\delta_2) e^{\delta(1/\delta_1 + 1/\delta_2)}}{\delta_1^2 [1 - e^{\delta(1/\delta_1 + 1/\delta_2)}]^2} \left[-\delta \delta_2 e^{r/\delta_2} + e^{-r/\delta_1} (r \delta_1 + \delta_1^2 - \delta_1 \delta - (r \delta_1 + \delta_1^2) e^{\delta(1/\delta_1 + 1/\delta_2)}) \right]_{r-\Delta/2}^{r+\Delta/2} \quad (\text{C.4b})$$

$$\frac{\partial F}{\partial \delta_2} = \frac{-T_\delta^\theta}{\delta_2^2 [1 - e^{\delta(1/\delta_1 + 1/\delta_2)}]^2} \left[-\delta \delta_1 e^{\delta(1/\delta_1 + 1/\delta_2)} e^{-r/\delta_1} + e^{r/\delta_2} ((\delta_2^2 - r \delta_2) + e^{\delta(1/\delta_1 + 1/\delta_2)} (r \delta_2 - \delta_2^2 - \delta \delta_2)) \right]_{r-\Delta/2}^{r+\Delta/2} \quad (\text{C.4c})$$

Appendix D Supplementary results on SoV fittings

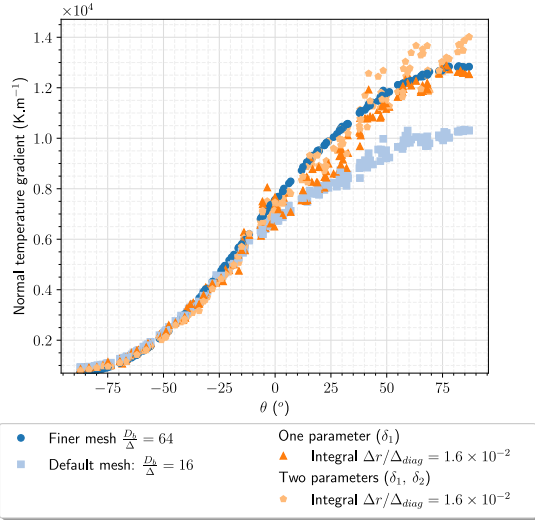
Dispersion figures.

Further fittings have been performed using the best candidate fitting procedure at two regimes and on several probe locations (200 probes). Results are shown in **Fig. D.26a** and **Fig. D.26b**.

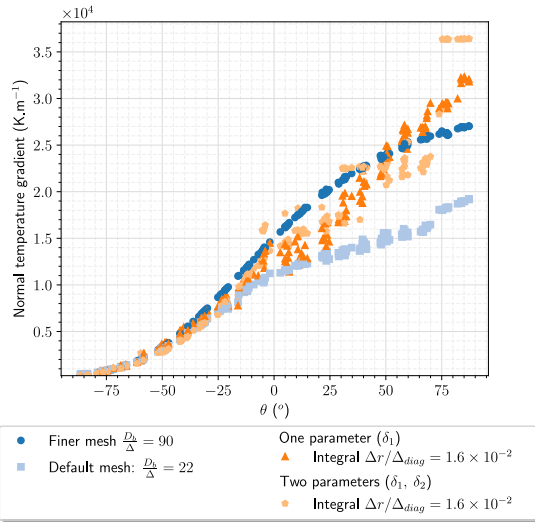
Both figures show dispersion in the predicted value depending on the azimuthal coordinate ϕ . Some improvements are observed in the top region due to the incoming fluid velocity feeding the fitting process. In the equator region, it is still difficult to enhance significantly the temperature gradient prediction.

Temperature and normal temperature gradient fitted profiles.

The temperature and normal temperature gradient predicted by the analytical form of solutions (once fitted) in the interface vicinity are visible for an angle $\theta = 83^\circ$ in **Fig. D.27**



(a)



(b)

Figure D.26: Dispersion in the predicted value for the best fitting approach using the SoV form of solutions with $u_r \neq 0$ at (a) $Ar^* = 50$ and $Pr_l = 1.0$ and (b) $Ar^* = 50$ and $Pr_l = 5.0$.

and **Fig. D.28**, respectively. The temperature profiles computed from both analytical forms of solutions show qualitatively similar variations on a finite length but the derivative of the erfc function is no longer describing well the second-order radial variations of the temperature at the exact location of the interface.

The effect of the temperature extension procedure is slightly visible on both original and fine mesh post-processed normal temperature gradient profiles (piecewise change of slope near $r \approx 0.1 \times 10^{-4}$ m).

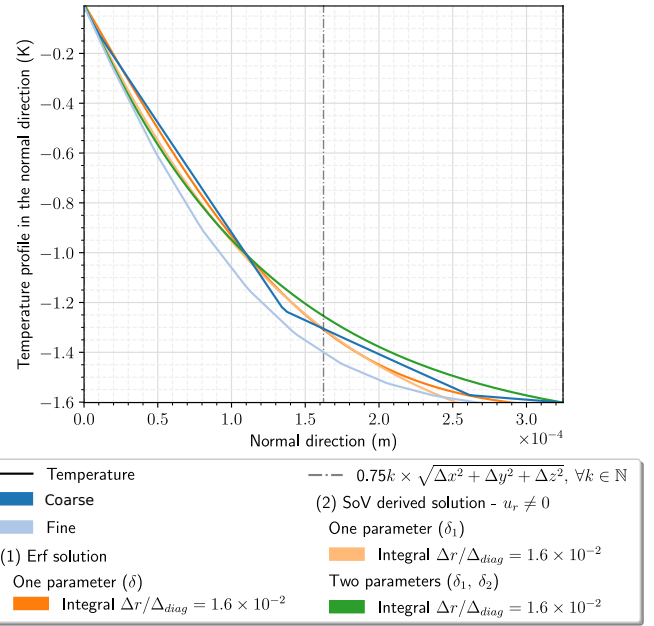


Figure D.27: Fitted normal temperature profiles in the interface vicinity and $\theta = 83^\circ$ using different approaches (Erf and SoV forms of solution) at $Ar^* = 50$ and $Pr_l = 1.0$. The spatial resolution of the coarse and fine mesh solutions equal $D_b/\Delta = 16$ and $D_b/\Delta = 64$, respectively

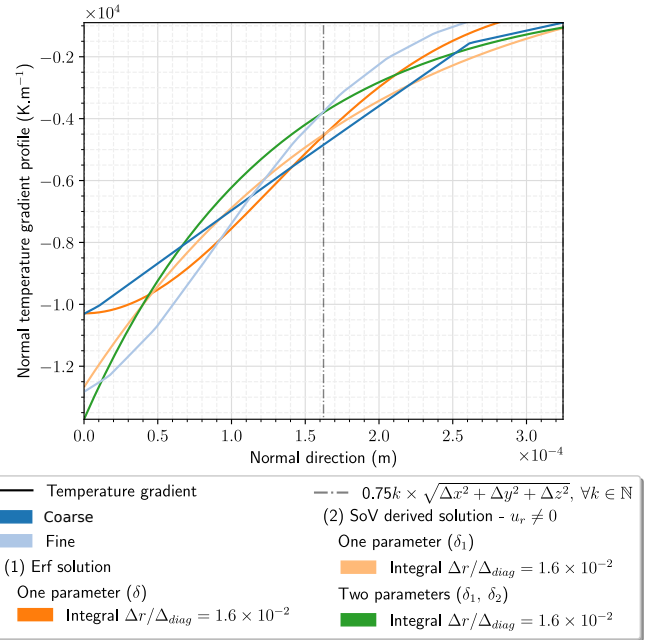


Figure D.28: Fitted normal temperature gradient profile in the interface vicinity and $\theta = 83^\circ$ using different approaches (Erf and SoV forms of solution) at $Ar^* = 50$ and $Pr_l = 1.0$. The spatial resolution of the coarse and fine mesh solutions equal $D_b/\Delta = 16$ and $D_b/\Delta = 64$, respectively

References

- [1] S. Tanguy, M. Sagan, B. Lallane, F. Couderc, C. Colin, Benchmarks and numerical methods for the simulation of boiling flows, *Journal of Computational Physics* 264 (2014) 1–22. doi:10.1016/j.jcp.2014.01.014.
- [2] L. C. Malan, A. G. Malan, S. Zaleski, P. G. Rousseau, A geometric VOF method for interface resolved phase change and conservative thermal en-

- ergy advection, *Journal of Computational Physics* 426 (2021) 109920. doi:10.1016/j.jcp.2020.109920.
- [3] S. Tanguy, T. Ménard, A. Berlemont, A level set method for vaporizing two-phase flows, *Journal of Computational Physics* 221 (2) (2007) 837–853. doi:10.1016/j.jcp.2006.07.003.
- [4] J. Schlottke, B. Weigand, Direct numerical simulation of evaporating droplets, *Journal of Computational Physics* 227 (10) (2008) 5215–5237. doi:10.1016/j.jcp.2008.01.042.
- [5] A. Orazzo, S. Tanguy, Direct numerical simulations of droplet condensation, *International Journal of Heat and Mass Transfer* 129 (2019) 432–448. doi:10.1016/j.ijheatmasstransfer.2018.07.094. URL <https://doi.org/10.1016/j.ijheatmasstransfer.2018.07.094>
- [6] L. G. Martinez, B. Duret, J. Reveillon, F. Demoulin, A new DNS formalism dedicated to turbulent two-phase flows with phase change, *International Journal of Multiphase Flow* 143 (2021) 103762. doi:10.1016/j.ijmultiphaseflow.2021.103762.
- [7] R. Scardovelli, S. Zaleski, DIRECT NUMERICAL SIMULATION OF FREE-SURFACE AND INTERFACIAL FLOW, *Annual Review of Fluid Mechanics* 31 (1) (1999) 567–603. doi:10.1146/annurev.fluid.31.1.567.
- [8] D. Gründing, S. Fleckenstein, D. Bothe, A subgrid-scale model for reactive concentration boundary layers for 3d mass transfer simulations with deformable fluid interfaces, *International Journal of Heat and Mass Transfer* 101 (2016) 476–487. doi:10.1016/j.ijheatmasstransfer.2016.04.119. URL <https://doi.org/10.1016/j.ijheatmasstransfer.2016.04.119>
- [9] B. Mathieu, Études physique, expérimentale et numérique des mécanismes de base intervenant dans les écoulements diphasiques en micro-fluidique, Ph.D. thesis, Université de Provence (2003).
- [10] A. Toutant, Modélisation physique des interactions entre interfaces et turbulence, Ph.D. thesis, Docteur de l’Institut National Polytechnique de Toulouse (2006).
- [11] G. Weymouth, D. K. P. Yue, Conservative volume-of-fluid method for free-surface simulations on cartesian-grids, *Journal of Computational Physics* 229 (8) (2010) 2853–2865. doi:10.1016/j.jcp.2009.12.018.
- [12] C. P. Zanutto, E. Paladino, F. Evrard, B. van Wachem, F. Denner, Modeling of interfacial mass transfer based on a single-field formulation and an algebraic vof method considering non-isothermal systems and large volume changes, *Chemical Engineering Science* 247 (2022) 116855. doi:10.1016/j.ces.2021.116855. URL <https://doi.org/10.1016/j.ces.2021.116855>
- [13] A. Toutant, B. Mathieu, O. Lebaigue, Volume-conserving mesh smoothing for front-tracking methods, *Computers & Fluids* 67 (2012) 16–25. doi:10.1016/j.compfluid.2012.06.019.
- [14] D. Legendre, J. Borée, J. Magnaudet, Thermal and dynamic evolution of a spherical bubble moving steadily in a superheated or subcooled liquid, *Physics of Fluids* 10 (6) (1998) 1256–1272. doi:10.1063/1.869654.
- [15] R. Duraiswami, A. Prosperetti, Orthogonal mapping in two dimensions, *Journal of Computational Physics* 98 (2) (1992) 254–268. doi:10.1016/0021-9991(92)90141-k. URL [https://doi.org/10.1016/0021-9991\(92\)90141-k](https://doi.org/10.1016/0021-9991(92)90141-k)
- [16] B. Yang, A. Prosperetti, Vapour bubble collapse in isothermal and non-isothermal liquids, *Journal of Fluid Mechanics* 601 (2008) 253–279. doi:10.1017/s0022112008000670. URL <https://doi.org/10.1017/s0022112008000670>
- [17] S. V. Patankar, *Numerical Heat Transfer and Fluid Flow*, CRC Press, 2018. doi:10.1201/9781482234213. URL <https://doi.org/10.1201/9781482234213>
- [18] G. Tryggvason, R. Scardovelli, S. Zaleski, *Direct Numerical Simulations of Gas-Liquid Multiphase Flows*, Cambridge University Press, 2001. doi:10.1017/cbo9780511975264.
- [19] R. P. Fedkiw, T. Aslam, B. Merriman, S. Osher, A non-oscillatory eulerian approach to interfaces in multimaterial flows (the ghost fluid method), *Journal of Computational Physics* 152 (2) (1999) 457–492. doi:10.1006/jcph.1999.6236. URL <https://doi.org/10.1006/jcph.1999.6236>
- [20] Y. Sato, B. Ničeno, A sharp-interface phase change model for a mass-conservative interface tracking method, *Journal of Computational Physics* 249 (2013) 127–161. doi:10.1016/j.jcp.2013.04.035.
- [21] A. Urbano, S. Tanguy, G. Huber, C. Colin, Direct numerical simulation of nucleate boiling in micro-layer regime, *International Journal of Heat and Mass Transfer* 123 (2018) 1128–1137. doi:10.1016/j.ijheatmasstransfer.2018.02.104.
- [22] A. W. Vreman, Particle-resolved direct numerical simulation of homogeneous isotropic turbulence modified by small fixed spheres, *Journal of Fluid Mechanics* 796 (2016) 40–85. doi:10.1017/jfm.2016.228.
- [23] S. Popinet, *Basilisk* (2022). URL <http://basilisk.fr>
- [24] S. Zhao, J. Zhang, M. Ni, Boiling and evaporation model for liquid-gas flows: A sharp and conservative method based on the geometrical VOF approach, *Journal of Computational Physics* (2021) 110908. doi:10.1016/j.jcp.2021.110908.
- [25] A. Weiner, Modeling and simulation of convection-dominated species transfer at rising bubbles, Ph.D. thesis, Technical University of Darmstadt (2020).
- [26] A. Weiner, D. Bothe, Advanced subgrid-scale modeling for convection-dominated species transport at fluid interfaces with application to mass transfer from rising bubbles, *Journal of Computational Physics* 347 (2017) 261–289. doi:10.1016/j.jcp.2017.06.040.
- [27] B. Aboulhasanzadeh, S. Thomas, M. Taeibi-Rahni, G. Tryggvason, Multiscale computations of mass transfer from buoyant bubbles, *Chemical Engineering Science* 75 (2012) 456–467. doi:10.1016/j.ces.2012.04.005.
- [28] R. Ostilla-Monico, Y. Yang, E. van der Poel, D. Lohse, R. Verzicco, A multiple-resolution strategy for direct numerical simulation of scalar turbulence, *Journal of Computational Physics* 301 (2015) 308–321. doi:10.1016/j.jcp.2015.08.031. URL <https://doi.org/10.1016/j.jcp.2015.08.031>
- [29] D. Bothe, S. Fleckenstein, A volume-of-fluid-based method for mass transfer processes at fluid particles, *Chemical Engineering Science* 101 (2013) 283–302. doi:10.1016/j.ces.2013.05.029.
- [30] H.-J. W. D. Bothe, M. Kröger, A vof-based conservative method for the simulation of reactive mass transfer from rising bubbles, *Fluid Dynamics & Materials Processing* 7 (3) (2011) 303–316. doi:10.3970/fdmp.2011.007.303. URL <http://www.techscience.com/fdmp/v7n3/24537>
- [31] K. Cai, G. Huang, Y. Song, J. Yin, D. Wang, A sub-grid scale model developed for the hexahedral grid to simulate the mass transfer between gas and liquid, *International Journal of Heat and Mass Transfer* 181 (2021) 121864. doi:10.1016/j.ijheatmasstransfer.2021.121864.
- [32] C. M. Y. Claassen, S. Islam, E. A. J. F. Peters, N. G. Deen, J. A. M. Kuipers, M. W. Baltussen, An improved subgrid scale model for front-tracking based simulations of mass transfer from bubbles, *AIChE Journal* 66 (4) (Dec. 2019). doi:10.1002/aic.16889. URL <https://doi.org/10.1002/aic.16889>
- [33] A. Weiner, C. M. Y. Claassen, I. R. Hierck, J. A. M. Kuipers, M. W. Baltussen, Assessment of a subgrid-scale model for convection-dominated mass transfer for initial transient rise of a bubble, *AIChE Journal* (feb 2022). doi:10.1002/aic.17641.
- [34] S. Fleckenstein, D. Bothe, A volume-of-fluid-based numerical method for multi-component mass transfer with local volume changes, *Journal of Computational Physics* 301 (2015) 35–58. doi:10.1016/j.jcp.2015.08.011. URL <https://doi.org/10.1016/j.jcp.2015.08.011>
- [35] F. H. Harlow, J. E. Welch, Numerical calculation of time-dependent viscous incompressible flow of fluid with free surface, *Physics of Fluids* 8 (12) (1965) 2182. doi:10.1063/1.1761178.
- [36] X. Liu, R. Fedkiw, M. Kang, A boundary condition capturing method for poisson’s equation on irregular domains, *Journal of Computational Physics* 160 (2000) 151–178.
- [37] F. Gibou, L. Chen, D. Nguyen, S. Banerjee, A level set based sharp interface method for the multiphase incompressible navier–stokes equations with phase change, *Journal of Computational Physics* 222 (2) (2007) 536–555. doi:10.1016/j.jcp.2006.07.035.
- [38] R. Egan, F. Gibou, xGFM: Recovering convergence of fluxes in the ghost fluid method, *Journal of Computational Physics* 409 (2020) 109351. doi:10.1016/j.jcp.2020.109351.
- [39] Y. Wang, X. Chen, X. Wang, V. Yang, Vaporization of liquid droplet with large deformation and high mass transfer rate, II: Variable-density,

- variable-property case, *Journal of Computational Physics* 394 (2019) 1–17. doi:10.1016/j.jcp.2019.04.052.
- [40] S. Popinet, Numerical models of surface tension, *Annual Review of Fluid Mechanics* 50 (1) (2018) 49–75. doi:10.1146/annurev-fluid-122316-045034.
URL <https://doi.org/10.1146/annurev-fluid-122316-045034>
- [41] F. Denner, B. van Wachem, Numerical time-step restrictions as a result of capillary waves, *Journal of Computational Physics* 285 (2015) 24–40. doi:10.1016/j.jcp.2015.01.021.
URL <https://doi.org/10.1016/j.jcp.2015.01.021>
- [42] T. D. Aslam, A partial differential equation approach to multidimensional extrapolation, *Journal of Computational Physics* 193 (1) (2004) 349–355. doi:10.1016/j.jcp.2003.08.001.
- [43] E. Lemmon, M. Huber, M. McLinden, Nist standard reference database 23: Reference fluid thermodynamic and transport properties-refprop, version 9.1 (2013-05-07 2013).
URL https://tsapps.nist.gov/publication/get_pdf.cfm?pub_id=912382
- [44] Z. Feng, E. E. Michaelides, Heat and mass transfer coefficients of viscous spheres, *International Journal of Heat and Mass Transfer* 44 (23) (2001) 4445–4454. doi:10.1016/s0017-9310(01)00090-4.
URL [https://doi.org/10.1016/s0017-9310\(01\)00090-4](https://doi.org/10.1016/s0017-9310(01)00090-4)
- [45] Z. Feng, E. E. Michaelides, Drag coefficients of viscous spheres at intermediate and high reynolds numbers, *Journal of Fluids Engineering* 123 (4) (2001) 841–849. doi:10.1115/1.1412458.
URL <https://doi.org/10.1115/1.1412458>
- [46] A. Weiner, D. Gründing, D. Bothe, Computing mass transfer at deformable bubbles for high schmidt numbers, *Chemie Ingenieur Technik* 93 (1-2) (2020) 81–90. doi:10.1002/cite.202000214.
URL <https://doi.org/10.1002/cite.202000214>
- [47] W. Bizid, Développement de méthodes de pénalisation pour la simulation de l'écoulement turbulent autour d'obstacles, Ph.D. thesis, Université de Bordeaux (2017).
- [48] E. Balaras, C. Benocci, U. Piomelli, Two-layer approximate boundary conditions for large-eddy simulations, *AIAA Journal* 34 (6) (1996) 1111–1119. doi:10.2514/3.13200.
URL <https://doi.org/10.2514/3.13200>
- [49] E. Labourasse, P. Sagaut, Reconstruction of turbulent fluctuations using a hybrid RANS/LES approach, *Journal of Computational Physics* 182 (1) (2002) 301–336. doi:10.1006/jcph.2002.7169.
URL <https://doi.org/10.1006/jcph.2002.7169>
- [50] Y. Benarafa, O. Cioni, F. Ducros, P. Sagaut, RANS/LES coupling for unsteady turbulent flow simulation at high reynolds number on coarse meshes, *Computer Methods in Applied Mechanics and Engineering* 195 (23-24) (2006) 2939–2960. doi:10.1016/j.cma.2005.06.007.
URL <https://doi.org/10.1016/j.cma.2005.06.007>
- [51] A. Chatelain, Simulation des grandes echelles d'écoulements turbulents avec transferts de chaleur, Ph.D. thesis.
- [52] D. Gründing, S. Fleckenstein, D. Bothe, A subgrid-scale model for reactive concentration boundary layers for 3d mass transfer simulations with deformable fluid interfaces, *International Journal of Heat and Mass Transfer* 101 (2016) 476–487. doi:10.1016/j.ijheatmasstransfer.2016.04.119.
- [53] R. Bird, *Transport phenomena*, J. Wiley, New York, 2002.